Experiments on Ultracold Rb: Rydberg atoms and Rb_2 molecules.
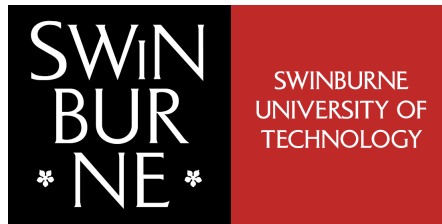
A thesis submitted for the degree of

Doctor of Philosophy

by

Heath Kitson

You will undertake and complete many tasks.

— Fortune cookie, 26th August 2006

Declaration

I, Heath Kitson, declare that this thesis entitled:

"Experiments on Ultracold Rb: Rydberg atoms and Rb_2 molecules."

is my own work and has not been submitted previously, in whole or in part, in respect of any other academic award.

Heath Kitson

Centre for Atom Optics and Ultra-fast Spectrsocopy
Faculty of Engineering and Industrial Sciences
Swinburne University of Technology
Australia

Dated this day, December 5, 2007

Abstract

This thesis presents experiments done in both ^{85}Rb and ^{87}Rb magneto optical traps. Fluorescence techniques are employed for the initial characterisation of atom number, density, temperature, loading and collisional rates in the trap. Spectroscopy of atomic energy levels over most of the optical spectrum is presented for ^{85}Rb, using a two-photon ionisation technique. The atomic nd states where n= 6 - 42 are resolved over an energy range of 15,800 - 20,800 cm^{-1}. An additional broad series of peaks following the nd series is observed but their origin could not be identified.

The absence of transit time and collisional effects in the ultracold atomic sample allows the measurement of atomic lifetimes over a broad range of states. Time resolved two-photon ionisation experiments are described and the resulting lifetime data are presented for the nd series over n=11 to 37, the most complete such measurements to date. A model of population dynamics following excitation to an nd state is made, taking into account the coupling of nearby dipole-connected energy levels by blackbody radiation. A comparison is made between two models of the strength of the interaction between atomic levels and blackbody radiation, by comparing modelled decay rates to experimental decay curves over the measured range of principal quantum numbers.

A series of measurements on ultracold Rb$_2$ molecules are made using resonance enhanced multi-photon ionisation and time of flight discrimination. Spectroscopy of excited molecular states over most of the optical spectrum is presented. The $(2)^3\Sigma_g^+$ (5s+4d), $(2)^3\Pi_g$(5s+4d) and $(3)^3\Sigma_g^+$(5s+6s) electronic molecular states are identified,

but the vibrational levels are not well resolved.

Fluorescence based trap-loss measurements and some ionisation data are presented for states up to $30 \, \text{cm}^{-1}$ below the $5s+5p_{3/2}$ limits for ^{87}Rb and ^{85}Rb. The vibrational series of the 0_u^+, 1_g and 0_g^- electronic molecular states are assigned; including some vibrational levels that have not previously been assigned. C_3 coefficients for the internuclear potential are measured for 0_u^+ and 1_g states of both Rb isotopes. These determine the strength of the resonant-dipole interaction, the $\langle 5p|er|5s \rangle$ dipole matrix element, and therefore the 5p lifetime for both isotopes. There is no isotopic difference observable in the C_3 coefficients for each series within the experimental uncertainty. However a systematic, isotope-dependent deviation of vibrational-level energies is clearly observed, suggesting the need for a more sophisticated model, possibly involving R-dependent spin-orbit coupling, to fully explain the spectra. Bound-bound spectroscopy is performed on upper excited states from the bound ground-state photoassociation decay products.

Acknowledgements

I would like to thank my supervisors Wayne Rowlands and Peter Hannaford for giving me the opportunity to work in their research group, in an exciting and fast moving research field. They provided the initial direction, funding and equipment for all of the work presented here. Their office doors were always open to me.

This project would not be possible without generous and more often than not long-term loans of major items of expensive equipment. Thanks must go to David Booth for handing me the keys to MOPO and teaching me to drive it. Steven Collins and Thin Ngyuyen for the generous loan of a wave-meter; Andre Sidorov, Russell Mclean and David Gough for the loan of the Ti:Sapphire laser; and David for your help installing it; Lap Van Do and David McDonald for the loan of two box-car integrators, a Joulemeter and a formerly OD 3 filter; Brenton Hall for the loaning of the MOT power supply; Anthony Bartel for the loan of a NIM-BIN and Alexander Akulshin for the loan of a digital signal generator. I extend thanks to all of those I have forgotten to mention whos equipment crossed the event horizon.

I spent six valuable weeks working at Insitituto per i Processi Chimico-Fisici at the CNR in Pisa. Carlo Gabbanini, Andrea Fioretti and Jerome Lozielle took me under their wings and taught me about photo-association and ionisation techniques.

Special thanks go to Mark "the magnificent" Kivinen for the design and manufacture of custom components, without whom I would remain a butcher, not a scientist. Thanks also go to Tatiana Tchernova and Sharon Jesson for their administrative support.

Dru Morrish generously gave me his LaTeX source code as a template for this document. Many hours were spent reading and improving drafts of this document by Wayne

Rowlands, Peter Hannaford, Michael Volk and Chris Ticknor for which I am grateful.

Prof. Dr. Eberhard Tiemann deepened my understanding of molecular structure with useful discussion and specific comments on my data. Russel McLean, David Gough, Alexander Akulshin, Peter Cadusch, Andrei Sidorov, Bryan Dalton, Tien Kieu and Paul Stoddart all made time to answer questions in their fields of expertise. James Wang, Daniel Day and Daniel White assisted with coating facilities, use of an absorption spectrometer, and fibre tip imaging and polishing.

Over the years students including Skits, Kaiser, Bird, Ruthless, Skank, D-day, McPhail, Frog, Gringo, Dmac, Dan, Go Tra me Ti Do, Futz in mouth, Gopisankarararao Veeravalli, Saeed, Silver-wolf, Wanner, Dyke and The Man provided me with much advice on physics and otherwise, over many good lunches and some bad (HKSF).

Midway through my PhD my solitude was broken by the arrival of the lithium team including Grainne "Mother" Duffy, Juergen "Futzs in mouth" Fuchs, Gopisankara"rara"rao Veeravalli and Paul Dyke. Lithium is commonly prescribed as a prophylaxis for depression and the lithium team bought with them good company, valuable expertise and equipment all of which proved essential for the completion of this thesis and for which I am especially grateful.

Gopisankararao Veeravelli worked for 12 months on this project during which time, not coincidentally, all of the major results were taken. He quickly proved himself a formidable researcher obtaining the brightest MOT to date in the experiment, and continued to prove himself worth every syllable for the length of the project.

Thanks to all who participated in runs, rides, netball, squash, basketball, triathalons and some clocking on. Acknowledgement also goes to the inner-suburban poker tour who funded part of my studies.

During the write up phase of this thesis I was supported by my parents Andrew and Joan Kitson, who nourished me with mineral water, peaches and a vision of a future after write-up.

Heath Kitson
Melbourne, Australia
December 5, 2007

Contents

List of Figures

List of Tables

List of Abbreviations

Standard abbreviations which are used and defined in the body of this thesis.

MOT	Magneto-Optical Trap
AOM	Acousto-Optical Modulator
PZT	Piezo Transducer
UHV	Ultra High Vacuum ($< 10^{-8}$ Torr)
MOPO	Master Oscillator Power Oscillator
CEM	Channeltron Electron Multiplier
CCD	Charge-Coupled Device
TOF	Time Of Flight
JWKB	Jeffreys-Wentzel-Kramers-Brillouin
FWHM	Full Width at Half Maximum
PI	Photo-Ionisation
PA	Photo-Association
REMPI	Resonance-Enhanced Multi-Photon Ionisation
RE2PI	Resonance-Enhanced 2-Photon Ionisation
Nd:YAG	Neodymium-doped Yttrium Aluminium Garnet ($Nd:Y_3Al_5O_{12}$)
Ti:Saph	Titanium-doped Sapphire ($Ti:Al_2O_3$)
CW	Continuous Wave
NDE	Near Dissociation Expansion

Chapter 1

Introduction

"If high-energy accelerators make the rap music of physics-with their whirling particles and rapid-fire smashups, then collisions between ultracold atoms are its Wagnerian opera . . . . . ."

— Science, **280**, 200 (1998)

1.1   The Big Picture

The big bang theory suggests that the universe was formed at very high temperatures, then passed through progressively cooler epochs as it expanded. Each epoch was characterised by the "freezing out" of a new interaction, or the predominance of a new form of stable matter. For example the grand-unification epoch saw the separation of gravity from the gauge interactions: electromagnetism, the strong and weak nuclear forces. The hadron epoch saw temperatures fall low enough for quarks and gluons to form stable protons and neutrons [1]. This cooling process has continued to the present epoch with the ambient background radiation at 2.8 K, with four fundamental interactions frozen out and stable super-clusters of galaxies formed.

Particle accelerators such as the planned 30-40 km US\$6.6 billion International Linear Collider [2] are able to probe high-energy collisional regimes, 6×10^{15} K, equivalent to temperatures shortly after the big bang. Surprisingly, table-top laser trapping and cooling techniques and evaporative cooling techniques can now produce the lowest known equilibrium temperatures in the natural universe 10^{-9} K. In this low-energy collisional regime classical atomic models break down and the quantum nature of matter and interactions becomes important:

- The de Broglie wavelength of scattering atoms becomes larger than the chemical bond length so wavelike and relativistic effects such as resonances, interferences, and retardation become important.

- Only the lowest partial waves of the scattering wave-function can penetrate the centrifugal interaction barrier, so that there is no averaging out of resonances, nodes and antinodes in the scattering wave-function.

- The collisional interaction time becomes large for low energy collisions, allowing interactions on even weakly attractive potentials. When collisional timescales are longer than atomic radiative lifetimes, the collision process becomes sensitive to interaction with external radiation.

- The Doppler width of transitions becomes narrower than the natural width of atomic dipole transitions.

1.2 Laser cooling of Atoms

Early in the 17th century in his treatise "De Cometis" Kepler proposed that radiation exerts a pressure on matter following the observation that comets' tails point away from the Sun. In 1901 Lebedev made the first quantitative measure of radiation pressure from the sun on a macroscopic plate in the laboratory [3] and then in 1933 Frisch deflected a beam of sodium atoms using resonant light from a lamp [4].

Following the invention of the laser, Hänsch and Schawlow and independently Wineland and Dehmelt proposed applying the radiation force of light to laser cool atoms and ions in 1975 [5] [6]. In both proposals atoms are irradiated with light red-detuned from a resonance. Atoms moving towards the radiation source see the light Doppler shifted towards resonance and preferentially absorb photons from the direction opposing their motion. After each absorption the atom spontaneously re-emits a photon in a random direction which imparts no net momentum when averaged over many absorption-emission cycles. The net effect is a force opposing the atom's motion. When applied in three dimensions this laser cooling scheme is called optical molasses after the viscous nature of its namesake.

Optical molasses was first demonstrated by Chu *et al.* for Na atoms in 1985 [7]. Temperature measurements below the theoretical predicted Doppler limit [8] led Dalibard and Cohen-Tannoudji to propose a new polarisation gradient cooling scheme in 1989 [9]. Two years after the first demonstration of molasses Raab *et al.* showed that the addition of an inhomogeneous magnetic field can provide a spatially dependent, conservative confining force in addition to the velocity dependent dissipative molasses forces [10]. This trap was called a Magneto Optical Trap (MOT) and was first loaded from a pre-slowed Na beam. In 1990 Monroe *et al.* simplified the MOT setup by loading from a room temperature background vapour without any pre-slowing [11]. The MOT has become a standard tool for many areas of atomic physics producing cold, dilute samples of atoms.

1.3   Photo-association

Photoassociation (PA) is a process where two free atoms absorb a photon during a collision and form a bound molecule. A typical PA reaction for Rb atoms initially in the 5s ground state is:

$$Rb(5s) + Rb(5s) + h\nu_{pa} \rightarrow Rb_2^* \tag{1.1}$$
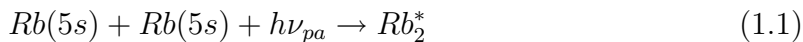
Laser controlled chemistry has been an active area of research since the invention of the laser; however high power densities (MW/cm^2) were required and poor molecular yields produced. High power density is necessary to modify the strong chemical binding interaction of bound molecules [12]. PA of free atoms requires much lower power densities since the long range binding is governed by relatively weak electrostatic dispersion interaction. PA processes were first studied at room temperature [13] but still produced poor yields, due to the wide collisional energy distribution and Doppler broadening of reaction transitions for atoms at room temperature.

PA experiments of ultra-cold atoms were proposed very soon after the first demonstration of laser cooling [14]. The availability of ultra-cold atomic samples allowed reactants with a very narrow range of collisional energies to be addressed by spectrally intense narrow-band lasers. This results in high molecular yields in a very narrow energetic range of final states. The energy resolution is typically limited by the PA laser linewidth or the atomic natural linewidth, with a collisional distribution of the atoms of just 2 MHz in this experiment for example.

The most important application of PA has been the high resolution spectroscopy of molecular potentials at long range. At thermal energies, molecular transitions typically occur close to their equilibrium internuclear separation of around 4-7 Åwhere there is substantial wavefunction overlap and exchange energy is the dominant interaction. By contrast, PA favours the formation of molecules with large internuclear separations, which have good Franck-Condon overlap with the initial unbound scattering state (see Figure 5.7 shown later). Under these conditions molecules are formed with internuclear separation of order 100 Å, where fine-structure, hyperfine structure and retardation effects are significant. Photoassociation spectroscopy also measures absolute binding energies of states.

In addition to molecular parameters, PA measurements give information on the atomic scattering process and properties of the unbound atoms. S-wave scattering lengths can be determined from nodes in the PA spectra, or from the energy of the least bound vibrational level in the ground state potential. The s-wave scattering length determines the mean field interaction of atoms which are cooled below the p-wave centrifugal barrier (80 μK for ^{87}Rb). Atomic lifetimes can also be related to the strength of the R^{-3} behaviour of the molecular potential at long range.

PA of laser cooled atoms also provides a useful source of ultra-cold molecules, which are difficult to directly laser cool due to their complicated level structure and lack of closed optical transitions. Molecules formed by PA are used in this work for further bound-bound spectroscopy of excited molecular states. Some other proposed applications of cold molecules are the search for electron dipole moments in polar molecules [15], entanglement of constituent atoms, dissociated from ultracold molecules [16], coherent super-chemistry of quantum degenerate samples [17] and interferometry with molecules [18].

1.4   Thesis Objective

The work presented in this thesis was undertaken in a new research group. All of the apparatus described herein was designed, constructed and characterised by the author; no other research students or staff were assigned to this project, except during the data acquisition stage of the project. The initial aims of this project were to build up a new experimental apparatus for the formation, trapping and study of ultra-cold molecules.

The apparatus combines laser trapping and cooling techniques in a UHV environment with tuneable narrow-band lasers for high resolution (1 part in 10^7) spectroscopic measurements and intense pulsed ionisation techniques which allow sensitive time-of-flight discrimination of single molecules.

The tunability of the ionisation laser, over the entire optical spectrum, combined with an ultra-cold sample of atoms presented opportunities to take spectroscopic measurements over a wide energy range. Atomic measurements were made for states with n=5-40, limited by the almost Fourier-limited bandwidth of the probe laser and the high density of states. The low atom temperature and dilution of the laser cooled sample eliminates transit time and collisional limitations, allowing lifetime measurements over the widest range of principal quantum numbers published in this system to date.

This work presents the most complete measurement of atomic lifetimes and black-body interaction cross-section, ever recorded in the Rb system. These measurements build on similar measurements in the literature over much smaller energy range measurements described in the literature. In addition a lifetime model was developed in this thesis, and fitted to the lifetime data which allowed an accurate test of theoretical lifetime and blackbody interaction calculations and approximations. Both lifetimes and interactions are measured at high principal quantum numbers where there is very little core-valence electron interaction, and down to the ground state where these interactions are significant, and quantum defect approximations break down.

Photo-association was performed in both ^{85}Rb and ^{87}Rb isotopes. This work also builds on previous similar measurements, but this thesis presents the most complete measurements of the two atomic systems under the same experimental conditions allowing isotopic comparisons over a wide range of detuning and internuclear separation. The spectroscopic energy range covered includes regions dominated by the hyperfine, the fine and the Van Der Walls interaction.

As in previously published work, the resulting vibrational level progressions are well explained theoretically using Near-Dissociation Expansion (NDE). However deviations from the NDE model are observed suggesting the need for an improved relativistic model. A more complete analysis will include R-dependent spin-orbit coupling and possibly pre-dissociation shifts and hyperfine structure. This work reveals significant

isotopic effects which require additional theoretical investigation beyond the scope of this thesis.

1.5   Outline of this Thesis

Chapter 2 outlines the laser trapping and cooling of the atomic sample which is used in later experiments. A semiclassical overview of optical molasses and the Magneto-Optical Trapping (MOT) schemes are presented placing an emphasis on the limitations of these techniques on the trapped atom numbers, densities and temperatures.

An overview of the experimental systems built up for the MOT, including vacuum systems, laser systems, magnetic field, imaging and data acquisition systems is provided in Section 2.2. Experimental loading and collision rates in the MOT are determined in Section 2.3.2. Other experimental trap parameters including trap size, atom number, atom density and ensemble temperature are presented. These are related back to the theoretical limitations and to the requirements for the experiments that follow in Section 2.4. Finally the measured trap parameters are compared to the requirements for the experiments in later chapters.

Chapter 3 details the setup of an ionisation detection system. Section 3.1 compares ionisation detection to the fluorescence detection techniques introduced in the previous chapter. The experimental set-up including the ionising laser, ion detection, time-of-flight discrimination, and data collection systems are outlined in the remainder of the chapter. An electric-field simulation is presented in Section 3.3. It is used to calculate ion times of flight, TOF discrimination resolution, and to characterise the electric field at the MOT, which introduces perturbations in the sample.

Chapter 4 describes experiments performed on Rydberg atoms of rubidium. It begins with a review of previous work on Rydberg atoms in Section 4.1. Rydberg wave-functions, energy levels, radiative lifetimes, interaction with blackbody radiation and

dipole matrix elements are then presented from the perspective of the quantum-defect model in Section 4.3.

An experimental energy level spectrum for ^{85}Rb is presented in Section 4.4. Levels are assigned and compared to predictions of the quantum-defect model. A previously unreported series of prominent broad features is observed and characterized but not assigned. Perturbations of the atomic sample due to external fields are investigated.

In Section 4.5, population dynamics of atoms excited to a wide range of nd states are measured with an ionisation technique. The dynamics are modelled using radiative lifetimes and two models of the coupling strength to neighbouring levels by ambient blackbody radiation are presented in Section 4.6. Fits to the experimental data are used to discriminate between models of blackbody interaction in Sections 4.7 and 4.8. Both blackbody coupling strength models appear in the literature, but this is the first experimental comparison of the two models and their validity over a broad range of principal quantum numbers.

Chapter 5 presents a theoretical overview of diatomic molecules and photo-association starting with a discussion of the Schrödinger equation for diatomic molecules in Section 5.1. Section 5.2 introduces angular momentum coupling in molecules and the quantum numbers used to describe molecules in different coupling regimes. The Born-Oppenheimer potentials relevant to the experiments presented here are introduced in Sections 5.5 and 5.4.

The asymptotic potential approximation is introduced in Section 5.3 and the Le Roy-Bernstein formalism in Section 5.6, which provides the basic tools required to analyse the photo-association spectra presented in the next chapter. This chapter concludes with a discussion of molecular wave-functions and the photo-association process, including line-strengths and transition rates.

Chapter 6 presents experimental work on PA of ^{85}Rb and ^{87}Rb atoms in a MOT. It begins with a review of previous PA experiments in sec 6.1. Experimental details

are outlined such as the intensity of PA light and the scan rates and frequency diagnostics. Ionisation data are presented for excited state electronic potentials used in the ionisation process, over the broadest spectral range reported.

Photo-association data are presented for states below the 5s+5p$_{3/2}$ states with the ionisation laser fixed to a molecular resonance. Trap-loss measurements are used to measure two-body collision rates in Section 6.6. When photo-ionisation data are combined with trap loss data three series of vibrational levels (0_u^+, 1_g and 0_g^-) are readily identified; some of the vibrational levels in the ^{87}Rb isotope are reported here for the first time. These series are consistent with a Near-Dissociation Expansion (NDE) function and C_3 parameters are extracted. However there are significant deviations from such a model and a qualitative description of the interactions that need to be incorporated into a more sophisticated model is presented.

Chapter 7 summarises the main results of the work presented in this thesis. A summary of continuing work, planned experiments and possible future directions for the project is presented.

Chapter 2

Laser Trapping and Cooling of Rb

"OK, what about temperature? What happens if we change it?"

— Ripley, *Alien.*

2.1 Laser Cooling and Trapping

2.1.1 Optical Molasses for a Two Level Atom

For a two level atom with transition frequency ω_a, interacting with counter-propagating laser fields of frequency ω_L, the average scattering force $F_\pm$ is calculated in terms of the photon momentum $\pm\hbar k$ and the average rate of photon absorption. The photon absorption rate is found from the optical Bloch equations for a two-level atom [19]:

$$F_\pm(v) = \pm\hbar k \; \frac{\gamma}{2} \; \frac{I/I_{sat}}{1 + I/I_{sat} + [2(\delta \mp kv)/\gamma]^2} \tag{2.1}$$

where v is the velocity of the atom, k is the photon wave vector, $\delta = w_L - w_a$ is the detuning of the laser frequency from the atomic resonance, γ is the spontaneous decay
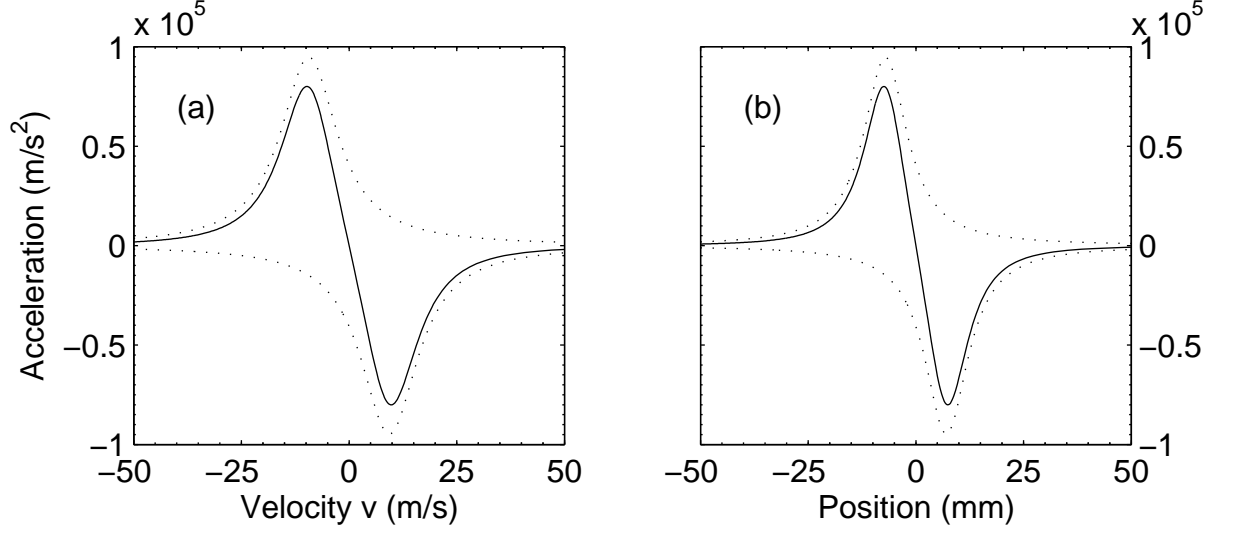
Fig. 2.1: (**a.**) Acceleration as a function of velocity for a two level ^{87}Rb atom in optical molasses and (**b.**) Acceleration as a function of position in an ^{87}Rb MOT where $I = 5I_{sat}$, $\delta = -2\gamma$ and $\frac{dB}{dz} = 12$ G/cm. The dotted lines show the contribution from each counter-propagating beam. The solid line is the total acceleration.

width of the atomic excited state, I is the intensity of the laser beam and I_{sat} is the saturation intensity of the transition.

A Rb atom in optical molasses loses on average $\hbar k$ momentum, or 0.006 m/s per photon absorbed and re-emitted. An atom at room temperature, with average initial velocity 170 m/s will be brought to rest after absorbing and re-emitting 30,000 photons. As a Rb atom can absorb $1/2\tau = 1.8$ million photons/s, this process takes about 1.5 ms, with the atom feeling a force 10,000 times greater than gravity. Figure 2.1a shows the velocity-dependent acceleration on a two-level Rb atom in molasses under our experimental conditions.

2.1.2   Magneto Optical Trapping of Rb

The addition of an inhomogeneous magnetic field to counter-propagating σ^+-σ^- red-detuned cooling light provides a spatially confining force analogous to the velocity

damping force of Equation 2.1.
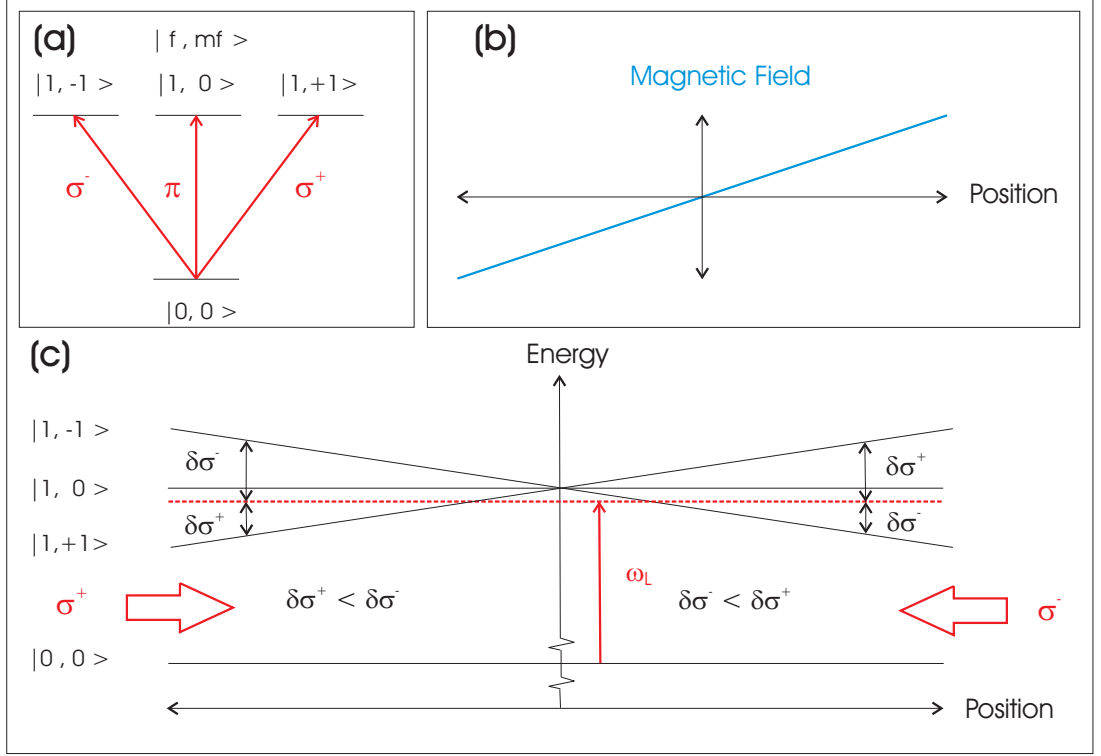
Fig. 2.2: (**a.**) Selection rules for polarised light and magnetic sub-levels for a $|f = 0\rangle \rightarrow |f = 1\rangle$ transition. (**b.**) One dimensional MOT magnetic field configuration (**c.**) One dimensional magneto-optical trapping scheme for a simplified $|f = 0\rangle \rightarrow |f = 1\rangle$ trapping transition. Atoms to the right(left) absorb σ^+ (σ^-) radiation imparting a force towards magnetic field zero at the trap centre.

In a magneto optical trap (MOT) the spatially-dependent Zeeman shifting of magnetic sub-levels is analogous to the velocity-dependent Doppler shifting of the laser light in optical molasses. A one-dimensional MOT configuration for a $|f = 0\rangle \leftrightarrow |f = 1\rangle$ level scheme is depicted in Figure 2.2. Right (left) of the trap centre the positive (negative) magnetic field orientation shifts the negative (positive) m_f states lower in energy, towards resonance with the red-detuned laser light. Due to angular momentum conservation atoms excited to positive (negative) m_f states preferentially absorb σ^- (σ^+) oriented radiation which imparts a net force towards the magnetic field zero at the centre of the trap. With the addition of a magnetic field, the scattering force of

Equation 2.1 becomes:

$$F_{\pm}(v, z) = \pm \hbar k \, \frac{\gamma}{2} \, \frac{I/I_{sat}}{1 + I/I_{sat} + [2(\delta \mp kv \pm \mu'/\hbar \, \frac{dB}{dz} \, z)/\gamma]^2} \qquad (2.2)$$

where B is the magnetic field strength and μ' is the effective magnetic moment for the cooling transition. Figure 2.1(b) shows the force on a stationary two-level ^{87}Rb atom for our experimental parameters.

In practice the one dimensional molasses and MOT schemes are usually applied in three orthogonal directions giving three dimensional cooling and confinement. The trapping and cooling transition used for ^{87}Rb (^{85}Rb) is $|5s_{1/2}, f = 2(3), m_f = 2(3)\rangle \leftrightarrow |5p_{3/2}, f' = 3(4), m'_f = 3(4)\rangle$ which is labelled in the energy level diagram of Figure 2.3.

For ^{87}Rb atoms excited to the $|f' = 3, m'_f = 3\rangle$ level the only allowed decay channel is back to the $|f = 2, m'_f = 2\rangle$ so the cooling transition is closed. However the trapping laser is only 42 natural linewidths detuned from the f'=2 state, so off-resonant excitations populate the f'=2 state. Once excited to the f'=2 state atoms can decay back to the cycling transition or to the dark f=1 ground where they no longer interact with the trapping laser and are lost from the trap. The dark-state optical pumping rate is even greater for ^{85}Rb where the hyperfine splitting is smaller. This problem is solved by applying additional light at another frequency, called re-pump light, which couples the dark ground-state back to an upper level which can decay back into the trapping cycling transition. The repump transitions are labelled in Figure 2.3.

2.1.3 The Doppler Limit and Sub-Doppler Cooling

A MOT governed by Equation 2.2 would in principle cool atoms to absolute zero. In practice the temperature is limited by heating arising from the atomic recoil accompanying each photon re-emission following absorption. Equating the cooling rate from Equation 2.2 with the heating rate arising from atomic recoils gives the
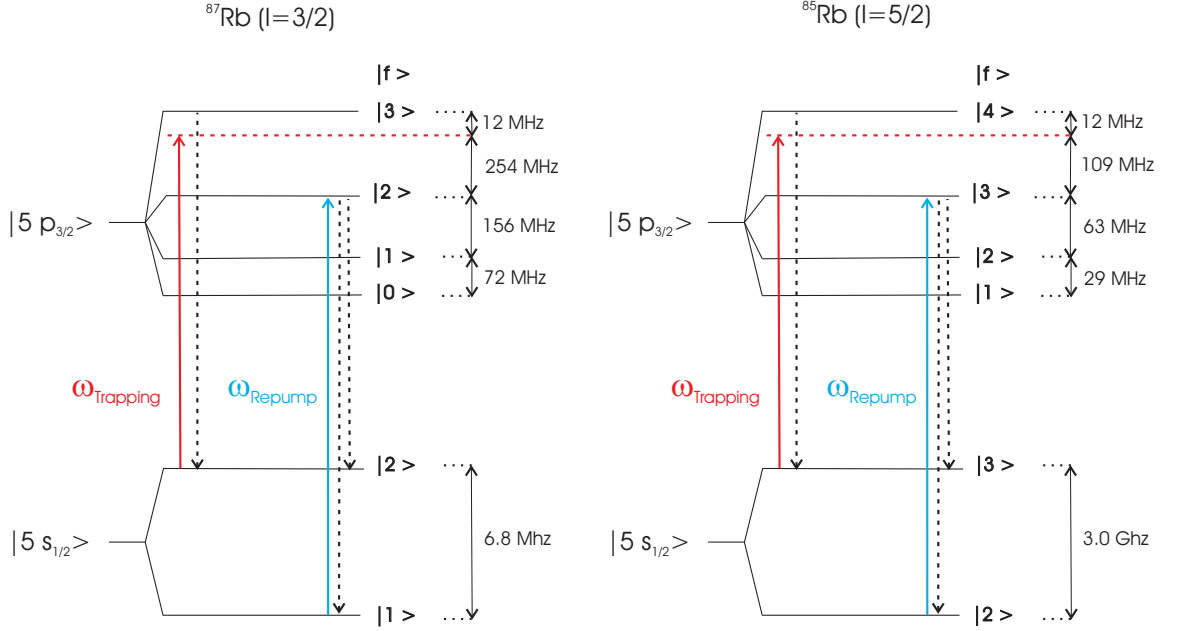
Fig. 2.3: Level structure of ^{85}Rb and ^{87}Rb with trapping and repumping transitions indicated

MOT equilibrium temperature T_D known as the Doppler temperature [20].

$$k_B T_D = \frac{\hbar\gamma}{8}\left(\frac{2|\delta|}{\gamma} + \frac{\gamma}{2|\delta|}\right) \tag{2.3}$$

This model, which neglects stimulated emission, is valid at low optical intensities. It predicts a minimum Doppler temperature of 143 μK for Rb, when $\delta = -\gamma/2$. Our experimental conditions $\delta = -2\gamma$ correspond to a Doppler limited temperature of 300 μK.

The MOT configuration provides an additional cooling mechanism known as polarisation gradient cooling. It arises from the non-adiabatic response of atoms to local spatial polarisation gradients. Two circularly polarised counter-propagating beams of the same intensity produce a linear polarisation everywhere, with the direction rotating by 2π over every optical wavelength. A schematic of one-dimensional polarisation gradient cooling for a $|f = 1\rangle \rightarrow |f = 2\rangle$ transition is shown in Figure 2.4. Atoms moving along

15

the polarisation gradient are optically pumped into positive or negative m_f states where they preferentially absorb σ^+ or σ^- photons opposing their motion. The preferential absorption is determined by the Clebsch-Gordon coefficients for the transitions between magnetic sub-states for σ^+ and σ^- radiation. The cooling mechanism is analogous to optical molasses and magneto-optical trapping, except it is the velocity dependent pumping of magnetic sub-levels, rather than the Doppler or Zeeman shift, that causes the selective absorption of radiation.
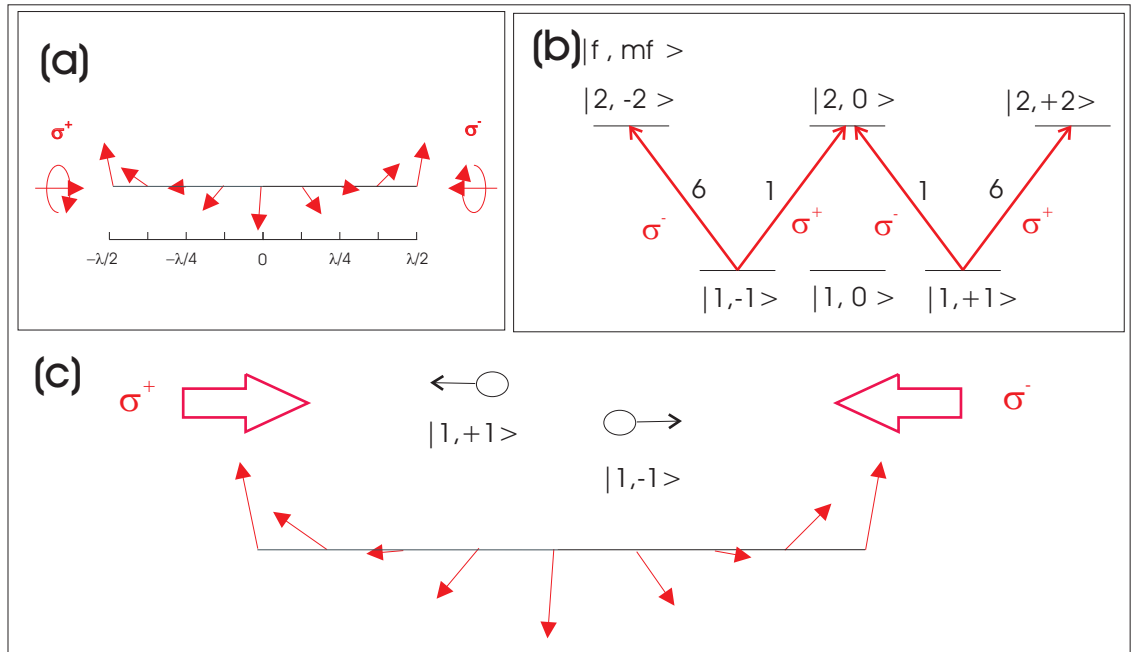
Fig. 2.4: (**a.**) Counter-propagating light with opposite circular polarisation produces rotating linearly polarised light. (**b.**) Transition strengths for σ^+ and σ^- radiation. (**c.**) Atoms moving to the right (left) in the linearly polarisation rotating field are pumped into the negative (positive) m_f states and preferentially absorb σ^+ (σ^-) radiation.

Similar to optical molasses, the temperature for polarisation gradient cooling is limited by heating arising from atomic recoil. The equilibrium temperature however is lower, since the σ^+/σ^- absorption selectivity is greater for the magnetic sub-level population imbalance than for the Doppler-shifted levels.

For the simplified case of one-dimensional polarisation gradient cooling and for the

$|f = 1\rangle \rightarrow |f = 2\rangle$ transition discussed above, an expression for the equilibrium temperature T_{pgc} is [9]:

$$k_B T_{pgc} = \frac{\hbar \gamma^2 I/I_{sat}}{2|\delta|} \left(\frac{29}{300} + \frac{254}{75} \frac{\gamma^2/4}{\delta^2 + \gamma^2/4} \right) \qquad (2.4)$$

From Equation 2.4 it is clear the optimum experimental parameters for the lowest temperature due to polarisation gradient cooling are low intensity $(I \ll I_{sat})$ and large detuning $(\delta \gg \gamma)$. These conditions are different to the optimum conditions for operation of the MOT. When $\gamma/\delta \rightarrow 0$ the temperature limit for polarisation gradient cooling is close to the single photon recoil limit, which is the recoil energy released by the emission of a single resonant photon, 0.4 μK for Rb.

In single-shot experiments, atoms are first collected with optimum loading conditions for a MOT. Phase space density is then maximised with a separate polarisation gradient cooling stage using reduced light intensity and increased detuning. This approach is less practical for continuous trap-loss experiments; instead intermediate values of intensity and detuning are chosen so that there is a balance between low temperatures and high loading rates.

2.1.4 Limits of Laser Cooling

The temperature of the MOT is limited by heating from atomic recoil. For our experimental conditions the Doppler limited temperature is 300 μK and the polarisation gradient cooling limit is 20 μK.

The number of atoms in our vapour cell MOT is limited by losses from background collisions. When loading from a thermal vapour at a given vapour pressure atoms are loaded at a constant rate. The rate of atoms lost from the trap due to collisions is proportional to the number of atoms in the trap, so that an equilibrium atom number is reached. For our vapour cell MOT the equilibrium number is limited by the vapour

pressure, which also determines the loading rate of the trap.

The density of the MOT is limited by radiation pressure between trapped atoms. For low atom numbers the size of the MOT is determined by the trapping force and the temperature of the atoms. In this regime the size of the MOT is independent of the atom number and the density is increased as more atoms are loaded into the trap. As the density increases radiation emitted by atoms is reabsorbed leading to a repulsion between atoms. The equilibrium density where the repulsive radiation pressure equals the trapping force of the MOT can be approximated for a two level atom as [21]:

$$n_{max} \approx 12 \left(\frac{g u_B (dB/dz) I_{sat}}{\hbar^2 k c \gamma^2} \right) \frac{(\Omega^2/2 + \delta^2 + \gamma^2/4)^3 2(2\Omega^2 + \gamma^2)}{(5\gamma^2 + 4\delta^2)\delta\gamma(\Omega^2/2)^2} \qquad (2.5)$$

where g is the Lande g-factor for the ground state of the cooling transition and Ω the Rabi frequency. This expression breaks down at very high and low intensities, but provides a good order of magnitude estimate under our experimental conditions [21]. Under our experimental conditions this gives a maximum density of approximately 3×10^{11} atoms/cm^3, though experimentally measured densities are an order of magnitude lower. Once this equilibrium density is reached, loading more atoms into the MOT increase the spatial size of the MOT but not the atomic density.

2.2   Magneto Optical Trap Experimental Set-up

The MOT used in these experiments and described in detail in the rest of this chapter has typically 7×10^6 atoms with a peak density of 10^{10} atoms/cm^3, at a temperature of 100 μK. The trap is loaded from a thermal vapour, with loading rate 1.5×10^5 atoms/s. By altering the applied laser frequencies the MOT can trap either of the two stable isotopes ^{85}Rb or ^{87}Rb under similar experimental conditions, without realignment.

2.2.1   MOT Trapping Light

External Cavity Diode Lasers

The light for the MOT and diagnostics is generated from grating-stabilised external-cavity diode lasers. The external cavities are formed by a diffraction grating in the Littrow configuration [22], with the zeroth order taken as the output and the first order fed back into the diode.

The trapping light is from a commercial Toptica DL100 system which provides 45 mW of output power. This passes through two Acousto-Optical Modulators (AOMs) before injection locking a temperature-controlled bare high-power slave laser diode (Sharp Microelectronics GH0781JA2C 120 mW). Two additional diodes (Sanyo DL7140-201 80 mW) are grating stabilised in external cavities. They are used as the re-pump laser and a probe laser which is required for absorption diagnostics.

Stabilising Diode Lasers

All of the diode lasers are actively temperature-stabilised and current-stabilised. In addition the trapping and re-pump lasers are actively stabilised to an atomic hyperfine resonance. An error signal is generated from saturated absorption spectroscopy in a vapour cell, and fed back electronically to the diode currents and piezo transducers (PZTs) controlling the angle of the external cavity diffraction grating and the cavity length.

The saturated absorption set-up for the trapping laser is shown in Figure 2.6. Probe light from the diode laser with frequency ω_0 passes through a vapour cell and is collected on a photodiode. Pump light is taken from the same diode laser but is double-passed through an acousto-optic modulator with central frequency ω_{AOM}, before entering the vapour cell counter-propagating with the probe.

Atoms in the vapour cell see a probe with frequency ω_0 and a pump with frequency $\omega_0 - 2\omega_{AOM}$ where the negative sign is a consequence of choosing the negative diffracted order, and the factor of two arises from double passing the AOM. The only atoms which are simultaneously resonant with the pump and the probe are those with a velocity component $v = -c \times \omega_{AOM}/\omega_0$ in the direction of the pump laser. This corresponds to a Doppler shift of $+\omega_{AOM}$ for the pump and $-\omega_{AOM}$ for the probe. When the probe laser is resonant with an atomic transition at frequency ω_a in the atom's frame of reference, the probe laser is at frequency $\omega_0 = \omega_r - \omega_{AOM}$ in the laboratory frame of reference.

A 20 kHz frequency modulation is added to the central frequency of the nominally 100 MHz AOM. The saturated absorption signal which contains this modulation is mixed with the modulation itself in a lock-in amplifier. The output of the lock-in amplifier which is a dispersion curve that crosses zero on an atomic resonance, is fed back to the laser current and the PZT.

Light from the master laser double passes an additional tuning AOM and is then used to injection lock a temperature stabilised bare slave diode laser. Applying anti-reflection coating on the front surface of the laser diodes (custom coated at the Lebedev Institute) to a fraction of a per cent reflectivity improved the tuning range of the slave diode considerably. Injection locked anti-reflection coated slave diodes can follow the master laser over the entire [87]Rb ground state hyperfine splitting, i.e. 6.8 GHz, mode-hop free at a fixed temperature and injection current.

The error signal used to lock the re-pump laser was derived from the side of a saturated absorption peak and fed back to a PZT controlling the external cavity. The actual lock point is of order 5 MHz from the line centre of the Doppler-free absorption peak.

The probe laser was scanned across atomic resonances to determine relative atomic populations in the MOT, and to determine the peak-absorption which was used to determine a column density and infer the peak atomic density of the atomic cloud.

Locking schemes for ^{85}Rb and ^{87}Rb

It is possible to trap either isotope without any realignment by locking the laser frequencies to a different feature and adjusting the tuning (80±20 MHz) and dither AOM (110±20 MHz) frequencies. Figure 2.5 shows the spectroscopy of the master and slave lasers for each locking scheme. The peaks labelled with two quantum numbers are a result of interaction with two separate transitions, the so-called crossover peaks which are located halfway between the two designated transitions. We lock to the most prominent crossover peaks and then shift the laser to the desired frequency using AOMs. For ^{87}Rb the master is locked to the $|f = 2\rangle \rightarrow |f' = 3-2\rangle$ crossover, 133 MHz below the trapping transition. For the ^{85}Rb locking scheme the master is locked to the $|f = 3\rangle \rightarrow |f' = 4 - 2\rangle$ crossover which is 102 MHz detuned from the trapping transition.

Table 2.1: Frequency Shifts For ^{87}Rb and ^{85}Rb Locking Schemes

Shift	^{87}Rb	^{85}Rb
Detuning Of Crossover From Resonance	-133 MHz	-102
Detuning From Dither AOM	-91 MHz	-103 MHz
Detuning From Tuning AOM	2 x 106 MHz	2 x 96.5 MHz
Total Shift from resonance	-12 MHz	-12 MHz

2.2.2 Optical Setup

The optical setup shown in Figure 2.6 extends over two optical tables which are separated by another experiment. As a result the tables were not tied together or "floated" on compressed air to provide pneumatic isolation from external vibrations. Light was transferred between tables through free space without any noticeable limitation of the stability; however the lock of the diode lasers was less robust with the tables unfloated.

All of the MOT lasers and optics are on the same table as the vacuum chamber,
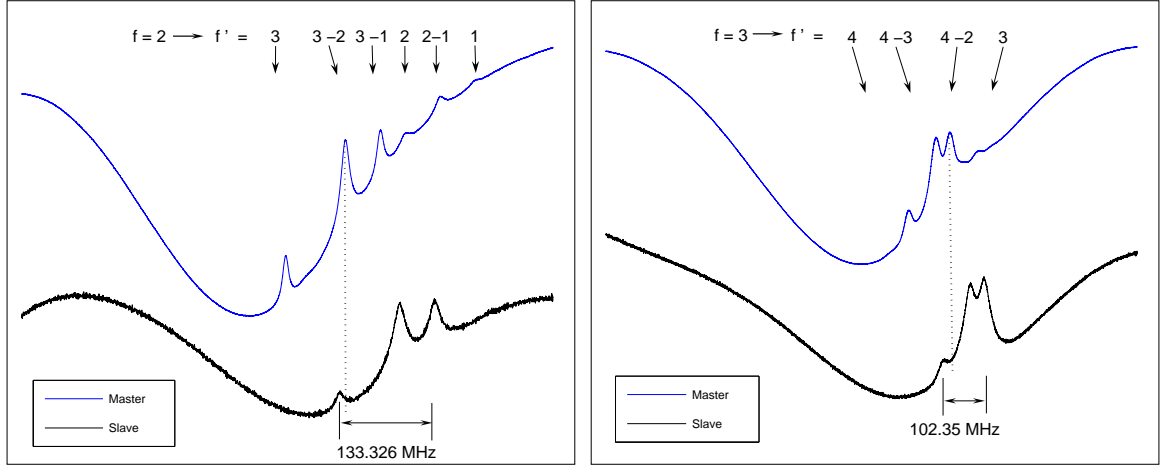
Fig. 2.5: Spectroscopy for ^{87}Rb (left) and ^{85}Rb (right) locking schemes. When the master-laser frequency is locked to the $f' = 3 - 2$ crossover for ^{87}Rb, or the $f' = 4 - 2$ crossover for ^{85}Rb, the frequency of the slave laser is red-detuned 12 MHz from the trapping transition.

increasing stability due to common mode rejection of some vibrations. The trapping laser passes through an optical isolator and then through a nominally 100 MHz AOM as part of the locking scheme described in Section 2.2.1. A portion of the trapping light is also picked off and passed through a nominally 80 MHz AOM before 1 mW of power is used to seed a slave laser. The second AOM gives the flexibility to easily switch between the two isotopes without any realignment as shown in Figure 2.5.

The injection-locked slave produces 100 mW. With a single -45 dB optical isolator feedback was observed in the slave diode when the light was retroreflected from the MOT, so a second isolator was added giving a total of 80 dB attenuation. Light from the slave is then reshaped with anamorphic prisms and expanded to 25 mm diameter with a telescope. This limit was imposed by the cost of large diameter polarisation optics; however the intensity in the trapping beams is close to the transition saturation intensity 3.6 mW/cm^2 for the trapping cycling transition [23].

After the telescope the trapping light is combined with the repump light on a polarising beamsplitter. There are no AOMs in the beam path of the slave or repump lasers; switching is carried out with mechanical shutters placed in the focus of the beam

Ti:Sapphire Table
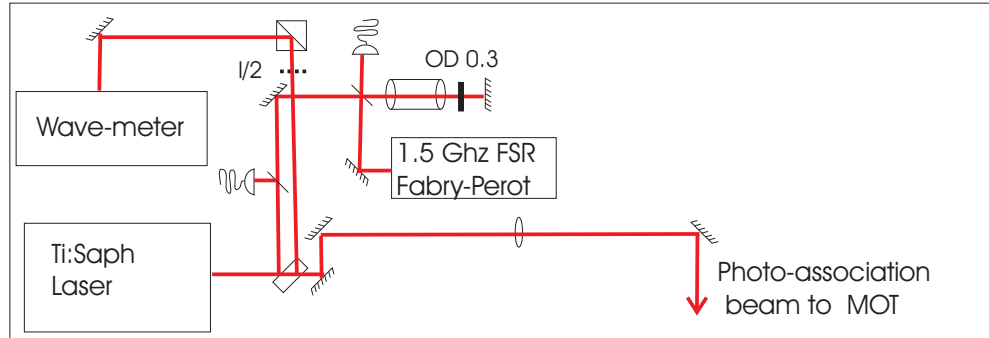
Main Table
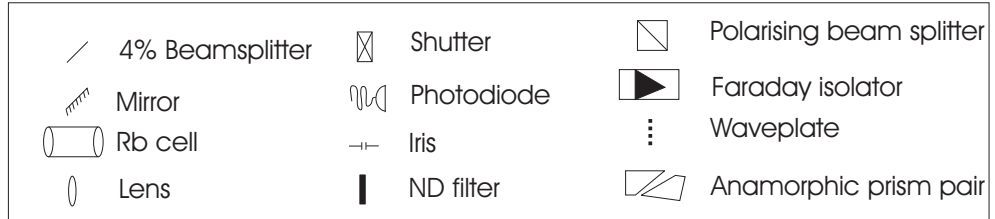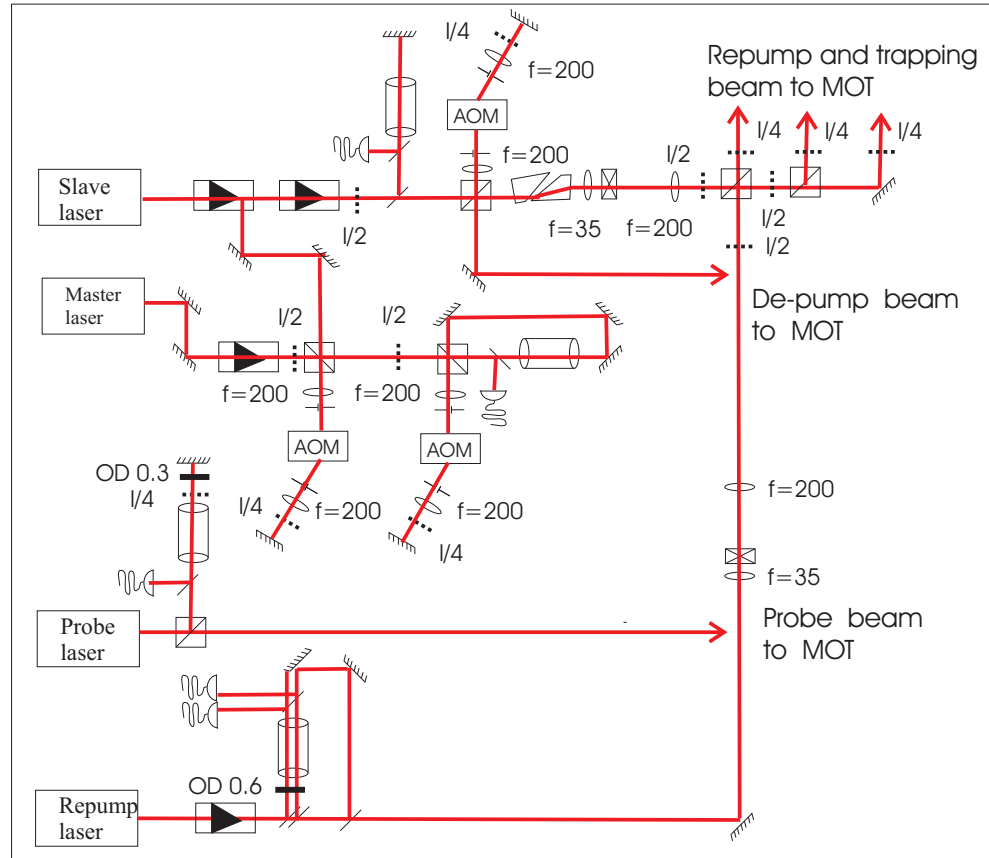
Fig. 2.6: Optical Setup.

expansion telescopes.

The trapping and repump light is divided into three separate beams with half-wave plates and polarising beam-splitters. Each beam is circularly polarised with a quarter-wave plate before entering the chamber along three orthogonal axes. After passing through the vacuum chamber each beam double passes an additional quarter-wave plate and is retro-reflected with opposite circular polarisation. The power in each MOT beam is 15 mW, combining in the centre to be 90 mW in a capture volume of 8.6 cm^3 corresponding to a capture velocity of approximately 30 m/s.

2.2.3   Vacuum System and Experimental Geometry

The vacuum system depicted in Figure 2.7 is constructed from grade 316 stainless steel. It is a cylindrical chamber capped with two 6" windows and has twelve flanges pointing radially outwards from the chamber centre, 8 x 2.75" and 4 x 4.5." Six flanges are used for orthogonal MOT laser beams, two for photoassociation light, one for a cold cathode vacuum gauge and one for an ion detector. An additional port connected to a five-way cross houses the alkali metal dispensers and vacuum pumps. In addition, two cameras and a fluorescence collection system share the 6" window directly above the MOT.

Ultra high vacuum (UHV) is maintained by a 50 l/s ion pump, and a 50 l/s turbo pump is added to an all metal gate valve during baking. The chamber was baked at 150 °C for 72 hours. Commercial UHV ZnSe view ports were installed to transmit mid infra-red laser light for the implementation of a 1060 nm wavelength quasi-electrostatic dipole trap. The metal to ZnSe seal failed after baking within the thermal gradient and temperature specifications of the windows. Home made UHV ZnSe vacuum seals using solder have been reported by other groups [24]; however in our experiment these windows were replaced with standard glass windows.

Pressure is measured by a cold cathode gauge inside the chamber on the opposite side to the pumps. The background pressure after baking and removing the turbo pump
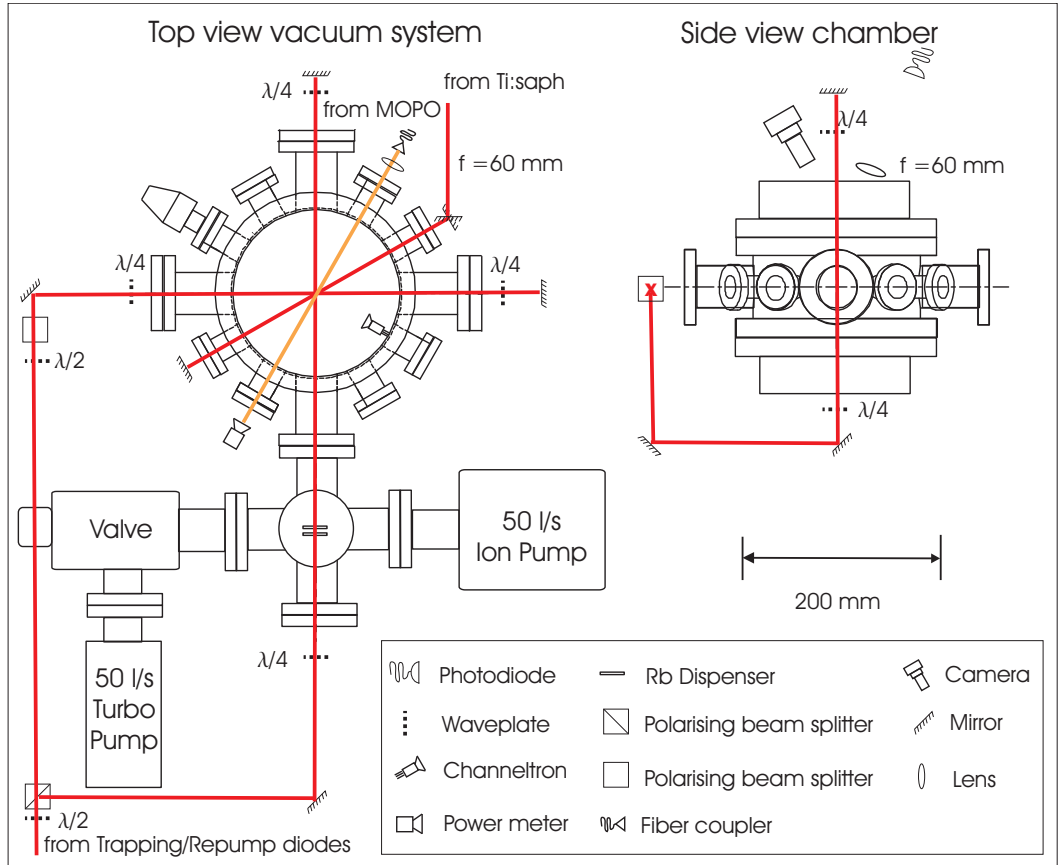
Fig. 2.7: Vacuum and experimental geometry.
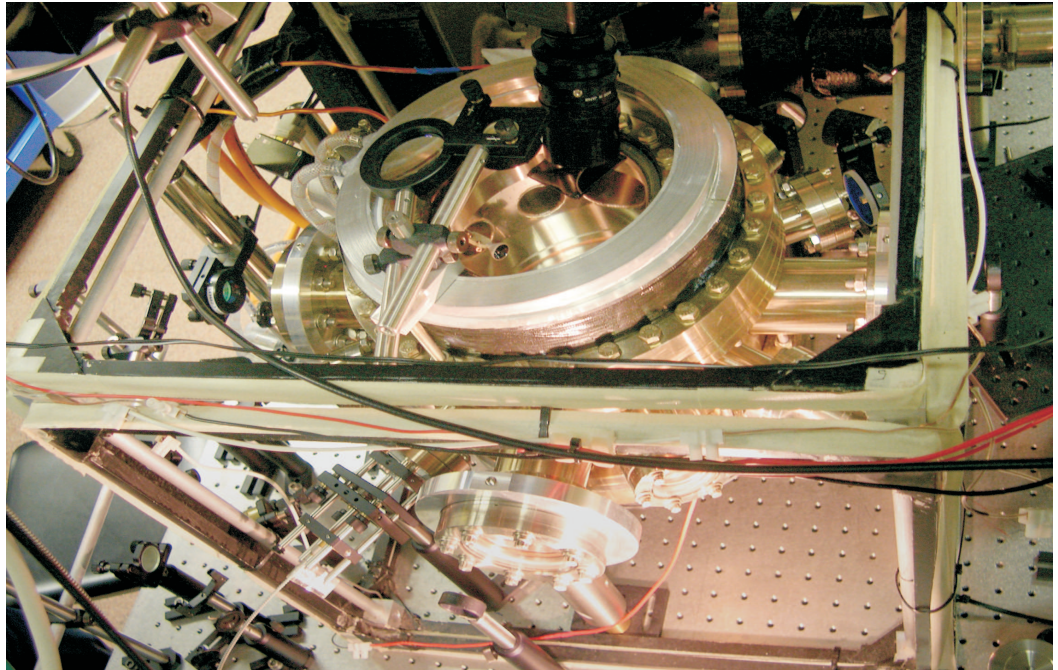
Fig. 2.8: Photo of UHV chamber. The channeltron-electron-multiplier, MOT coils, ionisation fibre, CCD camera, MOT optics and ion-pump can all be seen.

25

was 1.4×10^{-10} Torr.

2.2.4   Rb Vapour Pressure

Rb is released into the chamber by two Rb alkali metal dispensers (SAES Getters Rb//NF/5.4/17/FT10+10) which sit 30 cm from the centre of the main chamber. The dispensers were operated continuously with 3.5 A applied through them. From a base pressure of 1×10^{-10} Torr the pressure rises by an order of magnitude over one hour when the dispensers are activated. We have observed loading rates still slowly increasing twenty hours after activating the dispensers. Experiments are typically run with a Rb partial pressure of 5×10^{-9} Torr, corresponding to a 1/e loading time for the MOT of 35 seconds.

2.2.5   Magnetic Field Cancellation and Trapping

External magnetic fields arising from the Earth, nearby pumps and equipment are cancelled using three orthogonal pairs of square Helmholtz coils outside the UHV chamber. The MOT field gradient is generated by magnetic field coils which also sit outside the UHV chamber over the 152 mm windows, see Figs. 2.7 and 2.8. The chamber constrains the separation of the magnetic field coils to greater than 203 mm, and the inner radius to greater than 152 mm.

The MOT coils are wound from hollow core square-section copper wire with inner dimension 1.6 mm and outer dimension 3.2 mm. Each coil consists of 88 turns with a 178 mm radius and the coils are separated by 229 mm. In anti-Helmholtz configuration, the field gradient at the centre of the chamber is 0.45 Gauss/cm/A. The coils are typically run at 25 A giving a field gradient of 11.3 G/cm in the radial direction, but currents up to 100 A have been applied, creating a field gradient of 45 G/cm. The coils are connected to a power supply in series and are switched with a power MOSFET,

which gives a switching time of approximately 300 μs which is fast compared to ballistic expansion times of milliseconds.
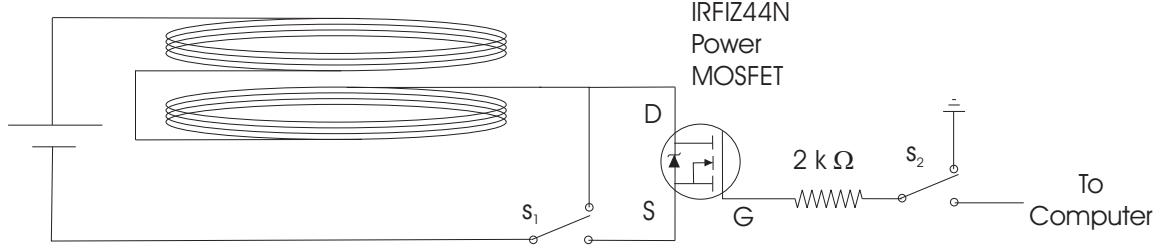
Fig. 2.9: Computer controlled switching circuit for MOT coils, with double pole switch s_1.

The coils are water cooled, with water passed through the hollow core of the wire and through the coil former which encloses the coils. The aluminium former dissipates most of the heat; however the relatively low flow rate through the wire provides good thermal contact to the centremost wires not in contact with the former. When they are cooled the wires reach an equilibrium temperature of 10 degrees above room temperature when passing 25 A through them. When the coils were run continuously at 65 A the temperature rose by 45 degrees in 5 minutes.

2.3   Loading the MOT

2.3.1   Loading From a Thermal Vapour

Assuming that every atom which enters the trapping volume with a velocity smaller than the MOT capture velocity ($v < v_c$) is trapped, the loading rate A is found by integrating over the trap surface ($SA = 4\pi r^2$):

$$A = \pi r^2 \int_0^{v_c} v \ n(v) \ dv \tag{2.6}$$

where $n(v)$ is the Maxwell-Boltzmann distribution of the thermal background vapour given by:

$$n(v) = n_o 4\pi v^2 \left(\frac{m}{2\pi k_B T}\right)^{3/2} e^{\frac{-mv^2}{2k_B T}} \tag{2.7}$$

and n_o is the atomic density, m the atomic mass and T the background vapour temperature.

The capture velocity v_c can be approximated as the velocity of the atom which is stopped in a distance $2r$, by a force equal to half the maximum scattering force [21]. From Figure 2.1 with 25 mm diameter trapping beams the capture velocity is 30 m/s. The fraction of atoms captured from a thermal background of Rb vapour at 295 K is 0.15% and is shown in Figure 2.10.
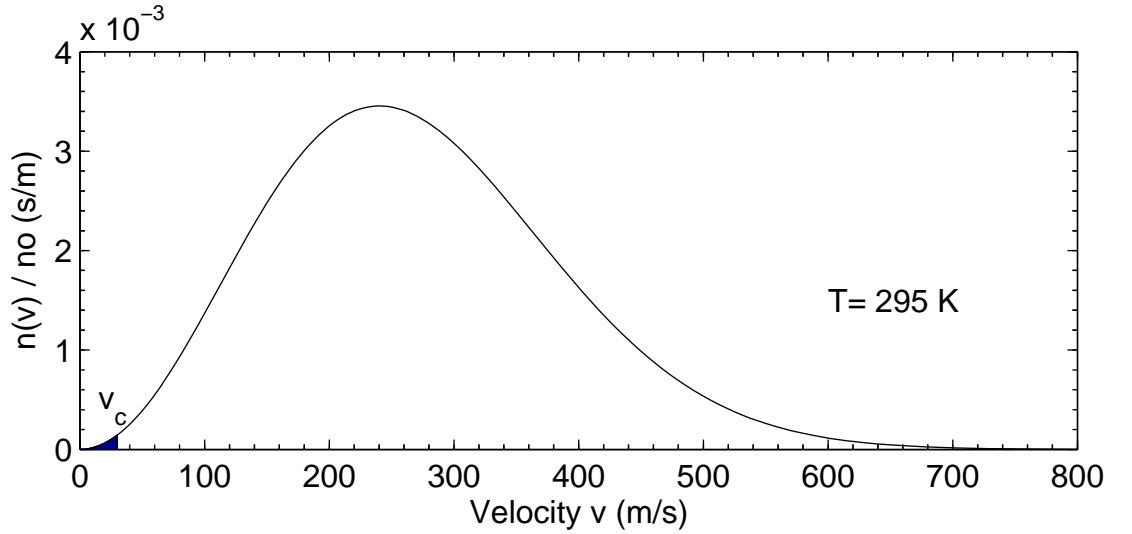
Fig. 2.10: Velocity Distribution of Room Temperature Rb Vapour. The shaded region indicates atoms with velocity less than the capture velocity of the MOT.

2.3.2 Loading and Collision Rates

The number of atoms N in the MOT is described by a rate equation with atoms captured from the background gas at a constant rate A and lost from the trap at a rate B proportional to the number of atoms in the trap [25]:

$$\frac{dN(t)}{dt} = A - B\ N(t) \tag{2.8}$$

This equation has the solution:

$$N(t) = N_{eq}\ (1 - e^{-t/\tau}) \tag{2.9}$$

where $N_{eq} = A/B$ and $\tau = 1/B$. The rate of trap-loss arising from collisions between two trapped atoms C has a density-squared dependence. Introducing intra-trap collisions into the model the rate equation becomes:

$$\frac{dN(t)}{dt} = A - B\ N(t) - C \int n^2(x)\ d^3x \tag{2.10}$$

When the volume of the trap V is constant this can be rewritten as [26]:

$$\frac{dN(t)}{dt} = A - B\ N(t) - C/V\ N^2(t) \tag{2.11}$$

which has the solution:

$$N(t) = \frac{\sqrt{D}V}{2C}\ tanh\left(\frac{\sqrt{D}(t + t_0)}{2}\right) - \frac{BV}{2C} \tag{2.12}$$

with $D = 4AC/V + B^2$ and $t_0 = (2/\sqrt{D})tanh^{-1}(B/\sqrt{D})$. In steady state:

$$N = \frac{V(\pm\sqrt{D} - B)}{2C} \tag{2.13}$$
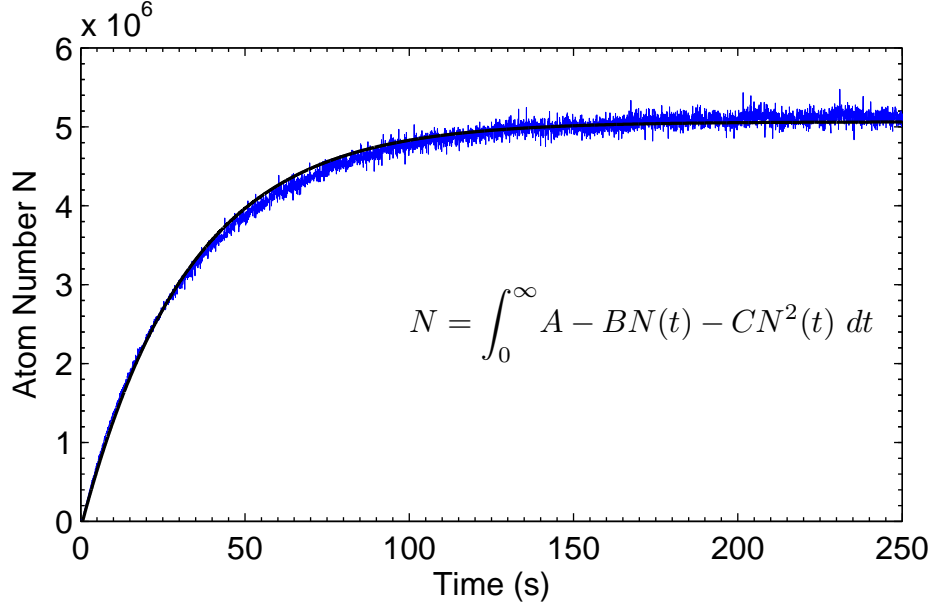
Fig. 2.11: MOT Loading Curve for 5 x 10^{-10} Torr Rb Vapour Pressure.

The loading curve in Figure 2.11 was taken under normal experimental conditions. It corresponds to a loading rate A of 1.5×10^5 atoms/s and a background collision loss rate B of 0.03 s^{-1} which corresponds to 1.5×10^5 atoms/s when the MOT is in equilibrium. The two-body loss rate constant $C/V = 7.7 \times 10^{-12}$, so that the loss rate (C/V N^2) is 190 atoms/s at equilibrium. The effective volume V can be found from Equation 2.16:

$$V = \frac{N^2}{\int n^2(x, y, z) \; dxdydz} \tag{2.14}$$

Under our experimental conditions the effective volume is 7.6 mm^3 giving a rate constant C of 0.001 m$^3s^{-1}$. The loading time constant τ from the fit in Figure 2.11 is 35 s.

2.4 MOT Diagnostics

Fluorescence is continuously monitored by a charge-coupled device (CCD) video camera, and imaged onto a photodiode, as shown in Figure 2.8, which provides an *in situ* measure of atom number.

Real time determination of the MOT's volume and peak density requires *in situ* image processing. Ballistic expansion temperature measurements requires an external triggering capability faster than the time for the untrapped cloud to diffuse, on the order of ms. An EDC-2000N CCD camera with 10 bit resolution and external triggering is used for these measurements. The camera is linked to two computers, both interfaced with LabView software. One computer controls the timing of experiments acting as a trigger on the camera, the second captures the image and performs *in situ* signal processing to determine atom number, trap volume, peak density, and temperature. In addition the absorption of the probe beam is used to determine column densities, peak atomic densities and energy level distributions when scanned over resonances.

2.4.1 Atom Number and Density

Ignoring the effect of magnetic fields and sub-Doppler processes and assuming purely radiative damping, the total power scattered (P) over a solid angle of 4π by N atoms in counter-propagating $\sigma^+ - \sigma^-$ molasses beams is:

$$P = N \frac{\Gamma/2(I/I_{sat})\hbar\omega}{(1 + 4(\delta/\Gamma)^2 + I/I_{sat})} \tag{2.15}$$

where I_{sat}=3.58 mW/cm^2 for the ^{87}Rb $|f = 2, m_f = 2\rangle \rightarrow |f = 3, m_f = 3\rangle$ cycling transition.

A 51 mm diameter, 60 mm focal length lens placed 120 mm from the MOT is used to image the light onto a photodiode collecting 1.1 % of the emitted power. After

reflections from glass surfaces, under typical experimental conditions 250 nW of light is collected on the photodiode, corresponding to 7×10^6 atoms.

The atomic density is obtained from fluorescence images, with the signal processing automated with LabView software. The atomic distribution in the MOT is treated as a three-dimensional Gaussian distribution:

$$n(x, y, z) = \frac{N}{(2\pi)^{3/2}\sigma_x\sigma_y\sigma_z} \; e^{-\left(\frac{x^2}{2\sigma_x^2}+\frac{y^2}{2\sigma_y^2}+\frac{z^2}{2\sigma_z^2}\right)} \tag{2.16}$$

where N is the atom number and $n_o = \frac{N}{(2\pi)^{3/2}\sigma_x\sigma_y\sigma_z}$ is the peak atomic density of the distribution.
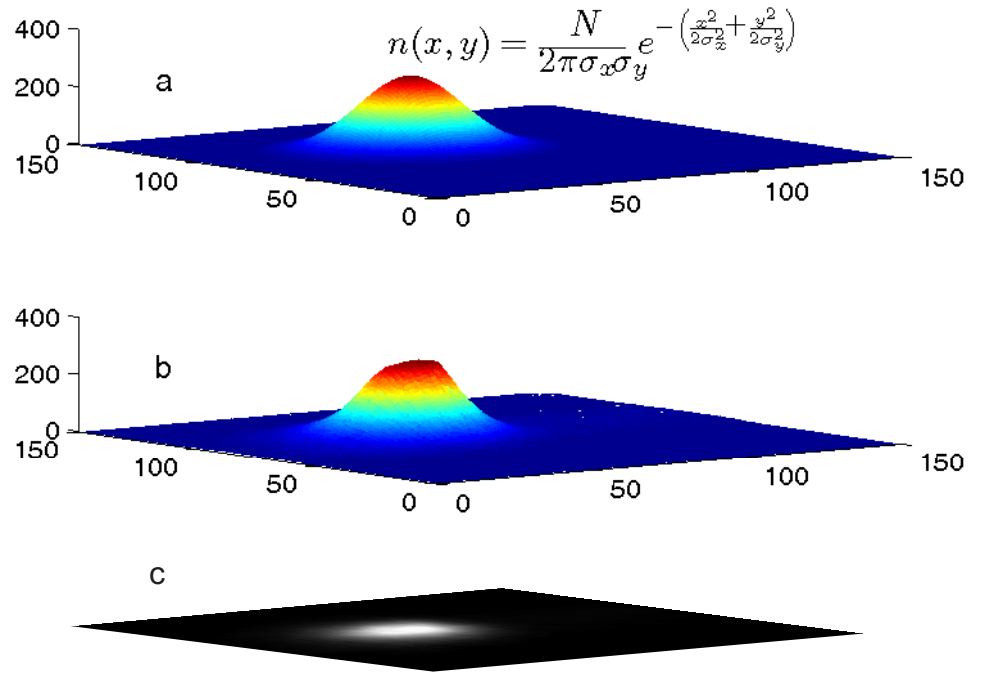
Fig. 2.12: a) two-dimensional gaussian fit to a MOT image b) MOT image with intensity depicted on the z axis c) a two-dimensional image of the MOT. Intensity units are arbitrary, and the x and y units are pixels.

The code which determines N_0 first locates the central peak of the cloud and then takes

two orthogonal cross-sections in the x and y directions. One-dimensional Gaussian profiles are then fitted to determine σ_x and σ_y. In the absence of any information on the axis orthogonal to the plane of the image, σ_z is taken as the average of σ_x and σ_y which typically differ by 20 %. Atom number N is determined by integrating the total number of counts on the CCD and using Equation 2.15. Peak density n_0 is then calculated from N, σ_x, σ_y and σ_z.

Under typical experimental conditions the MOT has 7×10^6 atoms distributed with $\sigma = 3.9 \times 10^{-2}$ cm giving a peak density of $\sim 10^{10}$ atoms/cm^3.

2.4.2 Temperature
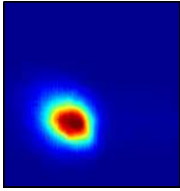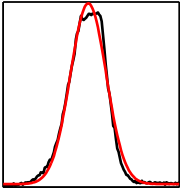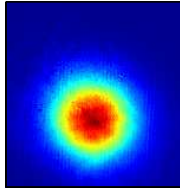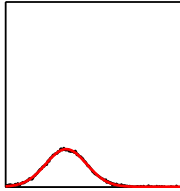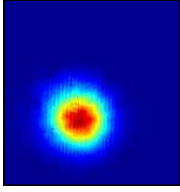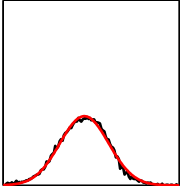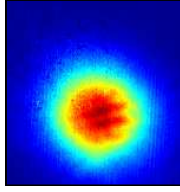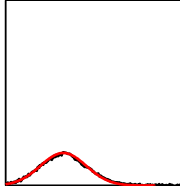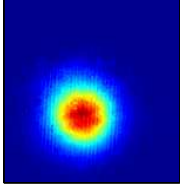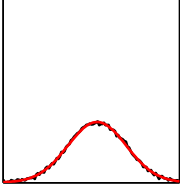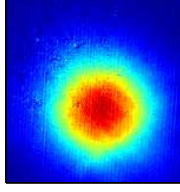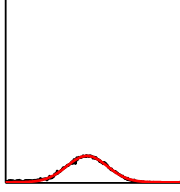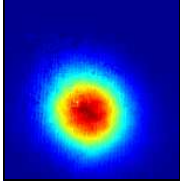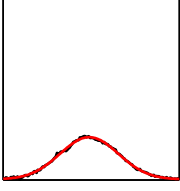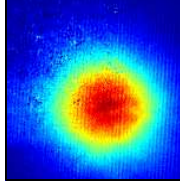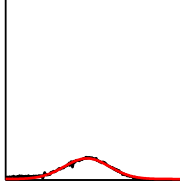
The MOT temperature was determined from the free space ballistic expansion of the cloud. The magnetic field coils, trapping and re-pumping light were switched off; with the switching time of the field coils and of the mechanical light shutter are of order 300 μs. After a delay τ, the camera shutter is opened, the trapping light is switched on and an image is captured. Images and corresponding cross-section with Gaussian fits are shown in Table 2.2.

Atoms in the cloud are initially distributed in a Gaussian profile. The cloud expands with the Maxwell-Boltzmann velocity distribution of the atoms. The most probable speed of atoms at temperature T is $v_0 = (2k_BT/m)^{1/2}$. Assuming no collisions, the 1/e radius of a cloud of atoms with mass m after expansion time τ from an initial 1/e radius r_o is given by [27]:

$$r(\tau)^2 = r_o^2 + 2k_BT/m\tau^2 \tag{2.17}$$

Figure 2.13 shows a fit of Equation 2.17 to the ballistic expansion data. The fit corresponds to a temperature of 120±15 μK. This temperature is below the Doppler limit for these experimental conditions derived in Section 2.1.3; so sub-Doppler cooling

Table 2.2: Ballistic expansion false-colour images of the MOT cloud τ ms after release. A Gaussian is fitted to the cross section to determine the 1/e radius $r=\sqrt{2}\,\sigma$.

τ ms	MOT Image	Cross-section	r μm	τ ms	MOT Image	Cross-section	r μm
0			552	4			940
1			615	5			1020
2			735	6			1082
3			781	7			1102

is responsible for a significant reduction in the temperature of the cloud.

The MOT temperature is still above the 20 μK recoil limit for this system, since the laser is detuned only two natural line-widths from resonance. To cool towards the recoil limit requires large laser detuning and a low trapping light intensity; however these conditions also correspond to a low capture velocity, loading rate and atom number.
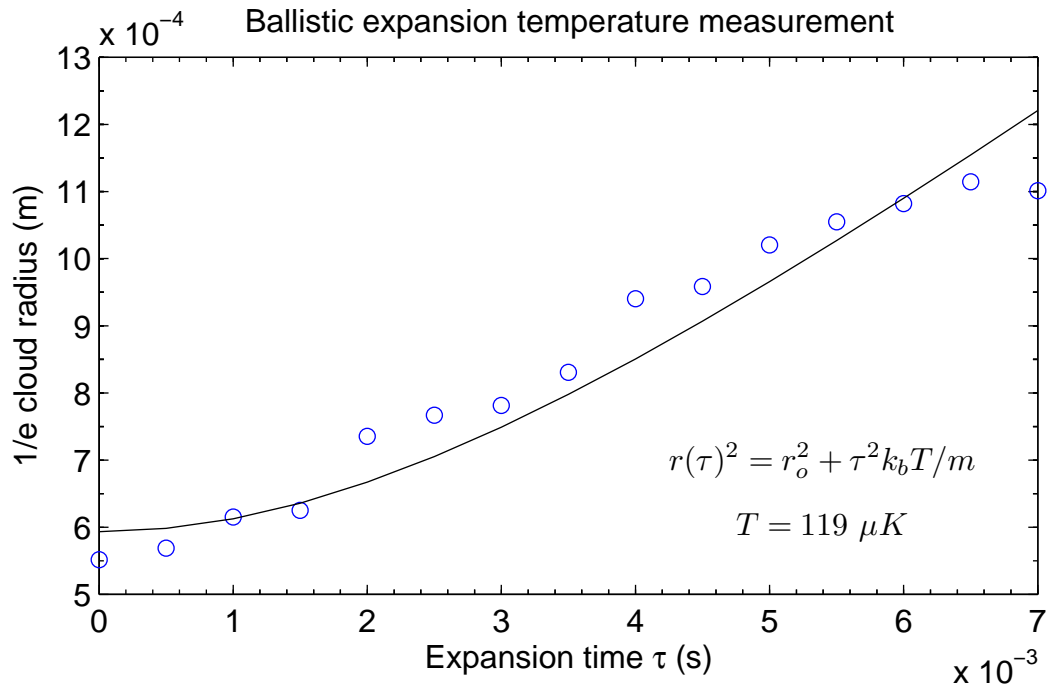
Fig. 2.13: Ballistic expansion of the MOT cloud after release, corresponding to $120\pm15\ \mu$ K.

Chapter 3

Ionisation Detection

"Unfortunately real instruments seldom equal the projected performance of a perfect model and the model 162 is no exception"

— *p. IV-24, Model 162 Boxcar Integrator Operating and Service Manual.*

3.1 Ionisation and Fluorescence Detection

Ionisation detection is a powerful detection technique, used in these measurements in conjunction with fluorescence, trap loss detection. The ion detection system has higher (single ion) sensitivity than the fluorescence based trap-loss spectroscopy. The implementation of time-of-flight (TOF) discrimination techniques allow molecular ions to be detected against a large background of atomic ions. In contrast, trap-loss measurements require a significant fraction of trapped atoms to be converted into molecules in order to detect them.

Ionisation detection processes are state selective. In a resonantly-enhanced multiphoton ionisation (REMPI) process an ionisation laser excites a narrow band ($0.2\,\mathrm{cm}^{-1}$) of states, usually restricted to a single electronic state. The symmetry of the detected

state can also be inferred from the selection rules governing the ionisation pathway.

A more practical advantage of using ionisation detection is that experiments can be performed with a shorter duty cycle than trap-loss experiments. It takes 30 seconds (1/e time constant) for the trap population to reach equilibrium after the introduction of a loss mechanism like photoassociation. The factor limiting the speed of ionisation measurements is generally the time for untrapped molecules to leave the ionisation region before the next pulse arrives. This is typically several ms, though an experiment with a 150 Hz ionisation laser repetition rate has been reported [28].

3.2 Ionisation and Detection Systems

3.2.1 Ionisation Laser

The ionisation laser is a tuneable pulsed system which consists of a Q-switched Nd:YAG (neodymium-doped yttrium aluminium garnet, $Nd : Y_3Al_5O_{12}$) pumping two (β-Barium-Borate) nonlinear crystals in a Master-Oscillator Power-Oscillator (MOPO) configuration.

The Q-switched Nd:YAG provides short (10 ns) intense (500 mJ) pulses at a repetition rate of 10 Hz. The third harmonic of the Nd:YAG (354.7 nm) pumps a master oscillator which is continuously tuneable over the visible spectrum 430-700 nm. The master oscillator line-width is narrowed to 0.2 cm^{-1} with grating feedback. The output from the master oscillator is injected into a power oscillator which amplifies the pulses to 50 mJ retaining the line-width and tunability of the master oscillator, and the short pulse width of the Nd:YAG pump laser.

Light from the MOPO is delivered to the atoms by 15 m of high power multi-mode optical fibre (Oz Optics QMMJ-5HP-IRVIS-550/600-3AS-15.) This fibre has a large 550 μm core diameter to reduce the power density at the input tip. The large size also

helps to dissipate heat. A 1.1 mm air gap surrounds the cladding to reduce the effects of overheating on surrounding materials such as epoxy which normally binds fibres to their mounting. This configuration is specified to 3 W of power for continuous light sources. However we have observed damage to the fibre tip at much lower average powers (of order 10^{-3} W) when coupling 10 ns pulses (peak power 10^4 W).

The 50 mJ pulses from the MOPO are attenuated before coupling into the fibre. Pulse energies of up to 2 mJ have been transmitted before damaging the fibre. Above this threshold pulse to pulse power transmission becomes unstable and then the input fibre tip fails catastrophically as shown in Figure 3.1. The dark areas of damage shown in the picture are due to "hot spots" in the spatial mode of the MOPO laser output, and the lighter areas are the ablated material. Improving the spatial mode of the laser would increase the amount of power that can be transmitted, though standard techniques such as spatial filtering proved challenging at these high peak powers.
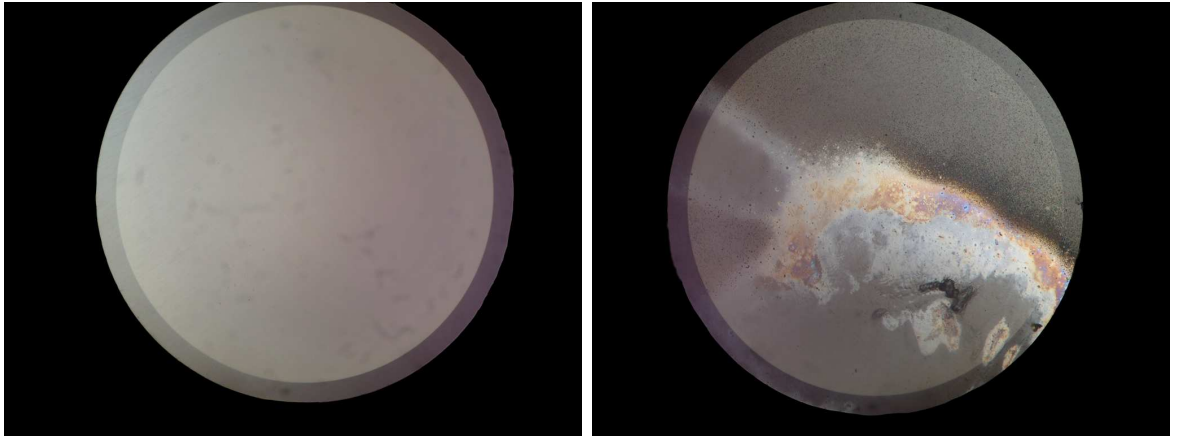
Fig. 3.1: left undamaged fibre tip; right fibre tip damaged by hot-spot in the spatial mode of the ionisation light. The pictures are taken through an optical microscope. The outer diameter of the fibre is 600 μm.

After transmission through the fibre the ionisation light is focussed onto the trapped atoms. The focal spot is limited by the 550 μm optical-fibre core, and by the 203 mm distance between the UHV chamber window and the trapped atoms. The tightest focal spot was achieved without collimation of the fibre output, imaging the fibre tip onto

the MOT with a single lens system. The 2σ waist is 1.2 mm which is greater than the 0.78 mm 2σ diameter of the MOT.
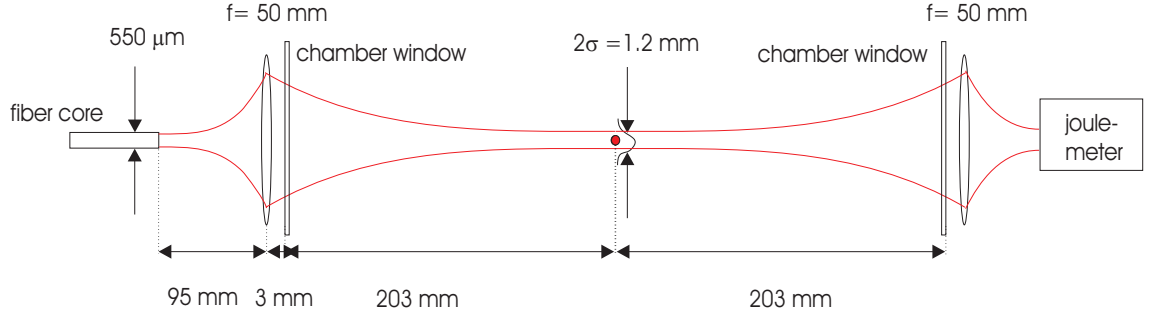
Fig. 3.2: Imaging of ionisation light onto the MOT

After passing through the chamber the light is focussed onto a piezo electric joulemeter which records pulse to pulse energies *in situ*. The joulemeter output goes through a gated integrator to integrate the peak power, and the pulse energy variation is recorded simultaneously with the ion data.

3.2.2 Channeltron

A channeltron electron multiplier (CEM), (Dr. Sjuts Optotechnik model KBL15RS) is used for ion detection. Positive ions are accelerated into the collection funnel of the CEM which is held at a negative potential. When ions contact the CEM entrance an electron shower is generated. The potential on the body of the CEM accelerates these electrons and further electron emission amplifies the electron cloud. The electron cloud leaves the CEM at a potential of 100 V and is accelerated through free space onto the collection anode. The signal is collected from the anode which is electrically isolated from the CEM body.

The CEM has a gain of 10^8, a response time of 26 ns and a pulse width of 10 ns. The collection cone is held at -2400 V relative to the rest of the chamber and the anode fixed at -120 V with a 10 MΩ resistor in parallel with the 200 MΩ resistance of the

CEM.

Employing a variable external resistor allows the anode voltage to be tuned; however the ion detection electronics were very sensitive to noise in external components before the pre-amplification stage. As a result the anode potential was fixed by soldering the 10 MΩ external resistor directly to the UHV feed-through and care was taken in the shielding of the external resistor and the pre-amplifier. After passing through a pulse discriminator and pre-amplifier, the signal from the CEM undergoes further processing in a boxcar module. A signal from the preamplifier averaged over 32 samples is shown later in Figure 3.7.
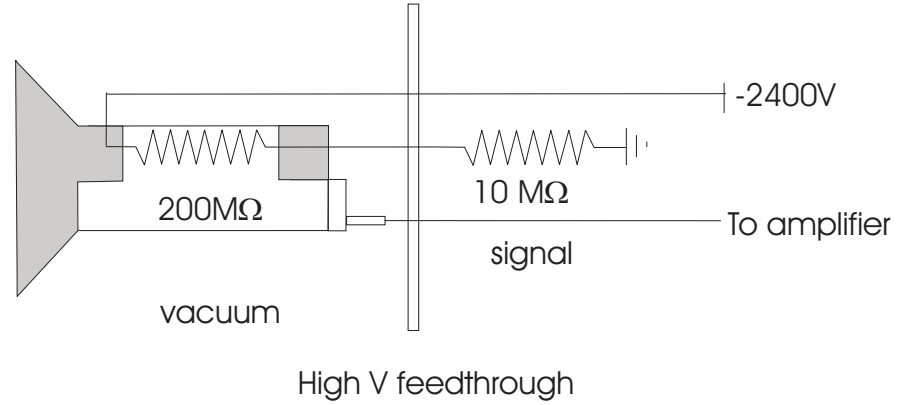
Fig. 3.3: Channeltron Electrical Configuration.

3.2.3   Ion Collection Geometry

Ions are created in the MOT at the centre of the vacuum chamber, the collection cone of the CEM is held at a negative potential with respect to the metal chamber, accelerating positive ions into the collection cone where they are amplified and detected.

There are no additional electrostatic components inside the UHV chamber. In this geometry the ion collection fields are generated by the potential difference between the CEM and the stainless steel walls of the grounded vacuum chamber. The chamber

layout is shown in Figures 2.7 and 2.8.

Gauss' law relates the electric displacement field $\overrightarrow{D}$ to the space charge density ρ, $\nabla \cdot \overrightarrow{D} = \rho$. In free space $\overrightarrow{D} = \varepsilon_0 \overrightarrow{E}$ and $\rho = 0$. From the definition of the electric scalar potential $\overrightarrow{E} = -\nabla V$ in free space Gauss' equation reduces to the Laplace equation $\nabla^2 V = 0$.

The region between the MOT and the CEM is approximately cylindrically symmetric around the axis through the MOT and the CEM. As a result the electric potential V can be found everywhere by solving the Laplace equation numerically in the two-dimensional plane shown in Figure 3.4a. The Dirichlet boundary conditions are -2400 V on the CEM and 0 V on the chamber walls as shown in Figure 3.4b. The electric potential was solved using a finite-element numerical technique in the electrostatics application mode of the Matlab Partial Differential Equation Toolbox [29]. The resulting electric potential V is shown in Figure 3.4c.

At the position of the MOT, where spectroscopy is performed on the atoms and molecules the calculated electric potential V is -184.75 V, and the calculated electric field component in the direction of the CEM detector is E_z= -29 V/cm and in the orthogonal directions $E_x = E_y \approx 0$ V/cm.

3.3   Time of Flight Detection

Ions formed at the centre of the MOT at a potential of -185 V and an electric field magnitude of -2900 V/m travel 104 mm to the CEM detector held at -2400 V. The ions feel an acceleration $\vec{a}_{ion}$ given by:

$$\vec{a}_{ion}(\vec{x}) = q/m \ \vec{E}(\vec{x}) \tag{3.1}$$

where q is the ion's charge (+e for a singly ionised particle), m is its mass, and $\vec{x}$ its
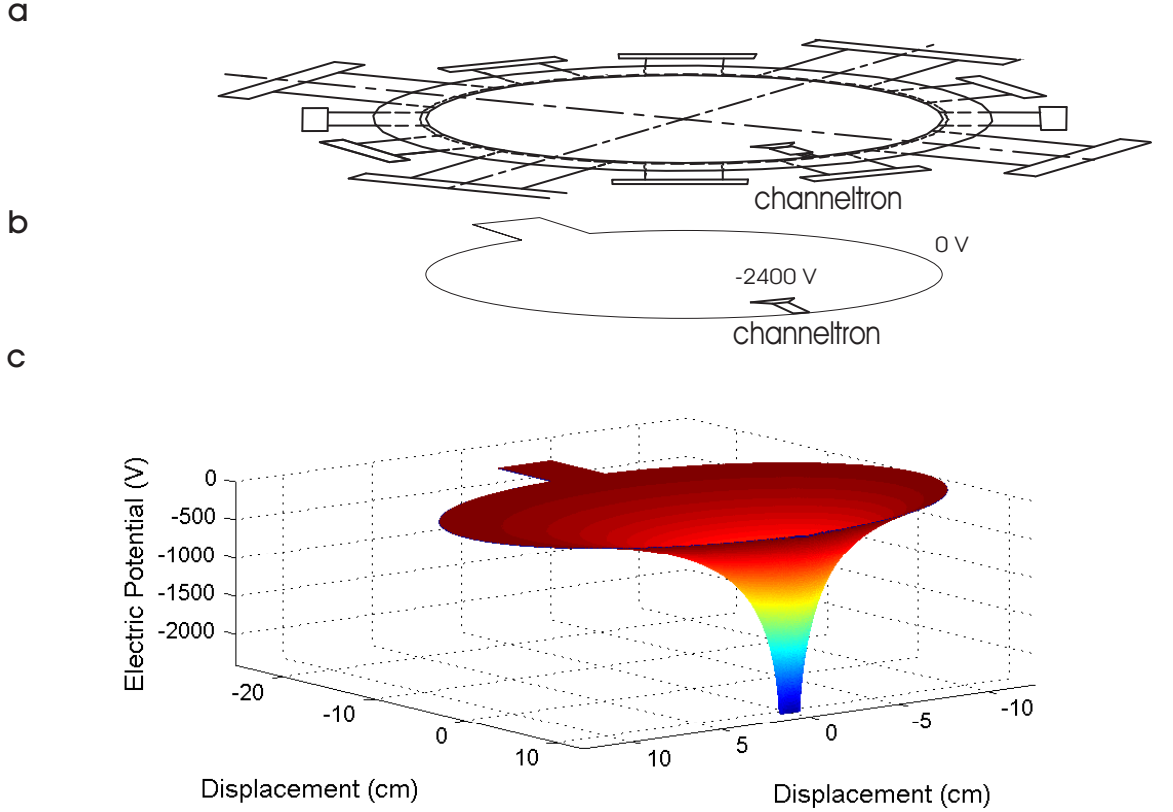
Fig. 3.4: **a.** Vacuum chamber and channeltron geometry **b.** Dirichlet boundary conditions for electric field simulation **c.** Electric potential inside the chamber.

position.

The one-dimensional potential between the MOT and the detector is shown in Figure 3.5. The acceleration as a function of position and the resulting time of flight (TOF) to the detector is calculated numerically using Equation 3.1. The calculated TOFs for atomic and molecular ions of both isotopes are listed in Table 3.1.

3.4 Time of Flight Resolution

The TOFs calculated above are for stationary ions formed at the centre of the MOT. There are a number of factors that broaden the arrival time of a given ensemble of ions,
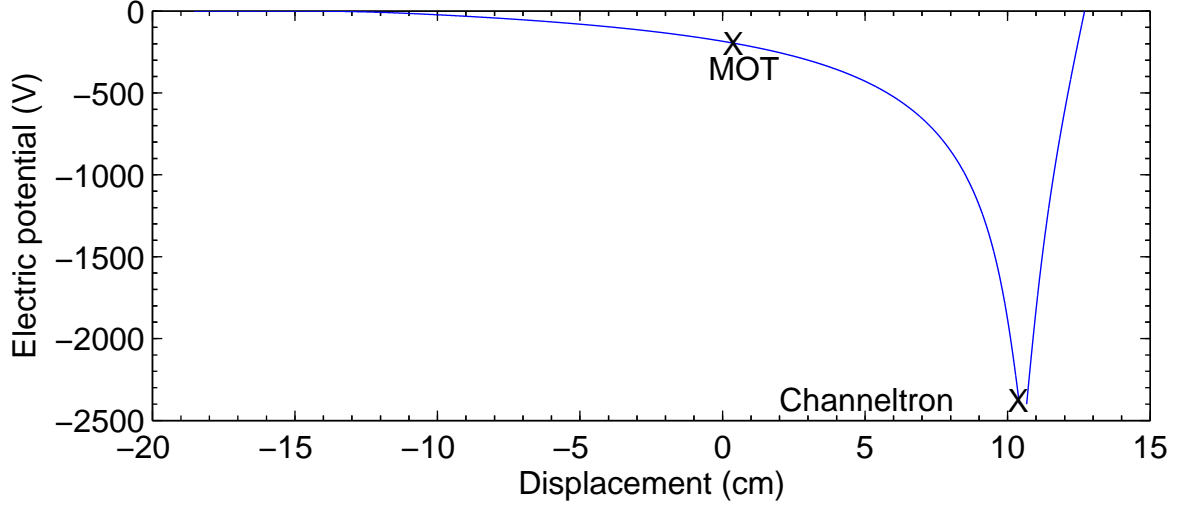
Fig. 3.5: Cross section of Electric Potential in the plane of the MOT and detector.

Table 3.1: Time of flight for Rb ions

ION	Charge	Mass(a.m.u.)	Time of flight (μs)
$^{85}Rb^+$	+e	85	9.31
$^{87}Rb^+$	+e	87	9.42
$^{85}Rb_2^+$	+e	170	13.17
$^{87}Rb_2^+$	+e	174	13.33

reducing the resolution of the TOF discrimination. These include interactions between ions, finite sample temperature, finite ionisation volume effects and the response time of the detector and electronics.

Typically $< 10^3$ ions/pulse are formed in a volume of $\sim$1 mm^3, corresponding to a nearest-neighbour ion spacing of $>$100 μm. The strength of the electric field from the nearest-neighbour (e/4$\pi\epsilon_0 r^2 \sim$-0.1 V/m) is more than 5 orders of magnitude lower than the interaction with the average external field (-24000 V/m). Under these experimental conditions the effects of ion-ion interaction are negligible compared to other broadening mechanisms.

The calculated effects of finite ionisation volume and finite sample temperature were

investigated numerically using the electric field calculations from Figure 3.4. The geometry is cylindrically symmetric around the z-axis (which passes through the MOT and CEM); so only a single radial direction needs to be considered.

The effects of the finite MOT temperature are also negligible. For an atomic ensemble laser cooled to 120 μK the atoms have an average velocity of 10 cm/s in each direction. This corresponds to a broadening of $\pm 6 \times 10^{-5}$ μs on the 9.4 μs TOF. This TOF broadening is comparable to the ion-ion interactions but negligible compared to the 100 ns instrument resolution, which is discussed below. The effect of heating caused by the ionisation process is neglected since the recoil velocity arising from the absorption of an ionisation photon (0.67-1.17 cm/s) is comparable to the recoil momentum from absorbing a photon from the trapping light (0.60 cm/s) which limits the MOT temperature.

The effect of the finite size of the ionisation region on the TOF of atomic ions is shown in Figure 3.6. Atoms in the ionisation region have a Gaussian spatial distribution with a 1 mm (1/e^2) radius; so atoms are initially 103$\pm$1.0 mm from the detector. The effect of the finite MOT size on ^{85}Rb ion TOFs is to smear the arrival times to $\approx$ 9.3$\pm$0.1 μs, which is comparable to the broadening due to the instrument resolution of 0.1 μs, and observable in experimental TOF data. The TOF for ^{85}Rb molecules is $\approx$ 13.17$\pm$0.2 μs and the ^{87}Rb TOFs scale with a factor of $\sqrt{87/85}$.

Comparing the broadening mechanisms to the TOF data in Table 3.1, atomic ions are clearly resolved from molecular ions for both isotopes. Experimental discrimination of atomic ^{87}Rb$^+$ and ^{85}Rb$^+$ ions (separated by 0.11 μs) is in principle on the edge of the resolution of this system, though in practice the two isotopes are never trapped simultaneously.

An experimental TOF spectrum for ^{85}Rb atomic and molecular ions is shown in Figure 3.7 with the calculated values shown for comparison. The instrumental timing resolution can be inferred from the width of the peak at 0 delay, which is from scattered
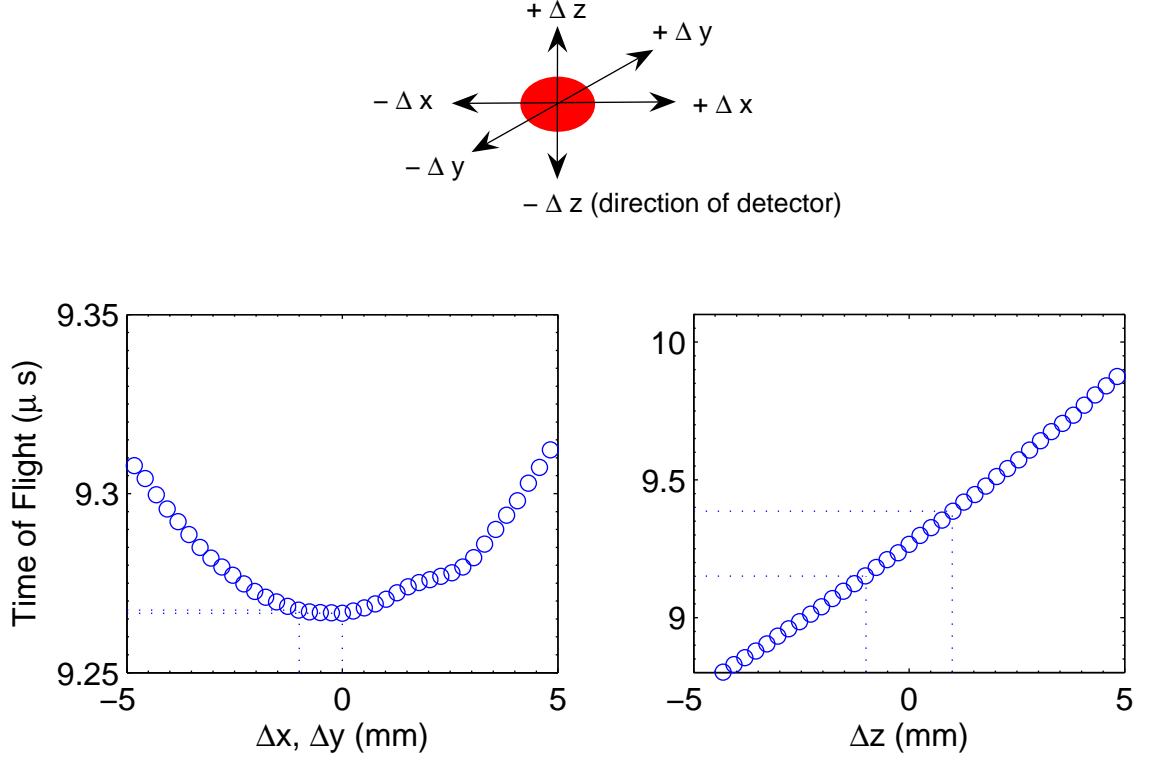
Fig. 3.6: Calculated TOF for atoms displaced from the centre of the MOT. Due to the cylindrical symmetry of the applied voltages, atoms see the same electric field in the x and y plane. The time of flight for atoms displaced in the x and y directions is relatively unchanged compared to atoms displaced in the direction of the detector (z direction). The structure around Δx and Δy=1 is due to the mesh used for the numerical potential calculations.

photons from the 10 ns ionisation pulse. The FWHM TOF broadening due to the detection instrumentation is 100 ns.

The atomic ion peak has a FWHM of 200 ns, which is consistent with the convolution of broadening from the finite volume effect and the detection electronics. The molecular peak FWHM is 300 ns, which is also consistent with broadening from the finite volume effect and detection electronics. The effects of finite velocity do not become appreciable compared with the other broadening effects until the sample temperature is 100 K, which places a (very high) upper limit on the molecule temperature which is expected to be close to the atomic temperature of 100 μK [30].
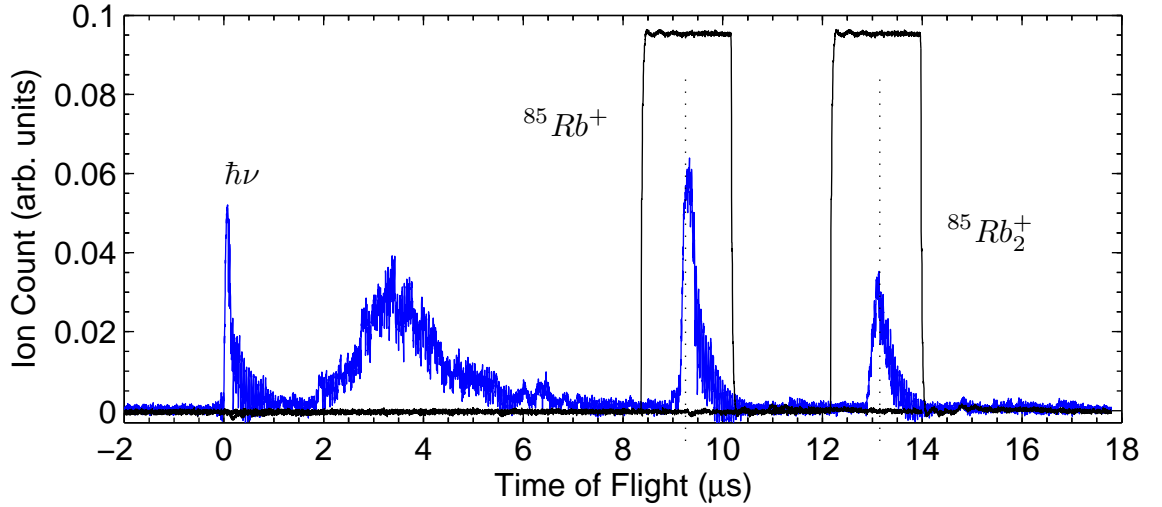
Fig. 3.7: Time-of-flight spectrum for ^{85}Rb captured on an oscilloscope. Dotted lines show calculated times of flight and the black bins show the integration region for counting atomic and molecular ions. The ionisation laser was tuned to 16,597 cm-1. The broad ion signal around 4 μs is an artifact, present when the ionising light was aligned off-axis of the chamber windows, resulting in scattered photons in the UHV environment.

3.5   Detection Electronics

A fast (10^7 Hz) sampling rate is required in order to continuously record TOF spectra with features 1 μs wide. The National Instruments digital acquisition cards used to collect experimental data do not have fast enough sample rates to record TOF spectra directly; so an additional boxcar integration stage is added before the digital data collection.

The output from the pulse discriminator and pre-amplifier goes to two Stanford Research Systems gated integrators and boxcar-averagers (model SRS-250). The integrators are triggered from the Q-switch output of the Nd:YAG which pumps the ionising MOPO. The integration regions are shown in Figure 3.7; they are 2 μs wide, one is centred on the atomic peak at 9 μs delay and the other at the molecular signal with 13 μs delay.

The boxcar output is an analogue voltage which is updated at the repetition rate of

the ionising laser, i.e. 10 Hz. This is slow enough to be easily recorded by the National Instruments data input cards at low sampling rates. The output voltage of the boxcar is the integrated input voltage over the gated region. A schematic of the ion detection electronics is shown in Figure 3.8.
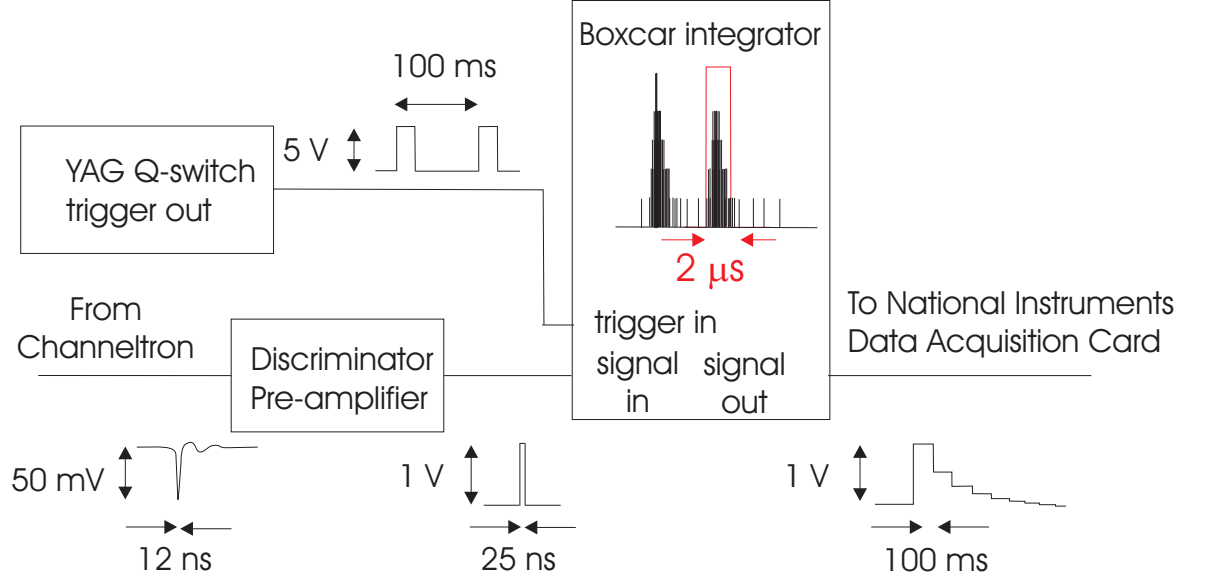
Fig. 3.8: Ion detection electronics.

3.6   Calibration of Ion Signal

To calibrate the ion detection electronics a large number of atomic ion samples were collected from a ^{85}Rb MOT while the ionising laser frequency was scanned over atomic resonances. The boxcar gate was placed over the atomic ion window with a delay of 9 μs and a width of 2 μs and ^{85}Rb atomic ions were detected. The energy of the ionising light was reduced to below 100 μJ, where there was on average less than one ion detection event per pulse. The boxcar gain was set to 40$\times$ (signal sensitivity of 1V/25 mV) to fill a reasonable range of the 12-bit digital acquisition card, without saturating the boxcar. This optimises the measurement resolution by limiting the digitisation of the data.

The output of the boxcar was recorded for 17,000 samples, while the ionising laser was scanned 479-502 nm. The voltage output from the boxcar is digitised into 5 mV bins as it is recorded by the 12-bit, ± 10 V range, digital acquisition card ($20 \ V/2^{12}$). A histogram of the recorded voltage counts is shown in Figure 3.9.

From the histogram, peaks corresponding to 0 up to 7 coincident ions counts are readily identified. The baseline has a small offset, centred around 8×10^{-4} V with a standard deviation of 0.01 V. The counts corresponding to a single ion are centred around 0.618 V, with a standard deviation of 0.048 V. All of the resolved peaks follow the single ion peak calibration of 0.618 ± 0.048 V/ion, though the higher coincident ion peaks are significantly broader than the single ion peak. In practice the gain of the boxcar is regularly adjusted so the signal fills the ± 10 V range of the data acquisition to maximise resolution. The boxcar gain has a linear response; so the calibration is adjusted by the gain factor when the boxcar gain settings are modified.
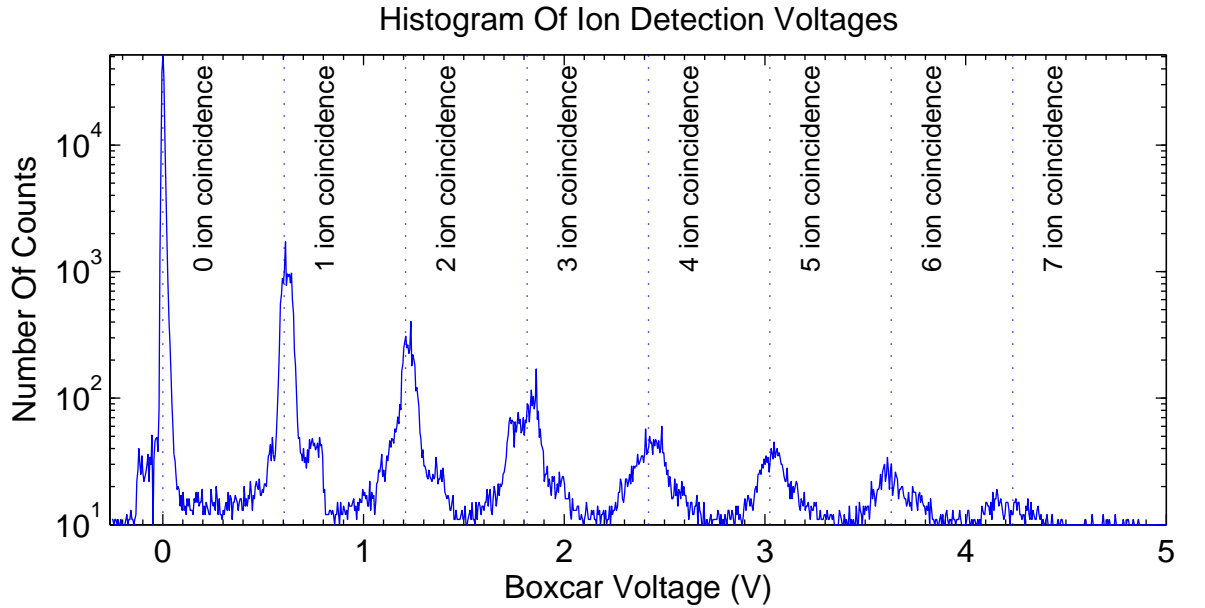
Fig. 3.9: Histogram of the boxcar voltage output for 17,000 ion detection samples. Peaks corresponding to 0 up to 7 coincident ions can be clearly identified, resulting in a gain of 0.681 ± 0.048 V/ion.

Chapter 4

Rydberg Atoms

"Once the Bohr theory was formulated it was apparent that Rydberg atoms should have bizarre properties."

— Thomas F. Gallagher, *Rydberg atoms*

4.1 Introduction

The availability of laser cooled atoms has re-invigorated the study of Rydberg systems; atoms excited to high principal quantum numbers n. Combined with the sensitive ion detection systems described in the previous chapter, and intense lasers tuneable over the whole optical spectrum, these systems and their interaction with their environment can be studied in unprecedented detail.

Rydberg atoms are particularly sensitive to their local environment, due to their close energy level spacing and large valence electron orbits $r \propto n^2$. One example is their sensitivity to ambient blackbody radiation, which redistributes Rydberg atoms between neighbouring energy states. The effect of blackbody radiation is readily observed when measuring the lifetime of Rydberg systems [31].

In the experiment reported here precise measurements of Rydberg energy level dynamics are taken over a wide range of energy levels. A model of excited state population dynamics following initial uniform excitation to a single Rydberg level is developed. This model builds on existing models for spontaneous decay rates and coupling between Rydberg atoms and ambient black-body radiation. Comparison of the experimental results clearly shows the range of validity of two existing theoretical models governing interactions with blackbody radiation, both of which are currently used in the literature [32] [33]. The interaction with black body radiation is an important source of decoherence in many quantum information schemes [34].

Additional measurements on atomic systems were taken to help characterise the experimental apparatus for later investigations into cold molecules. The ionisation detection system described in the previous chapter involves the application of relatively intense radiation fields required for ionisation, and electric fields for ion collection. Rydberg systems are ideal for probing the effects of external fields and collisions in the MOT, since they are very sensitive to their environment and relatively well understood. Deviations of measured energy levels and lifetimes from published values is studied, and the strength, shifting, broadening and splitting of levels is examined as a function of applied fields.

The final motivation for the atomic ionisation measurements presented here is that strong atomic ionisation processes interfere with measurements of much weaker molecular ion signals. Ionised atoms cause local space charge effects which can perturb molecular properties and TOF ionisation measurements. Atoms excited to Rydberg states can also have sufficiently long lifetimes ($> 1 \mu$s) that they interfere with TOF discrimination of molecules. These issues are exacerbated by the use of intense broadband optical probes, as are required for measuring short time dynamics, one of the future goals of this project.

4.2 Previous Studies of Rydberg Atoms

With the advent of the tuneable dye laser, ensembles of Rydberg atoms could be created in a single state and studied. Lee *et. al.* [35] employed a dye laser with a 250 kHz linewidth to measure the ^{85}Rb I ns energy levels using a two-photon Doppler-free technique in a vapour cell. High resolution measurements of the ns, np and nd Rydberg series have been made made in ^{85}Rb thermal vapour cells at high pressures and densities using narrow band dye lasers and Doppler-free spectroscopic techniques claiming 0.001 cm^{-1} resolution [36].

With the production of cold Rydberg atoms [37] there has been renewed interest in low temperature Rydberg systems for applications such as studies of collective effects [38] and formation and recombination of ultracold Rydberg plasmas [39] and quantum computing [34].

Cold samples have also improved measurements of fundamental properties of Rydberg atoms such as high-resolution microwave spectroscopy of energy levels [40] and lifetime measurements [32] which are closely related to interactions with ambient radiation [33].

Rydberg lifetimes have been measured using laser-induced fluorescence measurements on thermal samples; however atom transit times and collisional limitations have restricted such measurements to states between n=9 and n=18 [41] [42] [43].

Trapped cold atoms are ideal for measuring lifetimes, eliminating the problems of transit times and allowing measurements at low densities thereby reducing the effects of collisions and super-radiance. Excitation and ionisation can be performed efficiently as the compact trap size allows high fields to be focussed on the sample.

In 2002 lifetimes for ^{85}Rb ns, np and nd states where n=31-45 were measured in a MOT using state-selective field ionisation [33]. Field ionisation measurements have high resolution of energies enabling the study of closely spaced high n states to be resolved. In 2006 lifetimes and absorption cross-sections were measured for 10.6 μm

radiation for the nd states of Rb where n= 16-20 [44]. The use of optical ionisation provides less state selectivity in the detection process than field ionisation techniques. However photo-ionisation can be performed over a range of states, including low n states which require high, experimentally challenging, electric fields to field-ionise.

The work presented here builds extends on previous precision studies of Rb lifetimes in cold atoms, extending the measurements over a much wider energy range. Both lifetimes and interactions are measured at high principal quantum numbers where there is very little core-valence electron interaction, and down to the ground state where these interactions are significant, and quantum defect approximations break down.

4.3   Quantum Defect Theory

Rydberg atoms have a highly excited electron which is far from the inner core of the atom. As this outer electron is far from the core, thus feeling only a central coulombic force, it is well described by a hydrogenic model. A slight modification from a purely hydrogenic model introduces so called quantum defects to take into account effects from the atomic core. The hydrogenic wavefunctions and resulting energies and lifetimes of allowed Rydberg states are discussed below in sections 4.3.1, 4.3.3 and 4.3.4 respectively.

4.3.1   Rydberg Atomic Wavefunctions

Alkali atoms have a single valence electron outside of an ionic electronic core. In highly excited states the valence electron is mostly found outside of the ionic core. In an atom with atomic number Z the valence electron sees a nuclear core of charge $+Ze$ shielded by the electronic core of charge $-(Z-1)e$ and is well described by the Schrödinger equation for hydrogen.

$$\left(-\frac{\hbar^2}{2m}\nabla^2 - \frac{1}{4\pi\varepsilon_0 r} \right) \psi = E\,\psi \tag{4.1}$$

Expressed in spherical co-ordinates this equation can be separated into angular and radial variables. The angular equation is identical to a hydrogen atom, giving spherical harmonic eigenfunctions $Y_{lm}(\theta, \phi)$.

The radial equation for alkali atoms is also identical to the hydrogen radial equation but the potential $V(r)$ now has a modified form. The valence electron spends most of its time outside the inner electron shell, where it feels a hydrogenic potential, but when it penetrates the inner shell it feels a reduced central potential. In terms of the wavefunction, outside the shell the potential is identical to hydrogen; so the form of the wavefunction is identical. Inside the inner shell, the electron feels a lower potential corresponding to a higher kinetic energy ($\nabla^2\psi$). The increased curvature in the inner shell region imposes a different boundary condition outside of the shell, resulting in a phase shift δ_{nlj} in the general form of the hydrogenic wavefunction. Explicitly,

$$\psi_{rydberg}(n, l, m) = Y_{lm}(\theta, \psi)[f(E, l, r)cos(\pi\delta_{nlj}) - g(E, l, r)sin(\pi\delta_{nlj})]. \tag{4.2}$$

where E is the energy of the atom, $Y_{lm}(\theta, \psi)$ are the spherical harmonics and $f(E, l, r)$ and $g(E, l, r)$ are oscillatory functions 90 degrees out of phase, known respectively as the regular and irregular Coulomb functions, which can be calculated numerically [45] [46].

The phase shift δ_{nlj}, known as a quantum defect, exhibits a strong n and l dependence and a weaker j dependence. The quantum defect is simply a measure of the deviation of the (nucleus and Z-1 core electrons) from the purely hydrogenic Z=1 system. It is largest for states where the electron orbit has large overlap with the core, i.e. small n,l and j. The quantum defect has the empirical form:

$$\delta_{nlj} = \delta_0 + \frac{\delta_2}{(n - \delta_0)^2} + \frac{\delta_4}{(n - \delta_0)^4} + \frac{\delta_6}{(n - \delta_0)^6} \dots \tag{4.3}$$

4.3.2 Quantum Defects for Rb

The quantum defects of Equation 4.3 for ^{85}Rb have been determined from high resolution measurements of the energy levels [36]. The values shown in Table 4.1 are extracted from higher resolution energy spectra than those presented here, and are consistent with all of our measurements. These values are used to determine the effective principal quantum number n^*, discussed below, for all further analysis in this chapter.

Table 4.1: Published ^{85}Rb quantum defects for ns, np, nd and nf states [36].

Series	δ_0	δ_2	δ_4	δ_6	δ_8
^{85}Rb ns$_{1/2}$	3.131902(2)	0.204(8)	-1.8		
^{85}Rb np$_{1/2}$	2.65456	0.388	-7.904	116.437	-405.907
^{85}Rb np$_{3/2}$	2.64145	0.33	0.97495	146001	-447265
^{85}Rb nd$_{3/2,5/2}$	1.347157	-0.59553	-1.50517	-2.4206	19.736
^{85}Rb nf$_{5/2,7/2}$	0.016312	-0.064007	-0.36005	3.2390	

4.3.3 Rydberg Atom Energies

Equation 4.1 is the familiar Schrödinger equation for hydrogen which can be solved exactly. The eigenvalues give the energies for the allowed bound states with principal quantum number:

$$E(n) = -R_H \, \frac{1}{n^2} \tag{4.4}$$

where R_H can be expressed in terms of the Rydberg constant R_∞

$$R_H = -\left(\frac{M}{m_e + M}\right) R_\infty = -\left(\frac{M}{m_e + M}\right)\left(\frac{m_e c \alpha^2}{2h}\right) \qquad (4.5)$$

where α is the fine structure constant, h is Planck's constant, M is the atomic mass, and m_e is the electron mass. The negative energies are measured relative to the ionisation potential, i.e. $\lim_{n\to\infty} E(n){=}0$.

In the quantum defect model the effective principal quantum number $n^* = n - \delta_{nlj}$ is no longer an integer; however the Schrödinger equation can still be solved analytically; the allowed energies are:

$$E = -R_H \, \frac{1}{(n - \delta_{nlj})^2} = -R_H \, \frac{1}{n^{*2}} \qquad (4.6)$$

4.3.4 Rydberg Radiative Lifetimes

The radiative lifetime for a Rydberg atom in state $|n^*, l\rangle$ can be written in the usual way as a sum of spontaneous decay rates to all the energetically lower lying states $|n^{*\prime}, l'\rangle$.

$$\tau(n^*, l) = \left(\sum_{n^*l, n^{*\prime}l'} \frac{4e^2 \omega_{n^*l, b'l'}^3}{3\hbar c^3} \, \frac{l_{max}}{2l + 1} \, |\langle n^{*\prime}l'|r|n^*l\rangle|^2 \right)^{-1} \qquad (4.7)$$

The dipole matrix elements and subsequent decay times can be accurately calculated. When $n > l$, as is the case for all of the states considered in this thesis, the radiative decay time exhibits an approximately n^3 dependence.

Gounard calculated radiative lifetimes in the Coulomb approximation and expressed the lifetimes τ of a series of states n with the general expression [47]:

$$\tau_{radiative}(n) = \tau'(n^*)^\gamma \qquad (4.8)$$

where the τ' and γ have been calculated for the ^{85}Rb ns, np, nd and nf series [47] [48] and measured for the ns, np and nf series [33].

4.3.5 Blackbody Population Transfer Rate

The lifetime of Rydberg states at finite temperatures τ_T is not determined purely by the spontaneous decay rates of Equation 4.8. Atoms are also perturbed by the ambient blackbody radiation, with the effects becoming stronger at higher n where energy intervals between states are smaller. The blackbody radiation is in thermal equilibrium with the surrounds at room temperature (300 K), not with the sample of trapped atoms at 119 μK. The effect of blackbody radiation at 300 K has been calculated with coulombic models [31] [48]. Farley [48] gives the following form for the effects of blackbody radiation, which he notes has increasing accuracy at higher n^*, and is valid for $n^* >$ 12.8:

$$\tau_{bb}(n^*) = \left(\frac{4}{3} \frac{e^2}{\hbar c} \frac{k_B T}{\hbar} \frac{1}{n^{*2}.} \right)^{-1}_{.} \tag{4.9}$$

Theodosiou used a coulombic model modified at short range to include spin orbit and core polarisability [49]. He calculated ^{85}Rb lifetimes for n=4 up to n=18 at 0 K and 350 K. Bagnato *et al.* made a polynomial interpolation of those results to give the nd lifetimes at 300 K in the form [32]:

$$\tau_{bb}(n^*) = 294.242 + 0.096(n^*)^{3.867} \tag{4.10}$$

where τ is in ns.

The rates of spontaneous decay and blackbody population transfer for T=300 K are shown explicitly for Rb states up to n^*=40 in Figure 4.1. The inverse of the purely blackbody decay rates of Farley (Equation 4.9) and Theodosiou (Equation 4.10) are
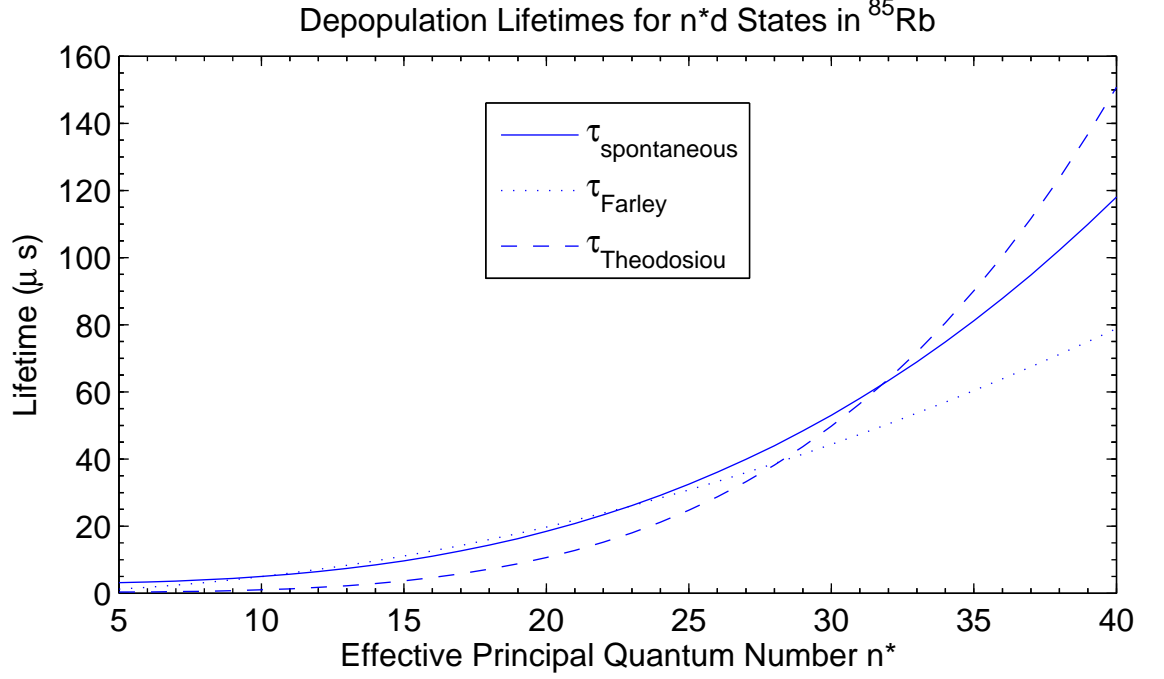
Fig. 4.1: Stimulated blackbody rates as calculated by Farley [48] and Theodosiou [49] and spontaneous decay rates as a function of effective principal quantum number.

shown along with the spontaneous lifetime from Equation 4.8 for comparison. The blackbody excitation rate of both models is of the same order as the spontaneous decay rate. For small n^* the Farley model predicts lower rates(longer lifetimes). At $n^* = 28$ the two models agree but at higher n^* the models diverge rapidly with the Theodosiou model predicting much lower rates (longer lifetimes).

4.3.6 Dipole Matrix Elements

The dipole matrix elements govern the strength of interaction between states and therefore atomic properties such as lifetimes and transition rates. The dipole matrix elements between two alkali atom states $\langle n'l'|er|nl \rangle$ can be calculated after solving the wavefunctions numerically from Equation 4.1.

It is possible to estimate the strength of matrix elements between states with the same

principal quantum number $\langle nl'|er|nl \rangle$ by consideration of their quantum defects. Since δ is the phase shift relative to the hydrogenic wavefunction, $\Delta = \delta - \delta'$ is the phase difference of the two wavefunctions. Two states with an integer Δ are in phase and have a large wavefunction overlap, and a large dipole matrix-element. Conversely two states with a half-integer Δ are out of phase and have poor wavefunction overlap and a small dipole matrix element. From Table 4.1 above, $\Delta_{ps} = \delta_{np}\text{-}\delta_{ns}$=0.48, so that the ns and np states are almost exactly out of phase and the dipole matrix element connecting the states is small. A dramatic consequence of this is the long lifetimes of np states which do not readily decay into the 5s ground state.

An approximate analytical expression for the hydrogen radial dipole matrix-elements in atomic units is [50]:

$$\langle n'|er|n \rangle \approx 0.4108\big(-2E_{n'} \big)^{3/4} \big(-2E_n \big)^{3/4} \omega^{-5/3} \qquad (4.11)$$

where $E_n = -1/2n^2$ is the binding energy of the state $|n\rangle$, and $\omega = |E_n - E_{n'}|/\hbar$ is the transition frequency. The dipole matrix-elements are normalised to the n^{-3} density of states, and have $\omega^{-5/3}$ frequency dependence, favouring transitions to nearby levels with low transition frequencies.

Alkali atom matrix elements are nearly hydrogenic when the quantum defect is small. All of the dipole matrix elements for the ns, np, nd and nf states have been calculated using quantum defects relative to the hydrogenic elements for Rb [50].

4.4 Energy Level Measurements

A resonantly-enhanced-multi-photon-ionisation (REMPI) spectrum was recorded in a ^{85}Rb MOT, the process is shown in Figure 4.2. In this case the probe laser is also the ionisation laser. Atoms are initially cooled in the MOT, cycling between 5s$\leftrightarrow$5p$_{3/2}$

levels. When the PI frequency ν_{probe} is resonant with an intermediate transition, the atoms can undergo resonantly-enhanced-two-photon-ionisation (RE2PI) from the $5p_{3/2}$ and are detected by the CEM. A signal arising from RE3PI of atoms initially in the 5s state is also observed. The probe laser frequency was scanned below the Rb I one-photon ionisation limit and a spectrum of detected ions recorded.
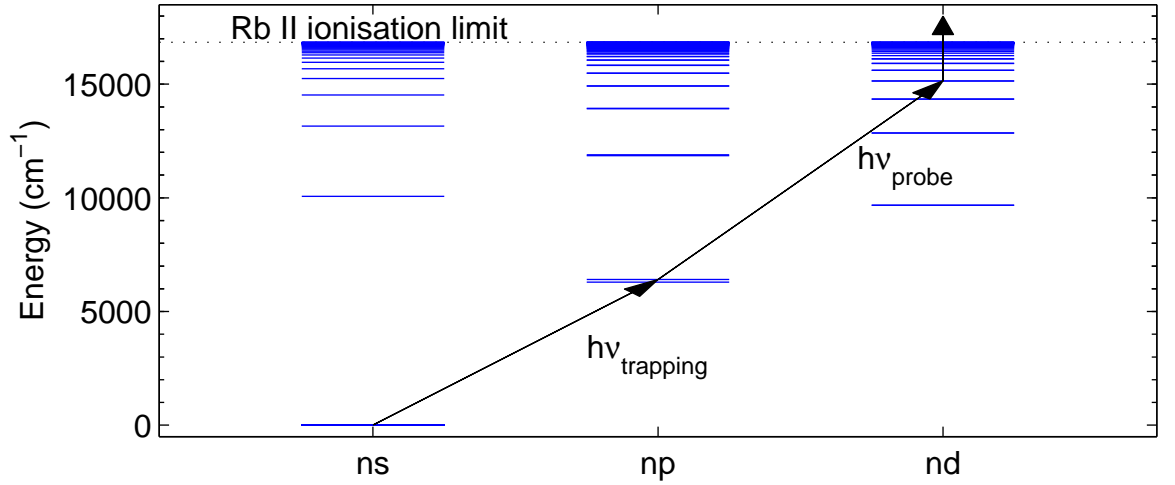
Fig. 4.2: Atomic level structure of Rb showing the trapping and cooling transition and the multi-photon ionisation spectroscopy scheme used in this experiment.

The probe laser used in this experiment is the pulsed MOPO described in Section 3.2.1. It is able to scan over large wavelength ranges mode-hop free, and with constant power output compared to dye laser technology. However it has a broad linewidth of 6 GHz (0.2 cm^{-1}), compared to the natural linewidth of the trapping transition (10 MHz), Doppler broadening in the sample (400 kHz) and the continuous wave (CW) linewidths of 1 MHz achieved for the trapping and photoassociation laser described later.

The MOT contained 10^6 atoms, at a density of 5×10^9 atoms/cm^3. The probe average-power was maintained at 100 mW (10 mJ pulse energy), where there is no line-broadening and the transitions are unsaturated as discussed later in Section 4.4.2. No systematic effects of line-broadening were seen in the data, which would be detected as increasing linewidths for transitions to higher n states. Both the atom number and

probe power were monitored *in situ.* The atom number fluctuated by less than 5% and the probe power by less than 20% over the entire scan. Peak heights should provide a measure of the relative transition strengths of the two-step RE2PI process, over a large range of n.

The boxcar integrator window was centred 9 μs after the ionisation pulse arrival, which corresponds to the time of flight of the atomic ions, with a width of 1 μs. The recorded spectra are shown in Figure 4.3, with the nd energy levels tabulated in Table 4.4.1. A high resolution scan was taken over the range 479-502.6 nm, with one pulse per 1×10^{-4} nm step-size, and a lower resolution scan taken from 475-632 nm with 1.5×10^{-3} nm step-size. Both spectra are shown in Figure 4.3 with the intermediate Rydberg states labelled. The higher resolution scan is plotted on a log wavelength plot so that energy levels can be identified.

4.4.1 Energy Level Data

The spectrum shown in Figure 4.3 is dominated by two series corresponding to transitions with the dipole-allowed intermediate transitions $5p_{3/2} \rightarrow n$d and $5p_{3/2} \rightarrow n$s. The measured level energies allow energy levels to be unambiguously assigned principal quantum numbers n and orbital angular momentum quantum numbers l up to n=40. The nd series is an order of magnitude stronger than the ns series which is consistent with the previous discussion in Section 4.3.6 of the dipole matrix elements which determine the strength of the two series.

As discussed in Section 4.2 the energy levels of Rb have been spectroscopically studied in detail. Figure 4.4 shows the Energy levels measured in this work from Table 4.4.1 graphed along with energy level measurements calculated from the quantum defects in Table 4.1. The absolute calibration of the energy levels is obtained from an internal calibration of the MOPO.

The residuals from Figure 4.4 show a clear n-dependence, with about a 1 cm^{-1} differnce

Fig. 4.3: Atomic ns and nd Rydberg series. The top spectrum is a broad lower resolution scan displayed on a linear wavelength scale. The middle and bottom spectra are progressively zoomed in sub-sections, displayed on logarithmic wavelength scales. Unresolved transitions close to the ionisation limit are indicated by overlapping transition labels. Asterisks denote prominent "Satellite" features.

61

State	λ (nm) in air	Energy (cm⁻¹) in vacuum	State	λ (nm) in air	Energy (cm⁻¹) in vacuum
6d	629.887	28688.0	25d	483.493	33493.6
7d	572.491	30279.2	26d	483.134	33509.0
8d	543.215	31220.3	27d	482.803	33523.1
9d	526.051	31820.8	28d	482.523	33535.2
10d	515.060	32226.3	29d	482.264	33546.3
11d	507.557	32513.3	30d	482.033	33556.2
12d	502.203	32723.3	31d	481.832	33564.9
13d	498.238	32881.7	32d	481.642	33573.0
14d	495.211	33004.3	33d	481.475	33580.3
15d	492.854	33100.9	34d	481.323	33586.8
16d	490.976	33178.5	35d	481.183	33592.9
17d	489.461	33241.5	36d	481.052	33598.5
18d	488.207	33293.9	37d	480.937	33603.5
19d	487.175	33337.3	38d	480.831	33608.0
20d	486.301	33374.2	39d	480.733	33612.3
21d	485.563	33405.4	40d	480.645	33616.1
22d	484.932	33432.2	41d	480.560	33619.8
23d	484.383	33455.6	42d	480.480	33623.2
24d	483.910	33475.8			

Table 4.2: Wavelengths and Energies for ^{85}Rb nd states from Figure 4.3. λ is the wavelength of $5p_{3/2} \rightarrow n$d transition in air and the energies are vacuum energies measured relative to the 5s ground state.

between the 6d and 42d energy level residuals. This observed difference in energy level shifts is consistent with the difference in Stark shift between these two levels (1.8 cm⁻¹) as discussed below.

4.4.2 Line Broadening and Shifts

In the spectra shown earlier there is some evidence of a systematic shifting of energy levels with n. In our MOT, a cold and relatively dilute atomic sample, the major sources of perturbation are the external electric field applied for ion extraction and the high peak power of the optical probe applied to ionise our sample. In the present geometry, all electric fields are generated by the potential of the CEM. The effect of
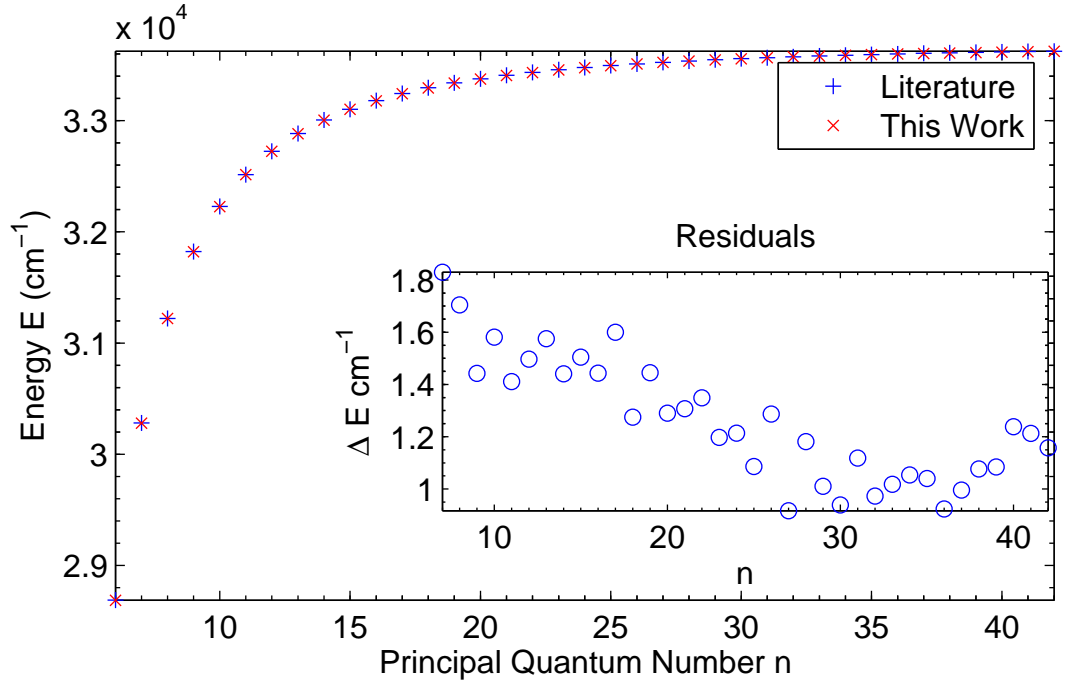
Fig. 4.4: Measured energy of Rydberg nd levels against values found in the literature. The magnitude of the residuals are consistent with a stark shift of the atomic levels due to the presence of the external electric field.

the external electric field on transitions could not be investigated experimentally using ionisation as a diagnostic, as when the potential on the CEM is reduced by 10 % there is no ion signal. The effects of the applied -2400 V potential can be calculated using experimentally measured polarisabilities for nd states [51]. The electric field at the centre of the MOT was calculated earlier to be -29 V/cm. The largest DC Stark-shift for the levels considered is for the $n=42$d, $j=5/2$ level which shifts less than 64 MHz/(V/cm)^2 corresponding to a shift of 1.8 cm^{-1} at the position of the MOT.

The effect of optical probe power on the energy level line-shape was investigated experimentally. Figures 4.5 shows a Gaussian profile fitted to the line-shape of the $5p_{3/2} \rightarrow 14$d transition probed at different optical powers. Figures 4.6 shows the linewidth, peak-height and line-center as a function of optical probe power. The peak-height rises linearly with probe power until the transition saturates at an average

power of 200 mW (20 mJ pulse energy). The line-width broadens at probe powers above 100 mW (10 mJ pulse energy). The line-centre of the transition shifts by less than 0.1 cm^{-1} when the optical probe average power is below 200 mW, which is less than the optical probe line-width of 0.2 cm^{-1}. For the atomic energy spectra presented earlier the average probe power was 100 mW (10 mJ/pulse), where the transitions are unsaturated and pulse broadening is small.
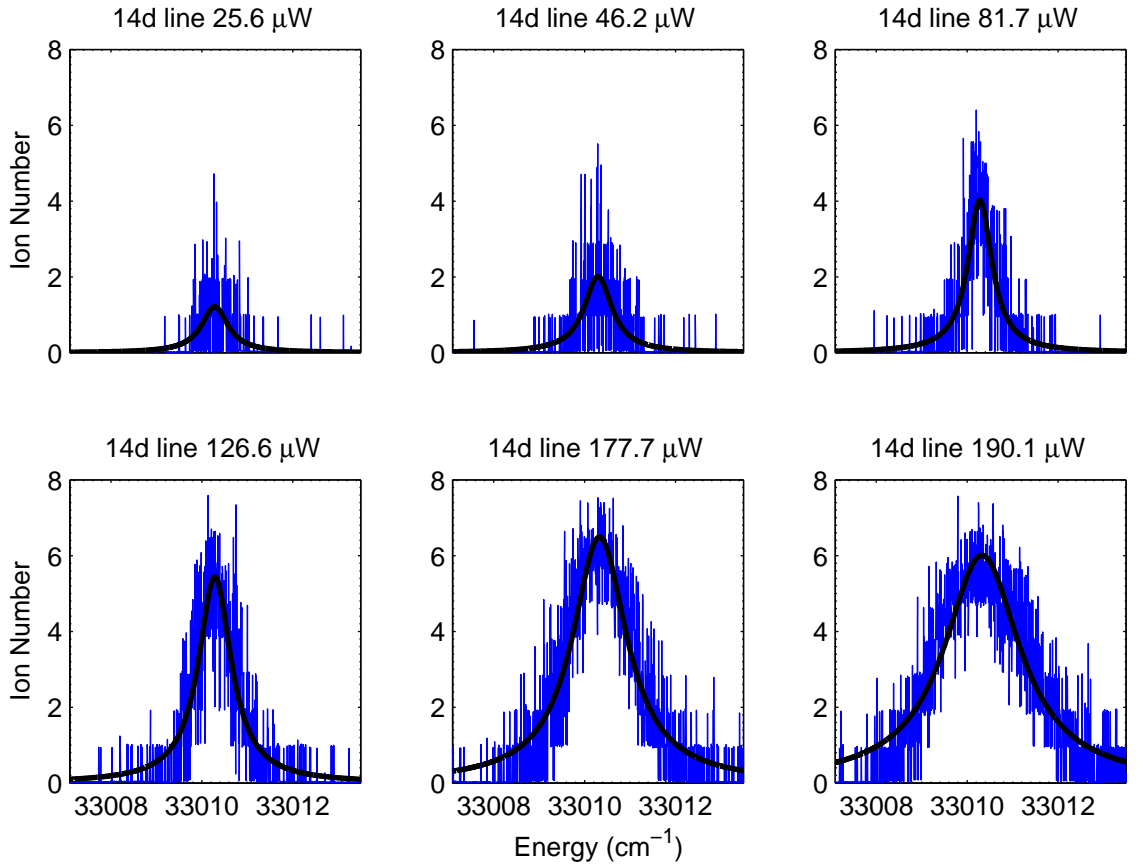
Fig. 4.5: 14d line-shape at different optical probe powers, with a Gaussian fitted to the line profile.
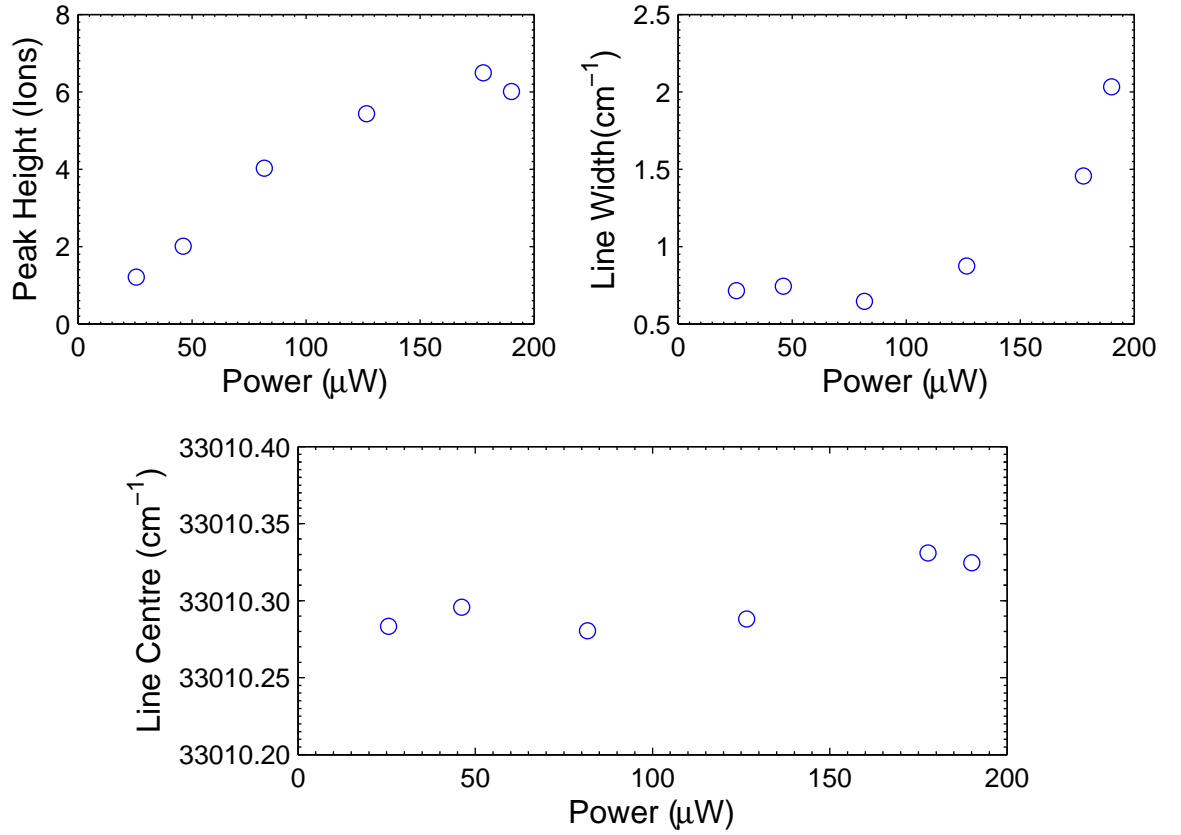
Fig. 4.6: $5p_{3/2} \rightarrow 14d$ transition strength, line-width (σ) and energy at different optical probe powers.

4.4.3 Line Shape

Figure 4.7 shows a high resolution scan of the $5p_{3/2} \rightarrow 6d$ transition. The $d_{3/2}$ and $d_{5/2}$ lines are clearly resolved, with fine structure splitting of 2.44 cm^{-1}. There is also evidence of additional splitting of the $d_{5/2}$ line, of the order of 0.2 cm^{-1}.

In Figure 4.3 every line in the nd series is accompanied by a broad satellite feature at higher energy. Some of the prominent satellites are identified with an asterisk. Figure 4.7 is a higher resolution spectra showing a broad satellite feature centred on 28,730 cm^{-1}. These "blue satellites" have the same energy spacing as the nd transitions, with the energy of the series converging with the 6d series until they start to overlap

near the 26d peak where the line spacing approaches the laser linewidth. This is strong evidence that the blue satellites are correlated with the nd peaks. The blue satellites are very broad with the 6d satellite having a one-sigma line width of 23 cm^{-1}, approximately 10 times broader than the 6d transition linewidths. The satellite of the broad 6d state is about half the height of the 6d transition, but contains an order of magnitude more ion counts when integrated over the entire peak.

The broad peaks can not be assigned to any of the dipole or quadrupole allowed transitions from either the 5s or $5p_{3/2}$ states present in the MOT. They are also not consistent with transitions to any higher angular momentum states, which converge to a purely hydrogenic energy distribution since the quantum defects become small for high l.

The lifetime of the blue satellites was measured, to aid their identification, and was found to be close to the neighbouring nd transition lifetime. Lifetimes of the ns transitions could not be measured for comparison as they overlap the broad peak. The strength of the blue satellite peaks is oscillatory with n, and does not correlate with the strength of the neighbouring $5p_{3/2} \rightarrow n$d transition.

The satellite features appear to be genuine atomic structure, present only at resonant frequencies when atoms are present. The most likely origin of the satellite peaks is the omnipresent 28 V/cm external electric field described in section 3.3. The dependence of the blue satellite structure on the external electric potential cannot be investigated in the current set-up, as when the external electric field is reduced no ions are detected. It is noted here that the satellite features are strongest at small principal quantum number, whereas the effects of external fields tend to increase with the principle quantum number. These features require further investigation particularly with respect to their dependance on the external electric field strength.
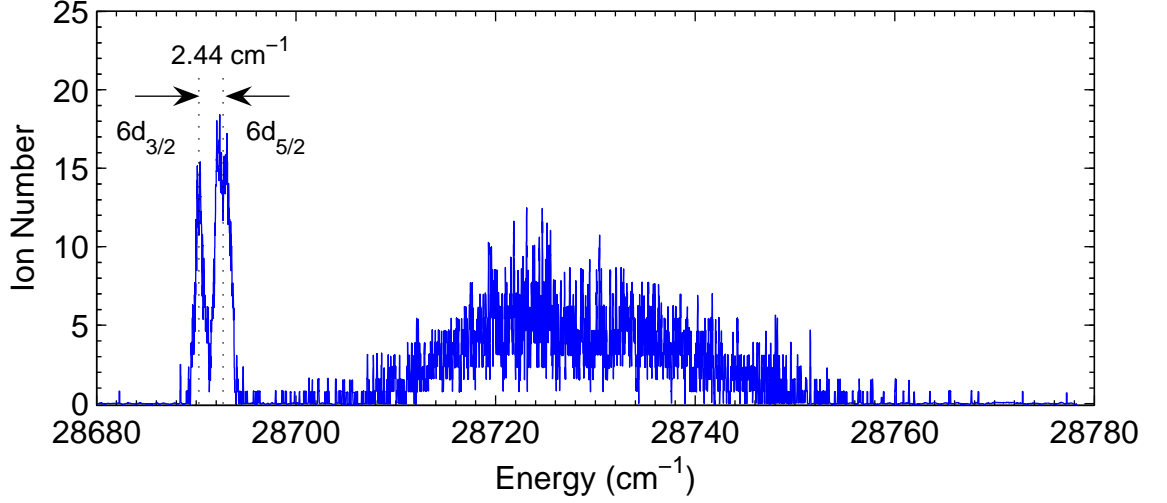
Fig. 4.7: $5p_{3/2} \rightarrow 6d$ transition with optical probe power of 124 μW. The fine structure of the transition is clearly resolved, with some evidence of further splitting possibly due to the electric field or hyperfine effects. A broad blue satellite can also be seen centred around 28,730 cm^{-1}. Its structure is not well resolved under these conditions, though there is some evidence of splitting into two or more components.

4.5 Measurement of Decay Curves

A series of ion decay curves were recorded for the nd states between n=12 and n=37. States belonging to the ns series were not measured as they overlap the blue satellites described above.

4.5.1 Time of Flight Spectra

An atom excited to an energy level within 12,820 cm^{-1} of the ionisation threshold (i.e all states where $n > 6$), can be ionised by the absorption of a single additional photon from the trapping, repump or probe light. Due to the short pulse length ($\approx$ 10 ns) of the probe laser those atoms which are ionised by this laser can be distinguished by the arrival time of the ions at the detector.

Figure 4.8 shows the ion TOF spectrum of an ensemble of atoms excited to the 13d
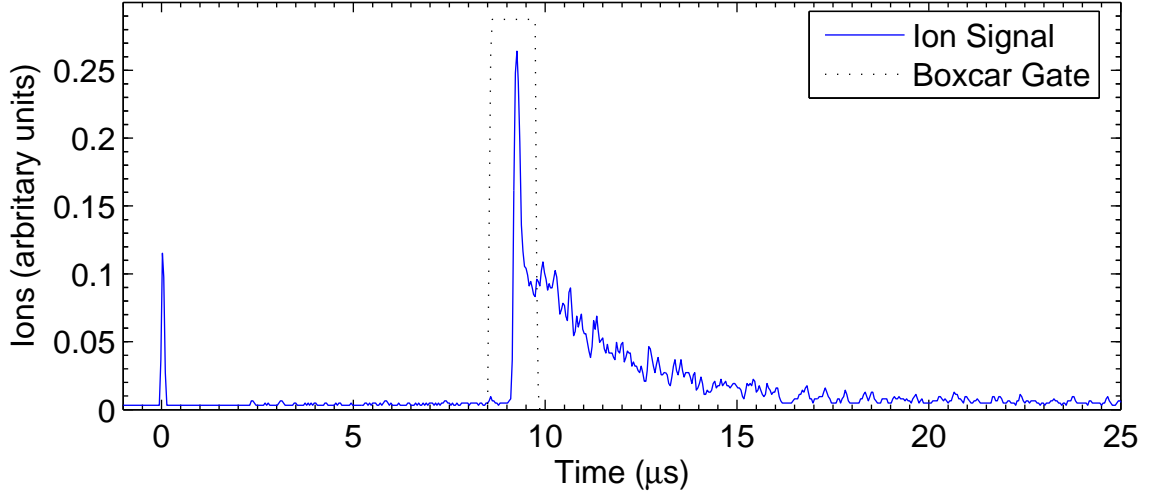
Fig. 4.8: Time of flight ion trace for the $5p_{3/2} \rightarrow 13d \rightarrow Rb^+$ state. The peak at time zero is from light scattered from the probe beam, the peak at 9.5 μs delay represent atomic ions ionised by the probe light, and the signal after 9.5 μs is from atomic ions ionised by the trapping and cooling light.

state by a probe pulse at time zero. The 13d state has a lifetime of order 3 μs, so that after the (10 ns) probe pulse atoms continue to be ionised by the trapping and repump light, until they are all ionised or have spontaneously decayed. Those atoms ionised in the absence of the probe pulse can be clearly seen on the time of flight spectrum as the exponentially decaying tail of ions extending out to about 20 μs. Also shown on Figure 4.8 for comparison is the boxcar gate which was used to count ions while recording the energy level spectra and shown previously in Figure 3.7.

4.5.2 Measurement of nd Decay Curves

Decay curves were measured after excitation to all of the nd states resolved in the earlier spectra up to n=37. Above n=10 the fine structure of the d states can no longer be resolved and both the $n\text{d}_{3/2}$ and $n\text{d}_{5/2}$ are simultaneously excited and contribute to the decay curves. For lifetime measurements the MOT was maintained at low densities ($< 10^{10}$ atoms/cm^3) to reduce collisional and collective effects such as super-radiance,

where spontaneously decaying atoms depopulate neighbouring levels by stimulated emission.

For the lifetime measurements the probe power was again maintained at 10 μJ/pulse. The LabView software used to collect data from the boxcar is too slow to acquire decay data; so a 60 MHz (Tektronix TDS1002) oscilloscope was used. The oscilloscope takes data directly from the CEM discriminator/preamplifier. After tuning the probe laser to the appropriate frequency, ion data was collected with each data point averaged over 64 pulses by the oscilloscope before the data was captured on the data acquisition computer through an RS232 serial port.

4.6 Decay Rate Model

The measured decay curves consist of a spectrum of detected ions versus arrival time at the detector. The measured signal thus represents decay from states which are detectable by ionisation detection to any state which is not detectable by ionisation detection. In this context "decaying" may refer to a range of processes such as ionisation, loss from the trap or excitation or decay into a dark state.

Spontaneous radiative decay is the main loss mechanism; however the ambient blackbody radiation redistributes population to nearby levels. For the optical ionisation detection used in these experiments all states with energy higher than the 6s state can be ionised by the absorbtion of a single photon. The measured decay rate is not simply the decay from the initial optically excited nd state but of total population N which includes those surrounding states subsequently populated by blackbody stimulated processes, each of which spontaneously decays at different rates. This necessitates the use of population rate-equations to model the measured decay curves, even after excitation to a single electronic state. Another consideration is the depletion of the excited state population N by the ionisation detection process. In principal depletion due to ionisation can be minimised by reducing the laser intensity, whilst the effects

of blackbody population transfer can be avoided by the use of state sensitive field ionisation.

4.6.1   Ionisation Depletion

Combining all non-ionisation decay processes into a single decay rate Γ the total loss rate is given by:

$$\frac{dN(t)}{dt} = -\Gamma N(t) - \frac{\sigma(n,l)}{h\nu_I} \ I \ N(t) \tag{4.12}$$

where I is the ionising (trapping + repump) light intensity with frequency ν_I and σ is the photo-absorption cross-section of the atom in state n, l.

The ionisation term in the rate equation can be made arbitrarily small by reducing the ionising light intensity, until the other decay terms dominate, provided there is still sufficient ionisation signal to record a TOF spectrum.

At low ionisation intensities there was no detectable change in the decay curves when varying the ionisation laser intensity. For the data which was compared to the rate equations, shown in Figures 4.13 and 4.14, the ionisation intensity was 4.8 mW/cm^2, where ionisation losses were not detectable. This justifies the exclusion of ionisation depletion in this decay-rate model.

4.6.2   Spontaneous Decay

In the dipole approximation the spontaneous decay rate from an atomic state a to state b with energy separation $\hbar\omega_{ab}$ is given by:

$$\Gamma_{radiative} = \frac{4\alpha}{3c^2} \ \omega_{ab}^3 \ |\langle b|r|a\rangle|^2 \tag{4.13}$$

where α is the fine structure constant. Since the radiative decay rates are proportional to the transition frequency cubed, radiative decay favours decay into the lowest allowed states. Thus nd states preferentially decay into the dipole allowed 5p state, and then into the 5s ground state. Atoms which have decayed into low lying states like the 5p and 5s state can no longer be ionised by a single photon process and so are measured as a decay in the ionisation time of flight spectra. All spontaneous decays are treated as a loss from the system in this model.

To first order in the quantum defects, the spontaneous atomic decay rates used in this model are recalled here [33], where Γ is in units ns^{-1}.

$$\Gamma_d(n) = (2.10 \ (n - 1.347157)^{2.89})^{-1} \tag{4.14}$$

$$\Gamma_p(n) = (2.80 \ (n - 2.65456)^{3.01})^{-1} \tag{4.15}$$

$$\Gamma_f(n) = (0.76 \ (n - 0.016312)^{2.95})^{-1}. \tag{4.16}$$

Below are the coupled rate equations governing the population of the p,d and f states N_p, N_d, N_f and the total population N, where all rates are a function of n^*.

4.6.3   Blackbody Population Transfer

Decay due to blackbody radiation is stimulated by the photons in the ambient radiation field. Since the transition is stimulated, the rate depends on the photon distribution of the ambient radiation. Explicitly the rate of stimulated transfer Γ_{bb} is weighted by the number of photons in the mode $h\nu$ from the ambient radiation with energy $k_B T$:

$$\Gamma_{bb} = \frac{1}{e^{h\nu/k_B T}} \ \Gamma_{radiative}. \tag{4.17}$$

In contrast to radiative decay, transitions stimulated by blackbody radiation favour close energy levels and these transitions can also occur to higher energy levels. Like radiative decay, dipole allowed transitions are preferred. After the initial excitation to a nd state, the most likely blackbody induced transitions are to the closest lying dipole allowed np and nf states at rates Γ_{pd} and Γ_{pf}.

Atoms that decay to these close lying states may still be detected by the ionisation system, in contrast to spontaneous decay products which are lost from the detection system.

However those atoms in the ns and nd states can still be lost from the detection system by spontaneous decay to a lower state. As discussed earlier the p states have a much smaller spontaneous decay rate than the neighbouring d states, while the f states have a larger spontaneously decay rate. Thus the measured decay of population N after excitation to a single Rydberg state does not obey a simple exponential decay as is shown later in Figures 4.10 and 4.11.

4.6.4   Decay Rate Equations

Figure 4.9 shows the energy levels and transitions that are considered in this model. The notation is $\Gamma_d=\Gamma(nd)$, $\Gamma_p=\Gamma(n+1)p$ and $\Gamma_f= \Gamma(n-1)f$.

After the initial excitation the total population of excited, ionisable atoms is N_0, all in a single nd state. Blackbody radiation then redistributes the population at a total rate $\Gamma_{bb} = (\tau_{bb})^{-1}$ determined by Equations 4.9 and 4.10 into nearby states determined by the branching ratios of the decay paths. The closest dipole allowed transitions are to the $(n\text{-}1)$f and $(n\text{+}1)$p states. This model only includes the closest neighbouring dipole allowed states, as the population of other dipole allowed np and nf states is smaller, and the decay rates of these states are similar to the neighbouring states; in terms of lifetimes $\tau(n,l) - \tau(n \pm 1, l) < \tau(n,l) - \tau(n, l \pm 1)$.
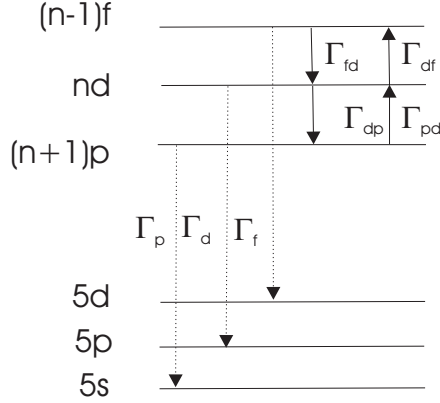
Fig. 4.9: Decay paths considered in the decay rate model. Γ_p, Γ_d, Γ_f are spontaneous decay rates, while Γ_{pd}, Γ_{dp}, Γ_{fd} and Γ_{df} are rates of population transfer due to blackbody radiation.

The rates of blackbody excitation Γ_{pd} and Γ_{fd} are given by:

$$\Gamma_{pd} = \frac{2\omega_{pd}|\langle (n+1)p|r|nd\rangle|^2}{2\omega_{pd}|\langle (n+1)p|r|nd\rangle|^2 + \omega_{pf}|\langle (n-1)f|r|nd\rangle|^2}\Gamma_{bb} \tag{4.18}$$

$$\Gamma_{fd} = \frac{\omega_{fd}|\langle (n-1)f|r|nd\rangle|^2}{2\omega_{pd}|\langle (n+1)p|r|nd\rangle|^2 + \omega_{pf}|\langle (n-1)f|r|nd\rangle|^2}\Gamma_{bb} \tag{4.19}$$

$$\Gamma_{dp} = \Gamma_{pd} \tag{4.20}$$

$$\Gamma_{df} = \Gamma_{fd} \tag{4.21}$$

where the relevant dipole matrix elements have been calculated [50] for all n considered here. All spontaneous decays are presumed lost to the system as the most likely decay products, with $n=5$, are no longer detected by the ionising laser.

$$\begin{bmatrix} \frac{dN_d(t)}{dt} \\ \frac{dN_p(t)}{dt} \\ \frac{dN_f(t)}{dt} \end{bmatrix} = \begin{bmatrix} -\Gamma_d - \Gamma_{dp} - \Gamma_{df} & \Gamma_{pd} & \Gamma_{fd} \\ +\Gamma_{dp} & -\Gamma_p - \Gamma_{pd} & 0 \\ \Gamma_{df} & 0 & -\Gamma_f - \Gamma_{fd} \end{bmatrix} \begin{bmatrix} N_d(t) \\ N_p(t) \\ N_f(t) \end{bmatrix} \tag{4.22}$$

which has the general solution in terms of the eigenvalues λ and eigenvectors $\vec{\eta}$:

$$\vec{N} = \sum_i C_i \, \vec{\eta_i} \, exp \, (\lambda_i \, t) \tag{4.23}$$

where λ_i is the ith eigenvalue, $\vec{\eta_i}$ is the ith eigenvector and the constants C_i are found from the boundary conditions, which specify that all of the atomic population N_0 starts in the nd state:

$$\begin{bmatrix} N_d(0) \\ N_p(0) \\ N_f(0) \end{bmatrix} = \begin{bmatrix} N_0 \\ 0 \\ 0 \end{bmatrix}. \tag{4.24}$$

The total population N, which is the variable measured in these experiments, is:

$$N(t) = N_p(t) + N_d(t) + N_f(t). \tag{4.25}$$

Matlab code was written to solve for $N(t)$ for n=12-37 and is included in an Appendix. The solution $N(t)$ and the population dynamics after excitation to two of the initial states considered here, $|12d\rangle$ and $|37d\rangle$, are shown in Figures 4.10 and 4.11.

In these plots $N_d(t)$ is a simple exponential decay, whereas $N(t)$, the quantity measured in the experiments, deviates significantly from exponential decay. The difference between $N(t)$ and $N_d(t)$ is a measure of the effects of the blackbody radiation, which increase with higher n as expected. The spontaneous decay rates from p states is less than the decay rates of d states, so population redistribution to neighbouring p states tends to increase the lifetime of the sample. Population transfer to f states, has the opposite effect of decreasing the sample lifetime.

The function $N(t)$ has a simplified form in the limits $\lim_{t\to 0} N(t) \to N_d(t)$ and $\lim_{t\to\infty} N(t) \to N_p(t)$. This is because all atoms are initially in the nd state but after long times only those in the longest lived np states remain and can be seen graphically as at short times
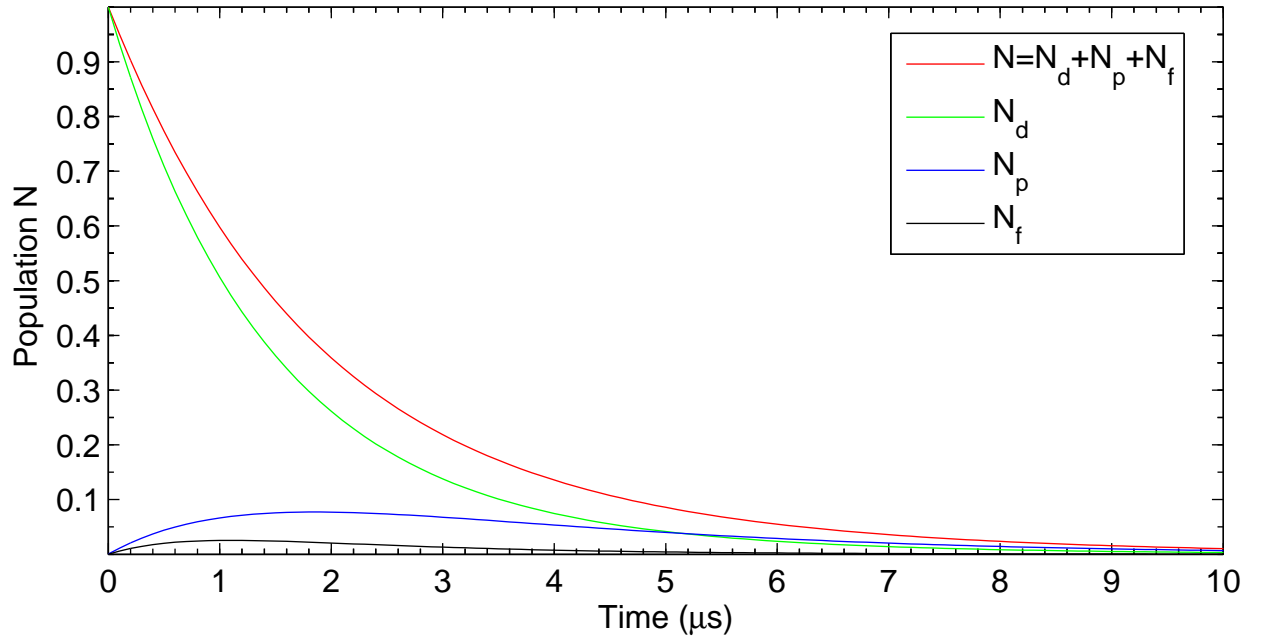
Fig. 4.10: Population dynamics after excitation to $|12d\rangle$.
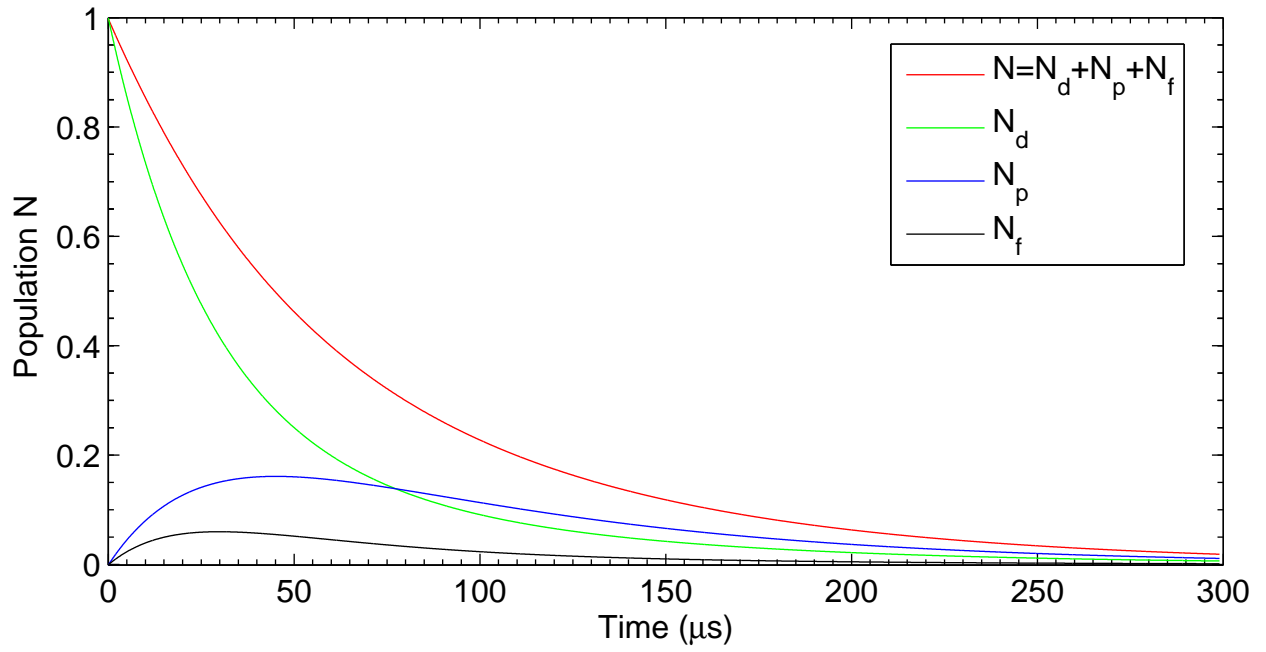
Fig. 4.11: Population dynamics after excitation to $|37d\rangle$.

N is close to $N_d(t)$, whilst at long time scales N is closest to $N_p(t)$. This variation in curvature over time illustrates the danger of fitting simple exponentials to determine atomic lifetimes, even for relatively low n. Such measurements will tend to overestimate the lifetime, particularly for higher n states. The fitted lifetime will depend on the time scale of the fit, being more accurate at smaller timescales.

The calculated decay curves for all of the states measured here are shown on the same axis for comparison in Figure 4.12.
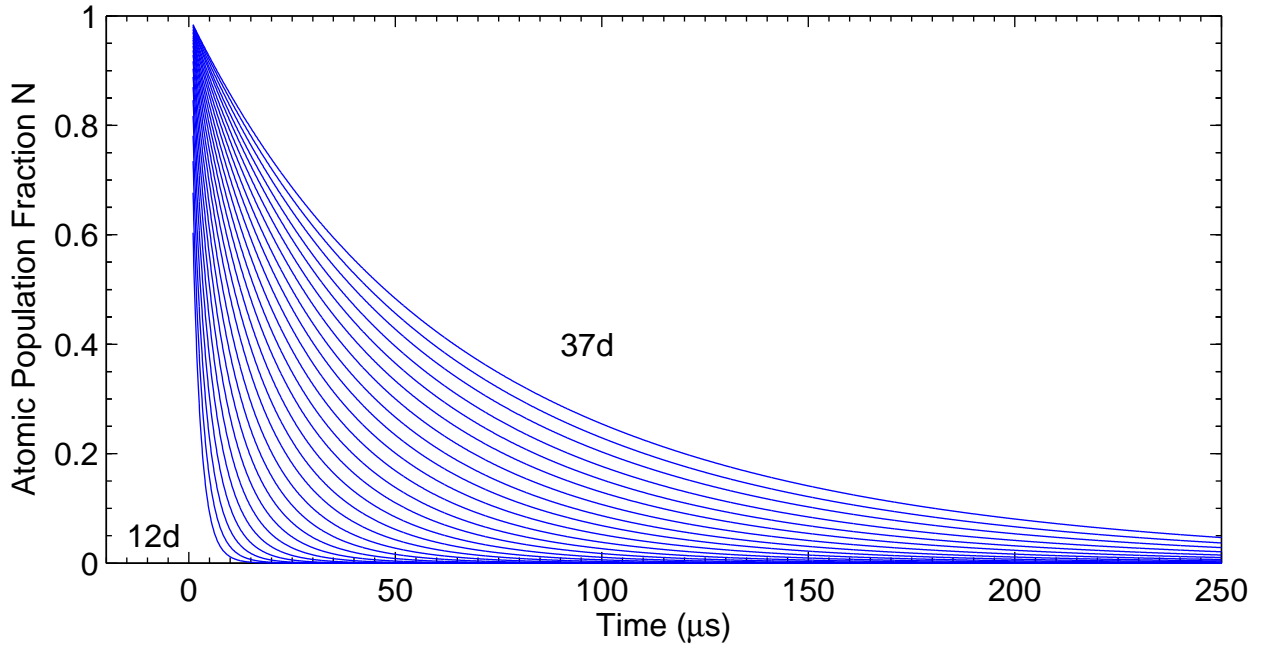
Fig. 4.12: Modelled decay curves for 12d-37d lifetime decay curves.

4.7 Lifetime Data

Whilst it is straightforward to evaluate the solution of Equation 4.23 given all the decay rates, the process is not as easily reversed. Even with the simple boundary conditions of Equation 4.24, $N(t)$ is composed of a number of exponentials with similar exponents, each a complicated function of the decay rate constants. It is not straightforward to

perform a reliable fit to extract the five independent decay constants (Γ_{pd}, Γ_{fd}, Γ_d, Γ_f, Γ_p) as well as $N_0 = N_d(t = 0)$.

For each measured state an experimental decay curve is measured. $N(t)$ is then calculated from Equation 4.22 for a given set of decay constants. The calculated $N(t)$ is then fitted to the data with two free parameters, the amplitude N_0 and an offset on the y-axis. The lifetime measurements together with the theoretical fits are shown in Figures 4.13 and 4.14. In Section 4.8 theoretical fits with different decay constants are compared allowing a comparison of models for the n^* dependance of some of the rate constants.

4.8   Blackbody Radiation Interaction

Given the spontaneous decay rates Γ_p, Γ_d and Γ_f, an analytical function of $N(t, \Gamma_{bb})$ can be found. The solution arises from the 3×3 matrix in Equation 4.22, where every nonzero matrix element has some Γ_{bb} dependence. An analytical form of $N(t, \Gamma_{bb})$ was evaluated in Matlab, but it extended over 83 pages and was computationally intensive.

Instead the fitting procedure was applied using the blackbody interaction rate constant $\Gamma_{bb}(n)$ as determined by the Farley model of Equation 4.9 and the Theodosiou model of Equation 4.10. The decay curve of the 16d state along with the fits of both models and residuals of both fits are shown in Figure 4.15. From the graphs and the residuals it can be seen that for the 16d state the Theodosiou model provides a better fit.

The "goodness of fit" of a model to measured values is measured by the coefficient of variation (R^2), a normalised sum of residuals, defined in Equation 4.26. An R^2 square of 1 indicates a perfect fit of the model to the data, and 0 indicates no correlation between the fit and the data.
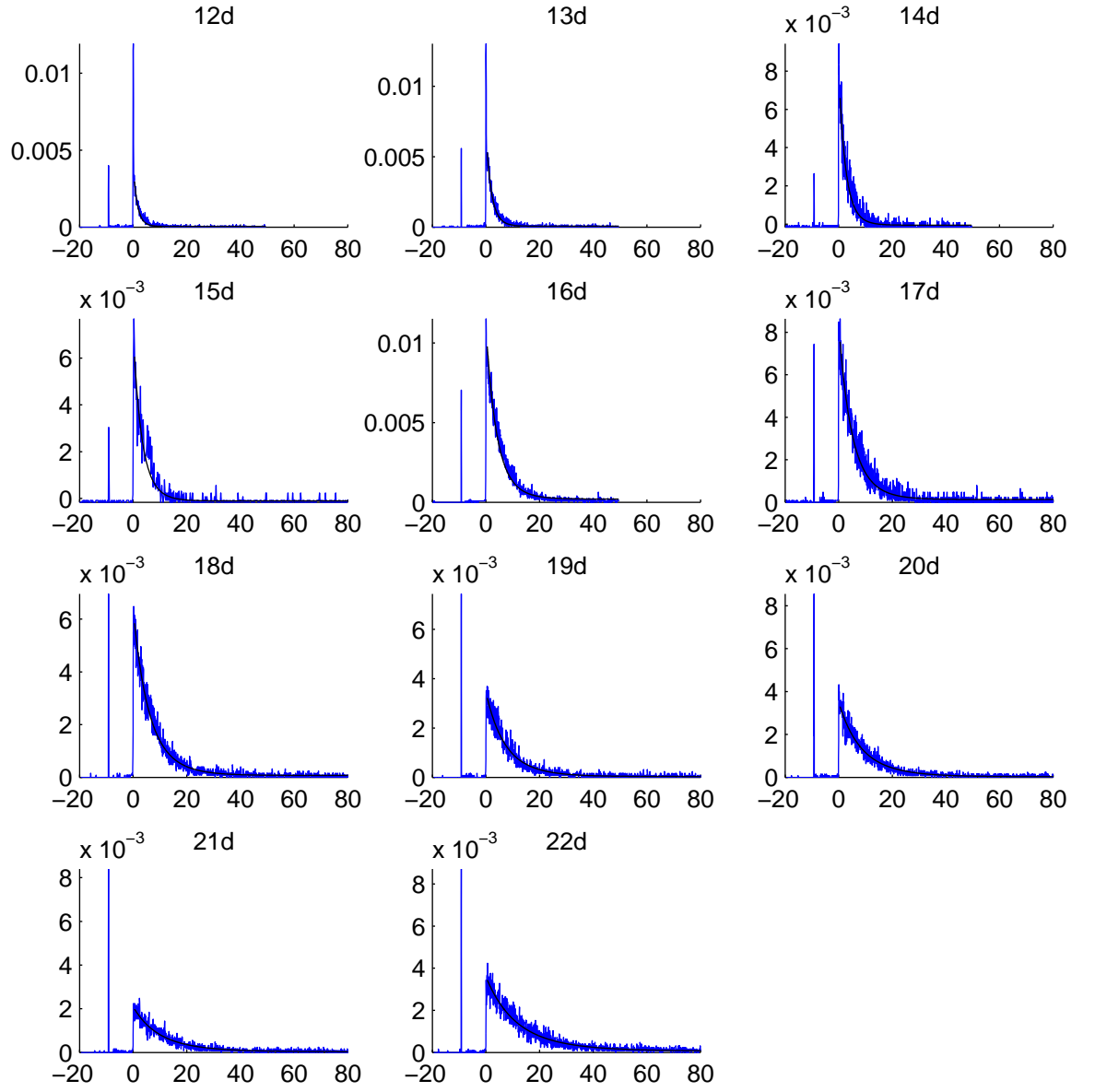
Fig. 4.13: Lifetime decay curves for n=12-22 where the x-axis is in μs and the y-axis is in arbitrary units.
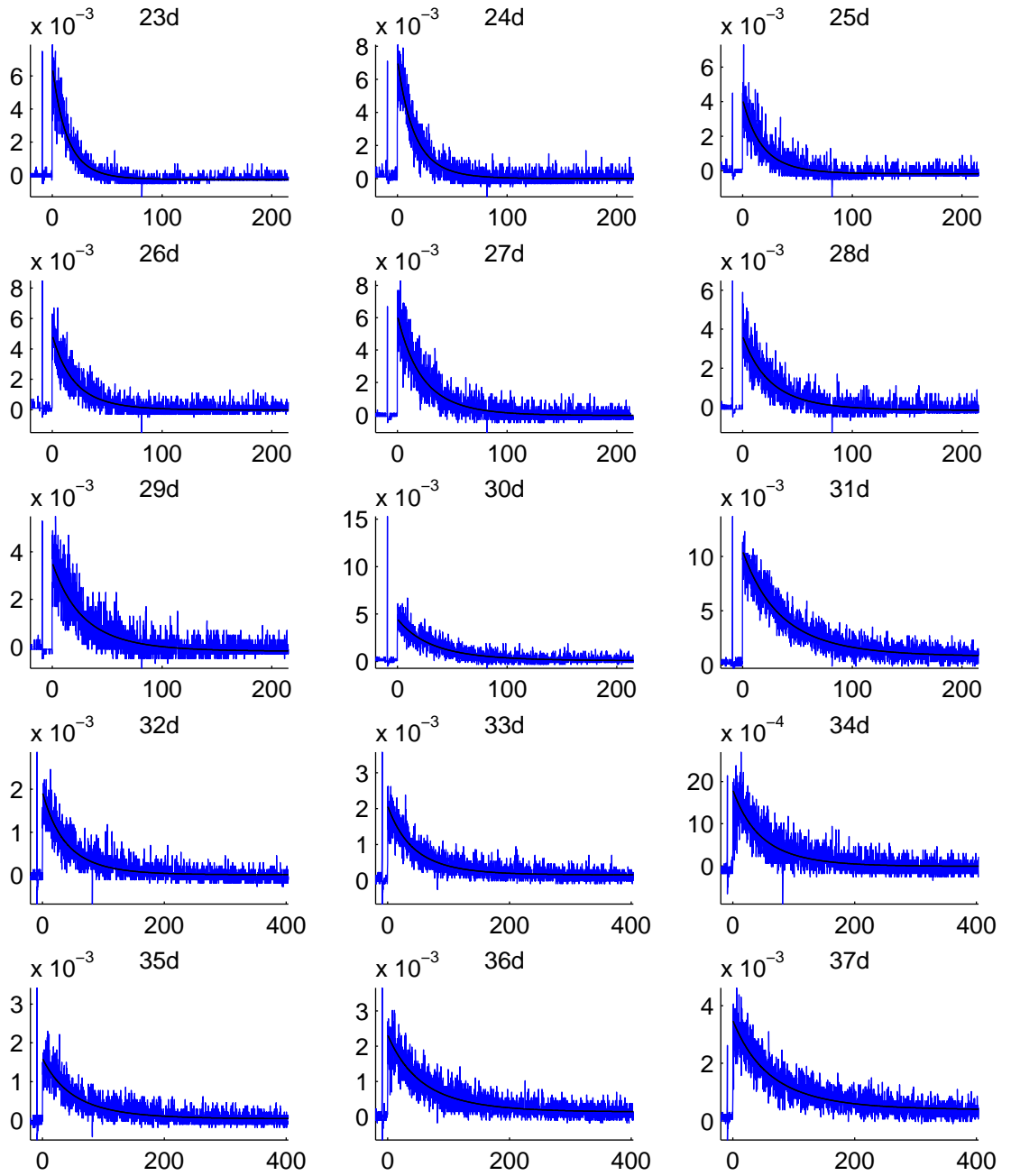
Fig. 4.14: Lifetime decay curves for $n=23\text{-}37$ where the x-axis is in μs and the y-axis is in arbitrary units.
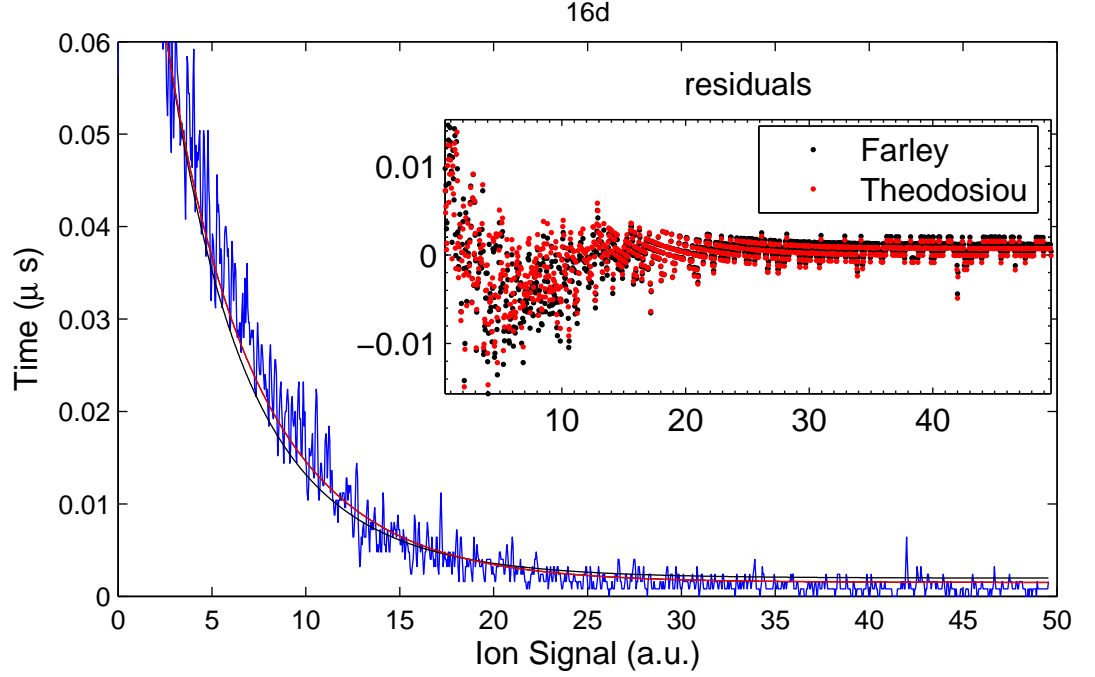
Fig. 4.15: The decay curve of the 16d state and the corresponding fit of N(t), using the blackbody coupling models of Farley and Theodosiou. The residuals of both fits are shown in the inset.

$$R^2 = \sum_{i=1}^{n} 1 - \frac{(y_i - \hat{y}_i)^2}{(y_i - \bar{y})^2} \tag{4.26}$$

where y_i is the ith measured value, $\hat{y}_i$ is the ith fitted value and $\bar{y}$ is the mean of the measured values.

The R^2 of each fit versus n of the initial excitation is plotted in Figure 4.16 for both models of blackbody interaction. Since most of the deviation between the modelled and measured results is attributed to noise in the data rather than deficiencies in the model, it is difficult to quantify the goodness of fit of a single model to the data. However when two models are fit to the same data set the difference in R^2 is a sensitive comparison of the models.

Both blackbody interaction calculations use a coulombic model; however the Theo-
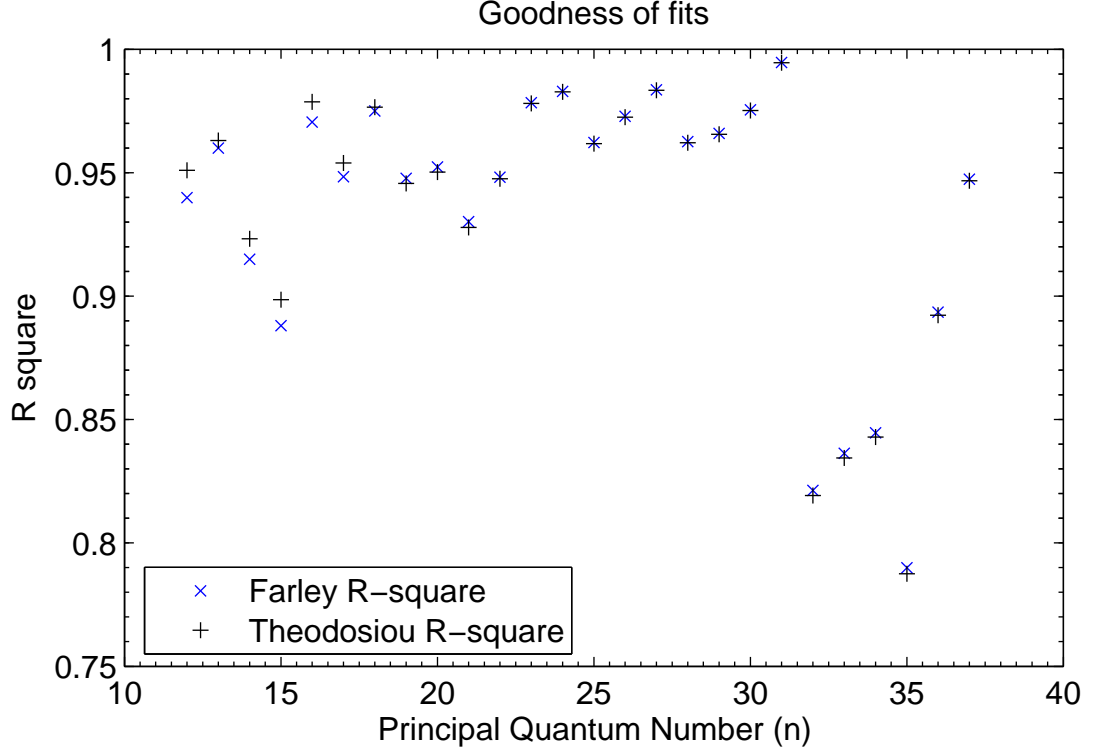
Fig. 4.16: The R square "goodness of fit" for the Farley and Theodosiou models fitted to the measured decay curves, as a function of the principal quantum number n. A value closer to 1 indicates a better fit to the data.

dosiou calculations modify the potential at short range to include spin orbit and core polarisability. The results of the Theodosiou calculations are tabulated for various temperatures up to $n=18$ and the results extrapolated to higher n. The simpler Farley model has a convenient analytical solution which should increase with accuracy at higher n, as core effects are smaller.

The R^2 plot in Figure 4.16 shows that the Theodisiou model of blackbody radiation interaction gives better agreement with the data for states up to $n=18$, where Farley's model underestimated the blackbody depopulation rate. Between $n=18$ and $n=30$ both models are in good agreement; however the Farley model is more accurate for all $n > 18$. Beyond $n=28$ the Theodisiou model underestimates the blackbody depopulation rate. These results are for excitation to $l = 2$ states; however the l dependence of Γ_{bb} is weak,

so that the conclusions should extend to other states with similar principal quantum number n.

Chapter 5

Diatomic Molecules and Photo-association

> "Every attempt to employ mathematical methods in the study of chemical questions must be considered profoundly irrational and contrary to the spirit of chemistry.... if mathematical analysis should ever hold a prominent place in chemistry – an aberration which is happily almost impossible – it would occasion a rapid and widespread degeneration of that science."
>
> — Auguste Comte, *Cours de philosophie positive, 1830*

5.1 Schrödinger Equation for Diatomic Molecules

The Schrödinger equation for two atoms or a diatomic molecule is made up of nuclear and electronic kinetic energies T_n and T_e, the electrostatic potential arising from nuclear-nuclear V_{nn}, nuclear-electronic V_{ne} and electronic-electronic V_{ee} interactions and relativistic terms V_{rel} such as spin-orbit coupling. The Hamiltonian H for the diatomic molecule is:

$$H = T_n + T_e + V_{ne} + V_{nn} + V_{ee} + V_{rel}. \tag{5.1}$$

In terms of atomic number Z, nuclear mass M, electronic mass m, elementary charge e, nuclear co-ordinate $\vec{R}$ and electronic co-ordinate $\vec{r}$:

$$T_n = -\sum_i \frac{\hbar^2}{2M} \nabla^2(\vec{R}_i) \tag{5.2}$$

$$T_e = -\sum_i \frac{\hbar^2}{2m} \nabla^2(\vec{r}_i) \tag{5.3}$$

$$V_{ne} = -\sum_i \sum_j \frac{Z_i e^2}{4\pi\varepsilon_0 |\vec{R}_i - \vec{r}_j|} \tag{5.4}$$

$$V_{ee} = +\sum_i \sum_{j>i} \frac{e^2}{4\pi\varepsilon_0 |\vec{r}_i - \vec{r}_j|} \tag{5.5}$$

$$V_{nn} = +\sum_i \sum_{j>i} \frac{Z_i Z_j e^2}{4\pi\varepsilon_0 |\vec{R}_i - \vec{R}_j|}. \tag{5.6}$$

Under the Born-Oppenheimer, or adiabatic approximation, nuclear and electronic motion are decoupled. Since the electrons and nucleus feel the same electrostatic force, and the electron is orders of magnitude lighter, the electron wavefunction is always in equilibrium with the slow nuclear motion. Initially the nuclear kinetic energy term T_n is neglected and the electronic Schrödinger equation is solved for a range of fixed nuclear coordinates $\vec{R}$. The solution is an electronic potential surface $V(\vec{R})$ for each quantum state, known as adiabatic Born-Oppenheimer potentials.

In the second step of the Born-Oppenheimer approximation the part of the Hamiltonian H that depends on the electrons is replaced by the potential energy surface $V(\vec{R})$. This converts the total molecular Hamiltonian into a Hamiltonian which acts only on the nuclear coordinates $\vec{R}$.

For a diatomic molecule, the Hamiltonian can be separated into angular and radial

parts. The angular part is expressed in terms of spherical harmonic functions $Y_{lm}(\theta, \phi)$, and the radial motion is expressed in terms of relative motion $R = |\vec{R}_1 - \vec{R}_2|$ and centre-of-mass motion $\vec{R}_{com}$. The centre-of-mass equation of motion is the same as for a free particle. The relative radial motion is governed by the Schrödinger equation, for a diatomic molecule it is:

$$\left[-\frac{\hbar^2}{2\mu}\frac{d^2}{dR^2} + V(R) + \frac{\ell^2}{2\mu R^2} \right] \Psi(R) = E\ \Psi(R) \tag{5.7}$$

where the reduced mass $\mu = \frac{M_1 + M_2}{M_1 M_2} = M/2$ for a homo-nuclear diatomic molecule, R is the internuclear separation $|\vec{R}_1 - \vec{R}_2|$, $V(R)$ is the rotationless Born-Oppenheimer potential, and ℓ is the nuclear orbital angular momentum operator.

The Born-Oppenheimer potentials $V(R)$ for the ground and excited states of Rb_2 are discussed in Section 5.3. The allowed energies E of the discrete vibrational levels in the potential are discussed in Section 5.6 and the radial one-dimensional wave-functions Ψ are discussed in Section 5.7.

5.2   Angular Momentum Coupling

Ignoring the weak hyperfine interaction, the radial Schrödinger Equation 5.7, contains the nuclear rotation and $V(R)$ which contains the electrostatic and spin-orbit interactions. The relative strength of the nuclear rotation, electrostatic, and spin-orbit interaction determines the coupling of the underlying angular-momenta and therefore the most appropriate quantum numbers which describe the molecule. Hund's cases are limiting cases which describe the angular-momenta coupling.

The most appropriate Hund's case can vary for different molecular states. The ground state, made up of two 5s atoms, has no orbital angular momentum and therefore no spin-orbit interaction. It is described by the total spin quantum numbers $\vec{S} = \vec{s_1} + \vec{s_2}$.

States asymptoting to the 5s+5p limit are well described by the total spin quantum number S when the spin-spin interaction is strong. This is the case near the bottom of the potential well at ≈ 4 Å. At longer range where the spin-orbit interaction $\langle \vec{L}.\vec{S} \rangle$ becomes larger than the spin-spin $\langle \vec{S}.\vec{S} \rangle$ interaction, S is no longer a good quantum number and the molecule is described by Hund's case C angular-momenta coupling. At infinitely large R there is no interaction between atoms and the molecular potential is labelled by the separated atom quantum numbers, in this case 5s+5p$_{3/2}$.

5.2.1 Hund's Case A Labels

At small internuclear separations the electronic motion couples with the rotation of the molecule according to Hund's case A, as shown in Figure 5.1. The total orbital angular momentum $\vec{L} = \vec{l_1} + \vec{l_2}$ and spin $\vec{S} = \vec{s_1} + \vec{s_2}$ precess around the internuclear line, and their respective projections onto the internuclear axis Λ and Σ as well as $\Omega = L + S$ are good quantum numbers. The total angular momentum for the molecule is $\vec{J} = \vec{L} + \vec{N} + \vec{S}$, where $\vec{N}$ is the orbital angular momentum of the nuclei, which is perpendicular to the internuclear axis of the molecule.

States are labelled with $^{2S+1}\Omega$ and with additional symmetries g(u), for gerade (ungerade), if the wave-function is symmetric (antisymmetric) on inversion of the electronic co-ordinates through the molecule centre of mass as the origin. For the case where Ω=0, the states are labelled with an additional reflexion symmetry +(-) if the wave-function is symmetric (antisymmetric) when reflected through any plane containing the internuclear axis.

5.2.2 Hund's Case C Labels

At the relatively large internuclear separations where photoassociation transitions are strong, the electric field along the internuclear axis is weak and Λ and Σ are no longer

good quantum numbers. In Hund's case C, the orbital angular momentum and spin couple to form $\vec{j} = \vec{S} + \vec{L}$, and the projection of $\vec{j}$ onto the internuclear axis Ω is a good quantum number. Hund's case C labelling convention is $\Omega_{u/g}^{+/-}$, where gerade, ungerade and reflexion symmetries are the same as for Hund's case A.
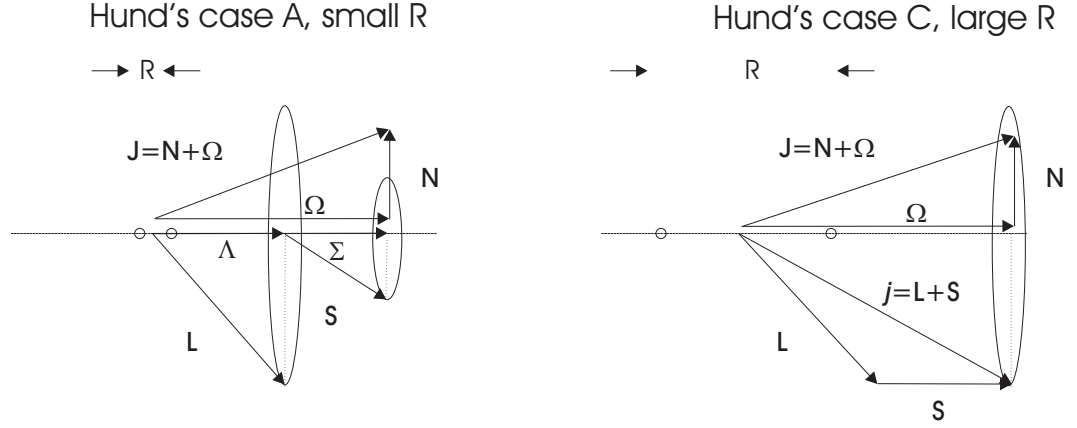
Fig. 5.1: Vector coupling and projection for Hund's case A and C.

5.3 Asymptotic Potential Approximation

At large internuclear separations, where the short-range chemical exchange overlap interactions are small, the potential $V(R)$ is largely determined by the coulomb interaction and higher order corrections. This is the case beyond the modified Le-Roy radius, $R > 20$ Å, for Rb_2 [52]. The electronic potential of molecular states beyond this range can be expanded in terms of multi-poles:

$$V(R) = D_e + \sum_n \frac{C_n}{R^n} \qquad (5.8)$$

where D_e is the dissociation energy, R the internuclear separation and the constants C_n can be calculated using perturbation theory. Terms arising from the first order perturbation theory are n=3, 5, 7,... They correspond to interactions between

permanent electric multi-poles, with the R^{-3} term corresponding to dipole-dipole coupling and the R^{-5} term to quadrupole-quadrupole coupling.

Neutral ground state atoms have no permanent electric dipole moments and even excited states have small higher order multipoles. However identical atoms in electronic states connected by an allowed electric dipole transition behave like electrostatic dipoles. The atoms interact with an R^{-3} potential, with the C_3 coefficient proportional to the square of the dipole matrix element connecting them.

The second order perturbation terms n=6, 8, 10,... are called dispersion coefficients and arise from coupling between induced multipole coupling. They are calculated from the polarisability of the various multipoles, with the R^{-6} term corresponding to the interaction between induced dipoles, R^{-8} induced quadrupoles and so on. Third order perturbation terms (neglected here) arise from interactions between permanent and induced multi-poles.

The asymptotic potential approximation fails at small R when exchange energy dominates Coulomb energy, for Rb_2 when $R < 20$ Å [52]. It also fails when the Coulomb interaction energy becomes comparable to the hyperfine interaction energy (0.2 cm^{-1} at dissociation), for $R > 148$ Åfor ^{87}Rb. At very large R the dominant interaction is also modified by retardation effects giving rise to the Casimir-Polder potential with an R^{-7} dependence [53].

5.3.1 Ground State Potential

Neglecting fine and hyperfine structure, the molecular states which asymptote to the 5s+5s dissociation limit are the $^1\Sigma_g^+$ and $^3\Sigma_u^+$ states, using Hund's case A labels. As they possess no permanent dipole moment and are not connected by a dipole allowed transition, the leading terms in the asymptotic expansions for both potentials are the n=6, 8, 10,... dispersion terms. The two potentials are shown in Figure 5.2; at short range, where exchange energy dominates, they diverge. At long range where Van
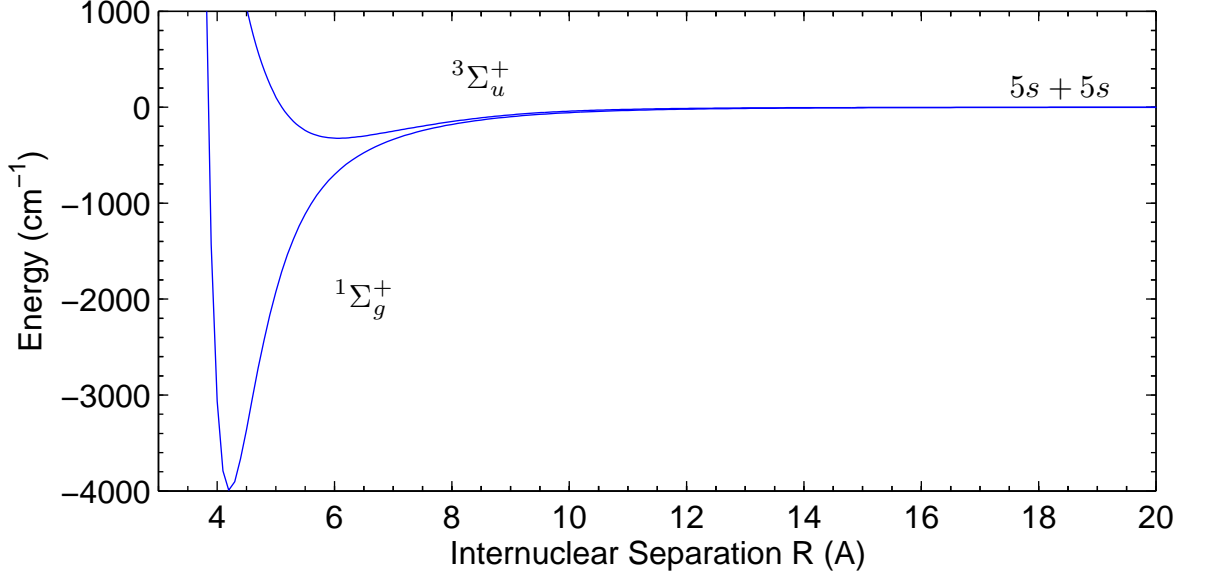
Fig. 5.2: Ground-state singlet [54] and triplet Born-Oppenheimer potentials for Rb_2. The triplet potential parameters are taken from [55] with the correct long range behaviour imposed using the long range C_6 [56] and C_8 and C_{10} [57] dispersion coefficients.

der Waals energy dominates, they are degenerate since both S-state potentials have exactly the same dispersion coefficients. To first order, at long range, the ground state potentials takes the form:

$$V_{5s+5s}(R) = -\frac{C_6}{R^6}.$$

(5.9)

5.3.2   Excited State Potentials

In a non-relativistic picture there are eight Hund's case A adiabatic molecular potentials which correspond to free 5s+5p Rb atomic states. These states have the form Σ or Π, with singlet or triplet and gerade or ungerade symmetry. In order of decreasing binding energy they are $^3\Pi_u$, $^1\Sigma_u^+$, $^1\Sigma_g^+$, $^3\Sigma_g^+$, $^1\Pi_u$ and $^1\Pi_g$ with the $^3\Pi_g$ and $^3\Sigma_u^+$ states repulsive at long range. These short range potentials are shown in Figure 5.3.
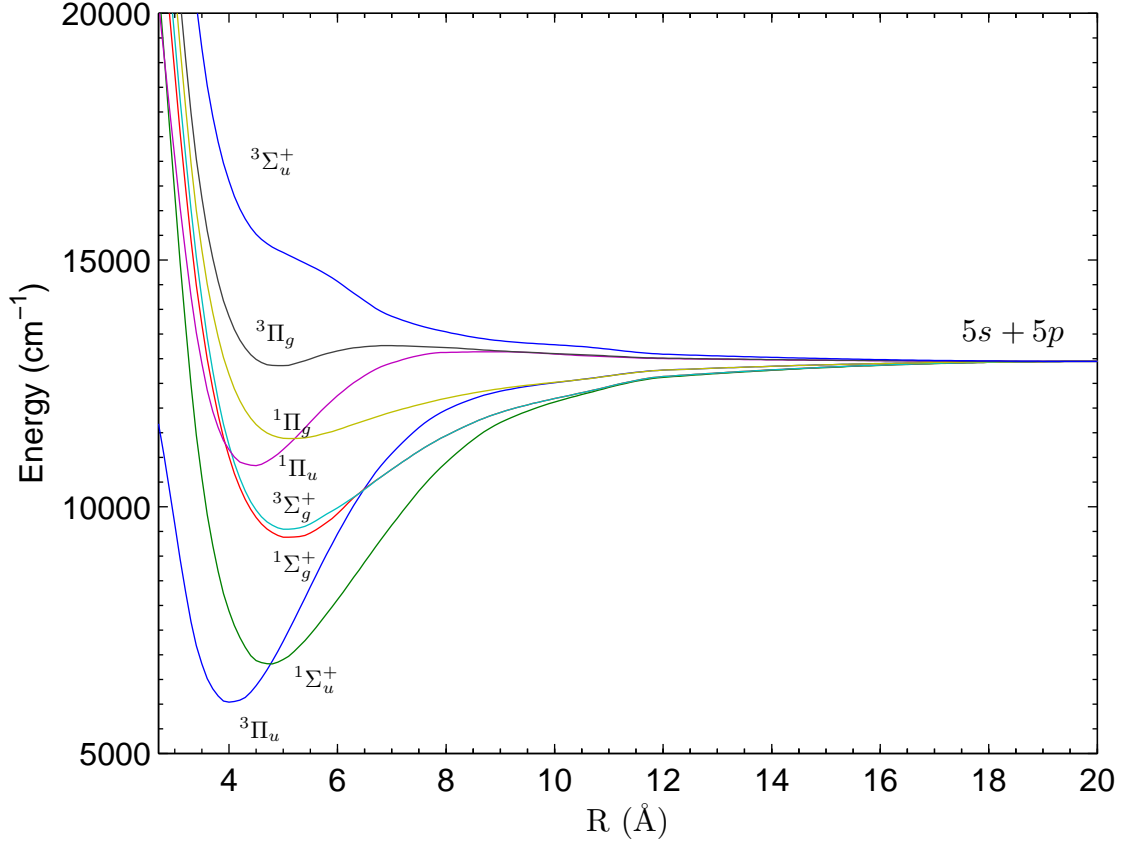
Fig. 5.3: The eight non relativistic adiabatic Born-Oppenheimer potentials in Hund's case A, which asymptote to the 5s+5p free atomic states [58].

The potentials of all states corresponding to the 5s+5p atomic limit are a result of the resonant dipole-dipole C_3/R^3 interaction. This interaction is extremely long range compared to the C_6/R^6 ground-state interactions, as can be seen by comparing the excited state potentials and ground state potentials shown later in Figure 5.7.

Figure 5.3 shows that the strength and sign of the resonant dipole interaction depends on the singlet or triplet symmetry of the electronic wave function. The eight potentials fall into four groups of 2 and can all be written in terms of a single constant C_3 which is proportional to $|\langle 5s|er|5p\rangle|^2$. The Σ states go as $\pm 2C_3/R^3$ while the Π states go as $\pm C_3/R^3$ [59].

5.4 The Movre-Pichler Model

The dispersion coefficients and resonant-dipole interaction determine the largest part of the potential at the long ranges where photo association (PA) occurs. Relativistic effects, leading to fine and hyperfine structure, are small by comparison but are still large compared to the collisional energy scales for ultracold atoms and molecules. The dominant relativistic contribution is from spin orbit coupling [60], which at large internuclear separation can be accounted for using the atomic fine structure splitting.

The Movre-Pichler model combines the C_3/R^3 resonant dipole and the free atom spin-orbit interactions $A\langle \vec{l}.\vec{s}\rangle$, where A is the atomic spin orbit constant, which is valid at large R. It gives an improved relativistic picture compared to the Hund's case A curves of Figure 5.3, and is valid at larger R. Figure 5.4 shows the 16 Hund's case C potentials which asymptote to the 5s + 5p dissociation limit [61].

At short range the potentials with Hund's case C labels all correlate to Hund's case A states as shown in Table 5.1.

Table 5.1: Hund's case A and C behaviour of potentials

Hunds Case A (5s+5p)	Hunds Case C (5s+5p$_{3/2}$)	Hunds Case C (5s+5p$_{1/2}$)
$^1\Sigma_g^+$	0_g^+	
$^1\Sigma_u^+$		0_u^+
$^3\Sigma_g^+$		$0_g^-, 1_g$
$^3\Sigma_u^+$	$0_u^-, 1_u$	
$^1\Pi_g$	1_g	
$^1\Pi_u$	1_u	
$^3\Pi_g$	$0_g^-, 1_g, 2_g$	0_g^+
$^3\Pi_u$	$0_u^+, 2_u$	$0_u^-, 1_u$

For the heavier alkali-metal dimers like Rb$_2$ it is necessary to correct for chemical bonding, higher-order dispersion contributions (C_6/R^6,...) and atomic relativistic corrections, which lifts the degeneracy of the 5p$_{3/2}$ and 5p$_{1/2}$ states. For all alkali-metal dimers it is important to include hyperfine interactions, nonadiabatic corrections, and
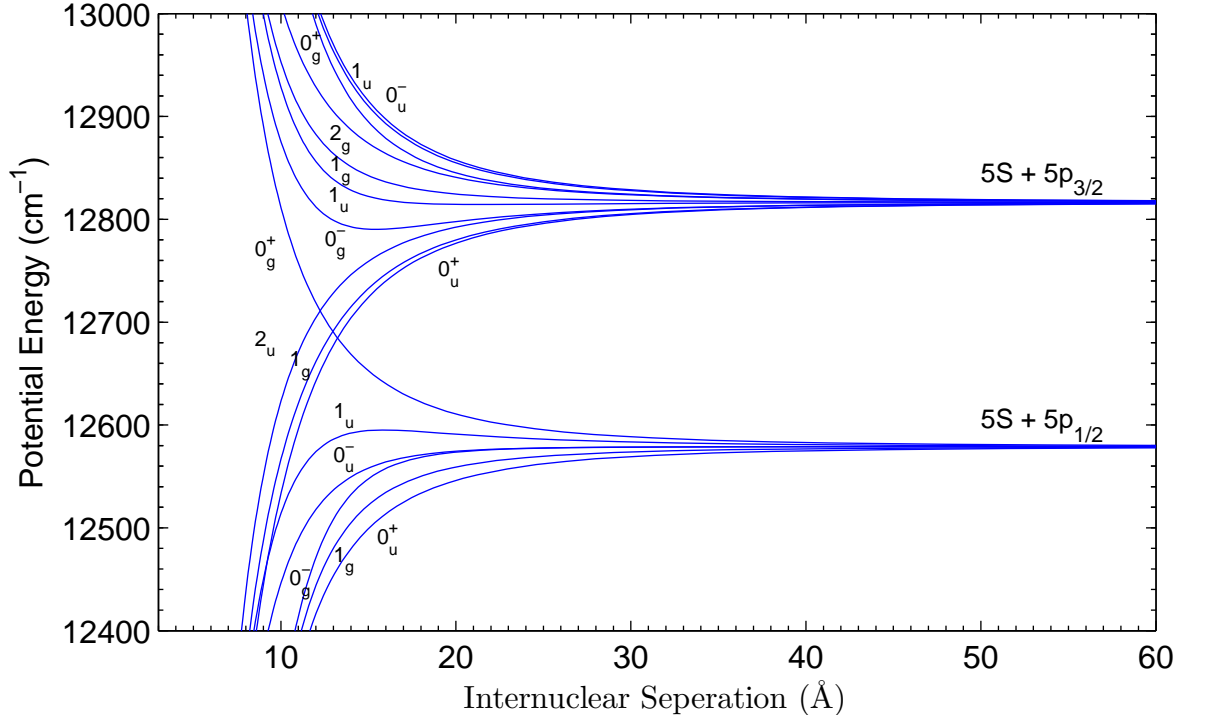
Fig. 5.4: Attractive Rb_2 molecular states assymtoting to the 5s + 5p atomic states for Hund's case C angular-momentum coupling. These potentials are calculated using the Movre-Pichler model [61].

retardation corrections to the resonant dipole interaction [59].

5.5 Hyperfine Structure

At long range ($R > 148$ Åfor $^{87}Rb_2$) the hyperfine interaction energy (0.2 cm^{-1} at dissociation) is comparable to the resonant-dipole interaction energy. It is also comparable in energy to the rotational structure of the molecule.

The atomic hyperfine interaction $\propto \langle \vec{s}.\vec{i} \rangle$, couples the nuclear spin $\vec{i}$ to the electronic spin $\vec{s}$. At short range the coupling is $\propto \langle \vec{S}.\vec{I} \rangle$ where $\vec{I} = \vec{i}_1 + \vec{i}_2$. At very long range the potentials can be labelled by the atomic hyperfine labels $\vec{f}_1 = \vec{j}_1 + \vec{i}_1$ and $\vec{f}_2 = \vec{j}_2 + \vec{i}_2$.

The hyperfine interaction can couple Born-Oppenheimer potentials with different g/u symmetry or different total electron spin $\vec{S}$, so that total parity, rather than electronic parity, is conserved.

States with $\Omega = 0$ (Hund's case C label) such as the 0_u^+ state have no hyperfine structure to first order and should exhibit a pure $J(J+1)$ rotational progression. States with $\Omega > 0$ such as the 1_g state exhibit hyperfine structure on a similar scale to the molecular rotational structure.

The calculation of molecular hyperfine potentials requires a multi-channel treatment [59]. For the $^{87}\mathrm{Rb}_2$ dimer there are a total of 384 distinct basis functions which are needed to define the Hamiltonian matrix from which the hyperfine adiabatic potential curves are calculated [28]. Hyperfine structure is resolved in the experiments presented here.

5.6   Le-Roy Formalism and Vibrational Energies

In the first order semiclassical Jeffreys-Wentzel-Kramers-Brillouin (JWKB) approximation the energy levels $E(v)$ of the bound vibrational states v, in the one dimensional potential $V(R)$, are given by:

$$v + \frac{1}{2} = \frac{\sqrt{2\mu}}{\pi\hbar} \int_{R_-(v)}^{R_+(v)} \sqrt{E(v) - V(R)} \ dR \tag{5.10}$$

where μ is the reduced mass, and $R_-(v)$ and $R_+(v)$ are the inner and outer classical turning points of the vibrational level v. The density of vibrational states can be evaluated:

$$\frac{dv}{dE(v)} = \frac{\sqrt{\mu}}{\sqrt{2}\pi\hbar} \int_{R_-(v)}^{R_+(v)} \frac{1}{\sqrt{E(v) - V(R)}} \ dR. \tag{5.11}$$

Inserting the long range form of the potential $V = \sum C_n R^{-n}$, and treating the discrete v as a continuous variable, in the limit $R_+/R_- \to \infty$ the expression can be evaluated analytically giving to first order of C_n [62]:

$$E(v) = D_e - (v_D - v)^{\frac{2n}{n-2}} \left(\sqrt{\frac{\pi}{2\mu}} \frac{\Gamma(1+1/n)}{\Gamma(1/2+1/n)} \frac{\hbar(n-2)}{(-C_n)^{1/n}} \right)^{\frac{2n}{n-2}} \tag{5.12}$$

where v_D is the hypothetical non-integer last bound vibrational level with dissociation energy D_e, n is the exponent of the leading term in the potential and $\Gamma(x)$ is the gamma function.

For potentials asymptoting to the 5s+5p$_{3/2}$ limit, the leading term in the expansion is $n=3$ due to the resonant-dipole interaction, and the LeRoy Bernstein equation for the vibrational energy is:

$$E(v) - D_e = -\left(\sqrt{\frac{\pi}{2\mu}} \frac{\Gamma(4/3)}{\Gamma(5/6)} \frac{\hbar}{(-C_3)^{1/3}} \right)^6 (v_D - v)^6. \tag{5.13}$$

An improved Le Roy-Bernstein formula [63] gives a second order correction to the approximation:

$$E(v) = D_e - \left(H_n(v_D - v) \right)^{\frac{2n}{n-2}} \left[1 - \gamma \frac{2n}{n-2} \left(H_n(v_D - v) \right)^{\frac{2n}{n-2}-1} \right] \tag{5.14}$$

where

$$H_n = \sqrt{\frac{\pi}{2\mu}} \frac{\Gamma(1+1/n)}{\Gamma(1/2+1/n)} \frac{\hbar(n-2)}{(-C_n)^{1/n}}. \tag{5.15}$$

This approximation is still subject to many constraints and can be applied only in the range of validity of the potential from Equation 5.8, which does not include relativistic terms such as fine or hyperfine effects, exchange energy, higher order electrostatic terms, or retardation effects.

5.7 Radial Wave-functions

Excited State Wave-functions

Bound wave-functions are calculated numerically with LEVEL, a freely distributed program that implements the Cooley-Numerov method to determine wave-functions given a rotationless potential $V(R)$ [64]. A brief description of the procedure follows.

Boundary conditions specify $\Psi(R = 0) = 0$ and $\Psi'(R = 0)$ is small; these conditions are used to guess neighbouring grid points around $R = 0$. Equation 5.7 relates $\Psi''(R)$ to $\Psi(R)$ for the given potential $V(R)$ and some energy E. This relationship is applied to numerically integrate $\Psi(R)$ outwards from the first two points at a given energy E_1 around $R = 0$.

As $R \to \infty$ the value of two neighbouring grid points are determined by the JWKB method. Numerical integration then proceeds inward using Equation 5.7 with the same energy and potential as for the outward case. The number of nodes in the wave-function and the overlap of the inward and outward propagated functions are then used to improve the estimate of the energy. The solution is then iterated with the same potential and the new energy E_2 until a self consistent $\Psi(R)$ is determined within the desired accuracy.

Ground State Scattering Wave-function

The unbound or scattering radial wave-function takes a simple form at long range $(R > 43.5 \text{ Å})$ for the case of s-wave scattering $(T < 80 \text{ } \mu \text{ K})$ [65]:

$$f(R, E) \to \left(\frac{2\mu}{\pi\hbar^2}\right)^{1/2} \frac{\sin(kR + \eta)}{\sqrt{k}} \tag{5.16}$$

where $E = \hbar^2 k^2/(2\mu)$, η is the collisional phase shift, and the unbounded wavefunction

is normalised per unit energy.

At shorter range ($R < 43.5$ Å), the potential is deep enough to cause significant acceleration, or curvature in the wave-function. Here the radial wave-function can be written in phase amplitude form [66] [67]:

$$f(R, E) = \left(\frac{2\mu}{\pi\hbar^2}\right)^{1/2} \frac{1}{C(E)} a(R, E) \sin(b(R, E)) \tag{5.17}$$

where $1/C(E)$ is an R independent normalisation factor that relates the actual wave-function to the JWKB wave-function. For $R < 43.5$ Åand $T < 350$ μK, $a(R, E)$ and $b(R, E)$ are well approximated by a standard JWKB form. In terms of the local wavenumber k_{local} [59]:

$$a(R, E) = \frac{1}{\sqrt{k_{local}(R, E)}} \tag{5.18}$$

$$b(R, E) = \int k_{local}(R', E) dR' + \frac{\pi}{4} \tag{5.19}$$

$$k_{local}(R, E) = \sqrt{k^2 - 2\mu V(R)/\hbar^2}. \tag{5.20}$$

The ground and excited state wave-functions for unbound atoms, and for a singly excited potential, are shown in Figure 5.7.

5.8   Photoassociation Process

Photoassociation (PA) occurs when two free ground state atoms absorb a resonant photon during a collision and form an electronically excited bound molecule. The free atoms in this case are a sample of magneto-optically trapped Rb atoms, whose energy distribution is characterised by a temperature $T = 120$ μK corresponding to a

collisional energy spread of 2 MHz. Since the energy distribution of the free atoms is comparable to the natural width of the bound levels, the transition behaves resonantly.

Photoassociation spectroscopy is depicted in Figure 5.5. The probe frequency ν is scanned, and when it is resonant with a free-bound transition (ν_0) molecules are formed and a signal is recorded in the photoassociation spectrum. The Condon point R_c is the equilibrium internuclear separation of a resonant transitions.
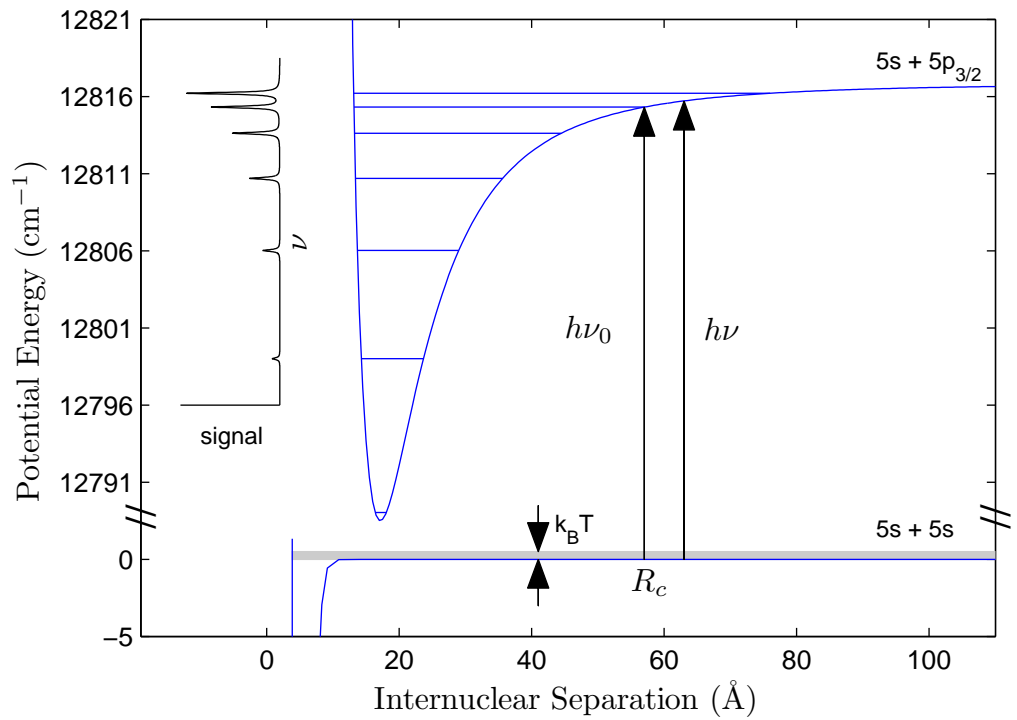
Fig. 5.5: Schematic of photoassociation spectroscopy with a corresponding photoassociation signal. The Condon point R_c is the internuclear separation where a resonant transition is most likely to occur.

As discussed in Section 5.3, the upper state potential has an R^{-3} long range form, whereas the ground state potential has an R^{-6} dependence. In the long range where R is of order 100 Å, the curvature of the ground state potential can be neglected compared to the excited state so that on resonance:

$$hv = \frac{C_3}{R^3} + \frac{C_6}{R^6} \approx \frac{C_3}{R^3} \qquad (5.21)$$

From this equation we see that the internuclear separation where a transition is resonant, known as the Condon point R_c, is given by:

$$R_c = \left(\frac{C_3}{hv}\right)^{1/3} \qquad (5.22)$$

5.8.1 Selection Rules and Transitions

The standard molecular selection rules can not be applied in PA transitions as the initial and final states correspond to different coupling cases, described by different quantum numbers. Electric dipole transitions still impose the limitation that the angular momentum only changes by one unit, and that this change occurs in the electron orbital degrees of freedom, not the electronic, nuclear spin or rotation of the molecule.

Another limitation on the allowed PA transitions is imposed by a centrifugal potential energy barrier from rotational motion of molecules with $\ell \neq 0$. From a scattering point of view, for a central potential the incoming wave can be expressed as a sum of partial waves ℓ. Some potentials are shown for the lowest few partial waves in Figure 5.6. Partial waves which cannot tunnel through the barrier are scattered and do not interact, limiting the collisions in the MOT to s-wave ($l = 0$) and p-wave ($l = 1$) interactions.

5.8.2 Franck-Condon Principle and Transition Rates

The PA process is the coupling of a scattering state to a bound state. The bound state is viewed as a quasi-bound level embedded in a continuum of free scattering states.
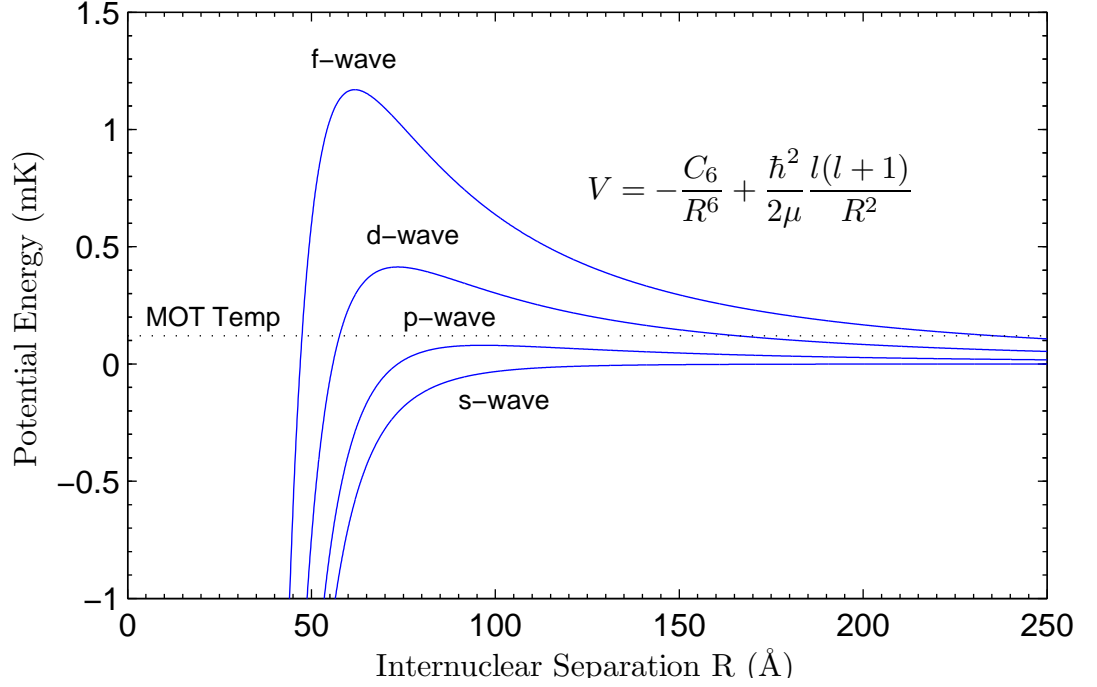
Fig. 5.6: The long range Van der Waals potential for s, p, d and f partial waves of ^{87}Rb. The dotted line is the collisional energy in the MOT.

In this approach proposed by Thorshiem *et al.* [14], and developed by others [68] [69], the strength of the optical coupling between the bound state $|b\rangle$ and the collision state $|E, l\rangle$ at energy E, with partial wave l, is determined by the matrix element:

$$V_b(E, l) = \left(\frac{2\pi I}{c}\right)^{1/2} \langle b | \vec{d}.\vec{e} | E, l \rangle \tag{5.23}$$

where $\vec{e}$ is the polarisation vector of the photoassociation light with intensity I, and $\vec{d}$ is the R-dependent molecular electric dipole moment. A rigorous quantum treatment requires consideration of the ground state quantum numbers $|f_1, m_{f_1}, f_2, m_{f_2}, l, m_l\rangle$ the appropriate (R-dependent) excited state quantum numbers and the polarisation $\vec{e}$.

A simplified two state model gives the transition rate $\Gamma_b(E, l)$ in terms of the matrix element defined above [59]:

$$\hbar\Gamma_b(E,l) = 2\pi|V_b(E,l)|^2. \tag{5.24}$$

The major contribution to the matrix element in Equation 5.23 comes from regions near the Condon point R_c, where the difference between the ground and excited state potentials is equal to the photon energy $h\nu$. When the upper potential is governed by an R^{-3} dependence, and the ground state by an R^{-6} dependence, the Condon point is the classical outer turning point of the excited state vibration R_{v+}.

The stationary phase approximation assumes the electric dipole operator $\vec{d}$ is a slowly varying function around the Condon point R_c. The stimulated decay rate Γ_b takes a simplified form:

$$\hbar\Gamma_b(E,l) = 2\pi|V_c|^2|\langle b|E,l\rangle|^2 \tag{5.25}$$

where V_C is evaluated at R_c. In the reflection approximation the Franck Condon factor $|\langle b|E,l\rangle|^2$ is [70]:

$$|\langle b|E,l\rangle|^2 = \frac{\partial E_b}{\partial b}\frac{1}{|D_c|}|f_l(R_c,E)|^2 \tag{5.26}$$

where $\partial E/\partial b$ is the interval between excited state vibrational levels b at energy E_b, (inverse density of states), D_c is the derivative with respect to R of the difference between the excited and ground state potentials at R_c and $f_l(R_c,E)$ is the wave function for the ground-state partial-wave l at the Condon point. In this approximation the line strength of the transition is determined by the scattering wavefunction.

Figure 5.7 shows the scattering wavefunction calculated for the ground state singlet potential and bound states of the ^{87}Rb upper 0_g^- potential under our experimental conditions. In this case the line strength is strongest at internuclear separations of approximately 100 Åwhere there is strong Franck-Condon overlap between upper bound

levels and the scattering wavefunction. The last node in the scattering wavefunction is around 45 Åfor the singlet state and 53 Åfor the triplet state. This corresponds to a PA detuning of -7.1 cm^{-1} and -4.4 cm^{-1}, respectively, from the 5s+5p$_{3/2}$ limit.
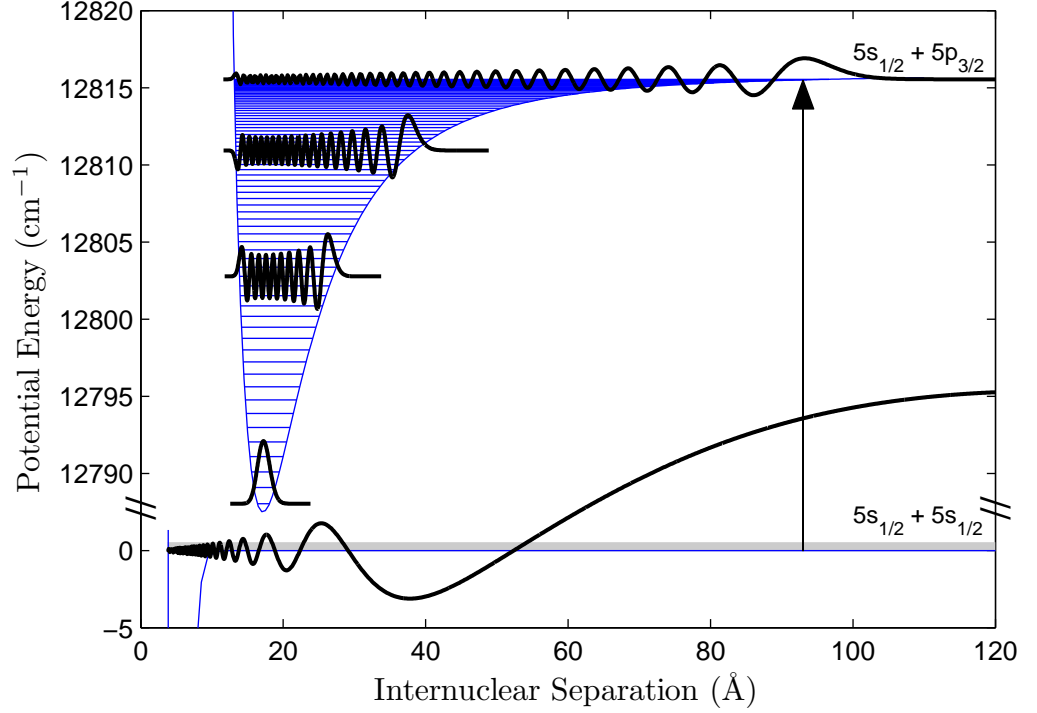
Fig. 5.7: Schematic of some bound wavefunctions in an upper 0_g^- state, and the scattering wavefunction of 120 μK atoms for ^{87}Rb. The Franck-Condon principle suggests transitions occur where there is greatest overlap between the scattering wavefunction and the bound upper state wavefunctions, indicated in this diagram with an arrow.

Chapter 6

Production and Detection of Cold Molecules

> "Almost every molecular constant derived from frequency domain rotational-vibrational-electronic spectra is expressed in cm^{-1} units and referred to interchangeably as an energy, a frequency or a wavenumber. We will follow that dubious but time honoured tradition"
>
> — Helene Lefebvre-Brion and Robert W. Field *The Spectra and Dynamics of Diatomic Molecules*

6.1 Review of Previous Work

Photoassociation spectroscopy has now been performed on a range of alkalis (e.g. Li), alkaline earths (e.g. Ca), noble gases (e.g. He) and mixed species (e.g. K-Rb). The field has recently been comprehensively reviewed with a strong theoretical emphasis [59]. There are also some older experimentally oriented reviews with a more specific focus on Na [71], K [72] and Cs [73]. A brief review of published photoassociation work on Rb is presented below.

Pioneering PA experiments in Rb were performed in a far off resonant dipole trap by Heinzen and co-workers in the early nineties. Trap-loss spectroscopy was performed over 30 cm^{-1} below the ^{85}Rb 5p$_{3/2}$ limit and the 0_g^-, 1_u and 0_u^+ series were observed and spectroscopic coefficients extracted [74].

In 1996 a time-dependent measurement of a cold collision was reported. The time to tunnel through a g-wave shape resonance potential barrier was used to determine the resonance energy [75].

In 2000 the purely long range 0_g^- states were detected for both Rb isotopes below the 5p$_{3/2}$ atomic level. PA spectroscopy was performed in a MOT, and molecular states detected by photo-ionisation [30]. The ^{87}Rb 0_g^- potential was analysed and found to be similar to the ^{85}Rb potential measured in the earlier trap-loss experiments [76].

In 2004 states within 0.4 cm^{-1} of the ^{87}Rb 5p$_{3/2}$ limit were recorded by trap-loss and ionisation detection techniques [28]. In this long-range region of the potential, close to atomic resonance, electrostatic and exchange energies are negligible and hyperfine effects determine the electronic potentials. Two series were identified, and the hyperfine quantum numbers and C_3 parameters were extracted.

In 2006 a Lu-Fano approach was combined with the improved LeRoy-Bernstein model to analyse the ^{87}Rb 0_g^- state in the range 12.5 cm^{-1}-1.5 cm^{-1} below the 5s$_{1/2}$+5p$_{1/2}$ atomic resonance [77]. The phase shift of the wave-function at the dissociation limit was extracted.

In 2006 trap-loss PA spectroscopic data were collected on the 0_u^+ potential below the ^{85}Rb 5s+5p$_{1/2}$ atomic limit. This was combined with previously published trap-loss PA spectroscopic data below the 5s+5p$_{3/2}$ atomic state taken from a dipole trap, and was combined in a fit to potentials and spin-orbit functions to derive an improved C_3 coefficient [78].

In 2006 the upper vibrational levels of the X$^1\Sigma_g^+$ ground state of ^{85}Rb$_2$ were investigated. Molecules were formed by PA in a MOT and after spontaneous decay to

the ground state were ionised by resonance-enhanced two-photon ionisation (RE2PI). By varying the ionisation frequency, vibrational levels were assigned for the ground state and for the $2^1\Sigma_u^+$ intermediate potential used in the RE2PI process [79].

In 2006 experimental spectra and theoretical interpretation of RE2PI of ultracold Rb_2 formed in a magneto-optical trap by photoassociation followed by radiative decay into the $a^3\Sigma_u^+$ lowest triplet state were presented [80]. Some vibrational levels of the triplet ground states and intermediate states were assigned and the corresponding potentials were investigated.

The work presented here builds on previous measurements in the Rb_2 system. This thesis presents the most complete measurements of the two atomic systems under the same experimental conditions allowing isotopic comparisons over a wide range of detuning and internuclear separation. The spectroscopic energy range covered includes regions dominated by the hyperfine, the fine and the Van Der Walls interaction.

6.2   Photoassociation Light

The photoassociation light used in these experiments comes from a solid-state (Ti:Saph) ring laser (Coherent 899) pumped by a 10 W frequency doubled solid state laser (Millennia.) The output power is typically 700 mW single mode, with a line-width of order 1 MHz. The laser is locked to a cavity and can be scanned up to 30 GHz mode-hop free.

The optical setup is depicted in Figure 2.6. A portion of the PA beam is picked off for diagnostics, including a saturated absorption experiment for an accurate measurement of atomic resonance, a Fabry-Perot spectral analyser, a wavemeter and a photodiode to monitor power.

6.2.1 PA Intensity

The PA light is focussed onto the atoms using a single 750 mm focal length lens. The 870 μm 1/e beam waist is overlapped with the trapped atoms which are confined in the MOT with a 1100 μm 1/e cloud width. The photoassociation beam is retroreflected to balance the radiation pressure from the near resonant light, which tends to drive atoms from the centre of the MOT. After the first pass, the slightly divergent light is not collimated or refocussed, so that the beam waist has expanded to 950 μm on the second pass of the MOT. After retro-reflection the peak PA intensity available at the MOT is of order 100 W/cm^2. The beam waist profile is measured using a razor blade on a translation stage and a power meter.
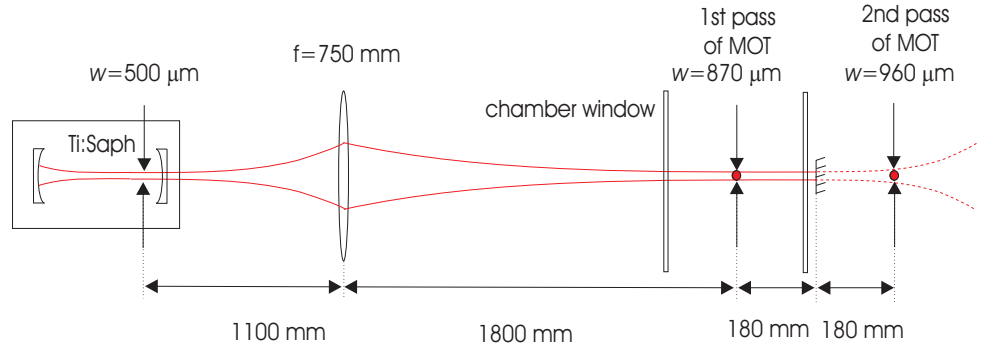
Fig. 6.1: Focussing of photo-association laser

6.2.2 Frequency Diagnostics

The PA frequency is measured with a Burleigh WA-1500 wavemeter. The absolute uncertainty of the measurement is limited by the resolution of the He-Ne reference which is calibrated to an accuracy better than ± 50 MHz [81]. The output of the wavemeter is continuously recorded by a 12-bit National Instruments voltage input card controlled by a LabView interface. The finite update rate (1 Hz) of the wavemeter output limits the resolution of the continuous measurement process. For a typical

continuous scan (25 GHz in 360 s) the laser wavelength has changed by 70 MHz, during the time it takes to complete one measurement. The resulting measurement of wavelength versus time is a staircase function, with steps of 70 MHz/s.

Wavelengths are interpolated from the staircase function using a least squares linear fit. This provides an averaging of the wavelength measurements as well as an interpolation between discretisation from the finite sample time (70 MHz), digital output of the wavemeter output (20 MHz at the highest resolution) and redigitisation of the data for storage (40 MHz at highest resolution setting).

The residuals from the linear fit exhibit a correlation over 1 s as expected due to the finite measurement time. Examination of the signal within a single (1 s) sample reveals that sources of (white) noise are modest compared to the digitisation errors. A long range systematic variation in the residuals indicates a slight nonlinearity in the wavelength scan.

The systematic shift due to the finite update time of the wavemeter was compensated by calibrating the wavemeter with the same scanning conditions as used in the experiments. The calibration was performed using the ^{85}Rb and ^{87}Rb $5s_{1/2} \rightarrow 5p_{1/2}$ and $5s_{1/2} \rightarrow 5p_{3/2}$ atomic hyperfine transitions from a vapour-cell saturated-absorption experiment.

The uncertainty in the measured wavelength is approximately ± 35 MHz, comparable to the systematic calibration uncertainty ± 50 MHz. The final frequency determination uncertainty is $\pm$ 61 MHz.

6.2.3   Detection Techniques

The implementation of fluorescence and ionisation detection systems are described in previous chapters. Schematics of trap-loss and molecular ionisation processes are shown in Figure 6.2. Initially free atoms undergo PA to an excited state attractive

potential. In the limit of well resolved photo-association lines, the vibrational period of the excited molecule is much shorter than the spontaneous lifetime. The molecule can then decay into the ground electronic state of opposite parity (gerade singlet or ungerade triplet) or into unbound atoms [82]. The decay path is determined by the Franck-Condon factors between the initial and corresponding final states.

When unbound atoms result from the spontaneous decay, those free atoms carry away the kinetic energy δE gained from their interaction. When this corresponds to a velocity greater than the escape velocity of the trap, the free atoms are lost from the trap. The escape velocity of the trap is the velocity required to leave the trap from the trap center, and is therefore less than the capture velocity $V_c = 30\ m/s$ discussed in Section 2.2.2. Trap-loss measurements infer the PA of two atoms into a molecule by the resonantly induced two-body loss-rate in the atomic fluorescence.

When a bound electronic ground-state molecule results from the spontaneous emission, the molecule is formed with translational energy close to the (119 μK) temperature of the free atoms [30]. When sufficiently bound these molecules are no longer resonant with the trap light, and are not magnetically trapped by the field gradients used in the MOT. The molecules will leave the trapping region due their ballistic expansion in a time of order 20 ms. An ionisation laser is tuned to resonance with the ground state molecular decay product. The ground state molecules undergo REMPI through an intermediate state, and form Rb_2^+, which is detected by its time of flight on the CEM.

6.3   Ionisation Detection of Molecules

During the normal operation of the MOT, with no PA laser, we observe a strong molecular ion signal for ^{85}Rb, and a very weak one for ^{87}Rb. This is consistent with other experiments which have reported a strong ^{85}Rb$_2$ signal and no ^{87}Rb$_2$ signal from a MOT [30] and a strong ^{85}Rb$_2$ signal and a weaker ^{87}Rb$_2$ signal [28].
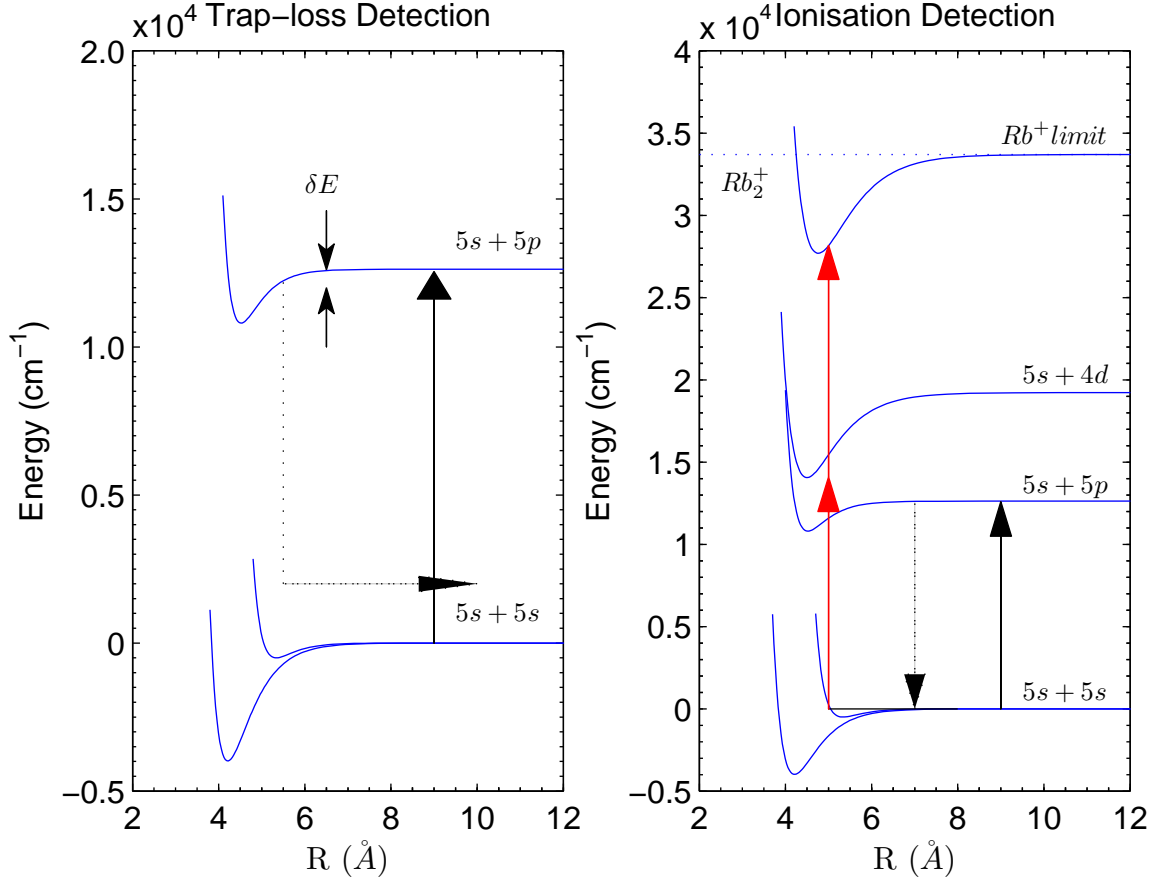
Fig. 6.2: The trap-loss diagram shows the absorption of a photoassociation photon; the atoms then accelerate towards each other gaining kinetic energy δE, before spontaneous emission. Spontaneous emission, indicated by the dashed arrow, occurs predominantly to unbound atoms. When $\delta E >$ MOT trap depth the free atoms are lost from the trap. The ionisation diagram shows spontaneous emission to a bound state, then a resonant two-photon absorption process through a bound molecular state to a Rb_2^+ potential.

The most likely explanation for this isotopic difference is that the molecules are being formed by PA from the trapping light. The trapping light for both isotopes is 12 MHz detuned, which may correspond to a node in the scattering function for ^{87}Rb. All of the following ionisation data were taken in ^{87}Rb to take advantage of the smaller molecular ion background signal from the trapping light.

We implemented REMPI to detect molecules formed by PA. A low resolution REMPI spectrum spanning the whole optical spectrum (400 nm-700 nm) was used to find

suitable frequencies for the detection of the molecules. In Figure 6.3 the ionisation laser was scanned from 14,250 - 20,000 cm^{-1} while the atomic and molecular ion signals were recorded simultaneously on separate boxcar modules. At energies above the $5p_{3/2} \rightarrow \underset{n\to\infty}{lim} nl$ one-photon limit at 20,877 cm^{-1}, a strong background of atomic and molecular ion signals makes individual levels difficult to identify.

The largest feature in the spectrum, at 15,351.5 cm^{-1}, is a spurious signal arising from leakage ($< 1\%$) of idler light from the MOPO that is resonant with the $5p_{3/2} \rightarrow 5d \rightarrow Rb^+$ transition. The ionisation light arises from non-linear parametric down-conversion of 28,195 cm^{-1} pump light, the third harmonic of a Nd:YAG laser. When the ionising laser is tuned to 15,351.5 cm^{-1}, idler light at 12,844 cm^{-1} is produced which is responsible for the spurious feature. This signal disappeared when a narrow-band interference filter transmitting around 15,351.5 cm^{-1} was placed before the sample.

The trap-loss spectrum shows a number of dips for the $5p_{3/2} \rightarrow nd$ series, which efficiently depletes the number of trapped atoms. Transitions from the 5s state do not appear in the trap-loss spectrum. Trap-loss can arise from both atomic ionisation depletion and molecule formation processes, with the atomic and molecular ion signals both consistent with the trap-loss signals.

The atomic ion signal arises when atoms, initially cycling between the 5s and $5p_{3/2}$ states, absorb photons from the ionising laser and are excited above the ionisation threshold (33,690.8 cm^{-1}) [83]. The atomic signal is dominated by REMPI transitions through intermediate dipole and quadrupole allowed transitions ($5s \rightarrow np$, nd and $5p_{3/2} \rightarrow ns$, np, nd, nf). Two photon dipole allowed transitions such as $5s \rightarrow ns$ are also observed.

These experiments were performed in the presence of a 29 V/cm electric field, at higher n stark mixing may lead to a relaxing of the selection rules. However all of the transitions identified here are single or two photon dipole or quadrapole allowed transitions.

The molecular spectrum is dominated by the spurious $5p_{3/2}$ $\rightarrow$5d$\rightarrow$Rb$^+$ transition discussed above, and by the $5p_{3/2}\rightarrow n$s, nd atomic transitions to (high n states) also spuriously detected as molecules in the TOF system due to their long lifetimes, as discussed in Section 4.5.1. There is also a strong molecular signal between the 14,000 - 15,000 cm^{-1} and 16,000 - 18,000 cm^{-1} intervals.

When the ionisation laser is tuned below 16,845.4 cm^{-1}, atoms initially in either the 5s or $5p_{3/2}$ state require a three-photon absorption process to reach the ionisation threshold. Below this three-photon threshold is the most suitable place to detect molecules, as the atomic ion signal is small, the trap is unperturbed and the molecular signal is strong. It is in this region that we fix the ionisation laser wavelength to collect PA spectra, at 16,583 cm^{-1}.

6.4 Spectroscopy of Excited Molecular Potentials

After PA to an excited molecular potential, spontaneous decay into bound states favours high lying closely spaced vibrational levels of the electronic ground state potentials [76] [79]. Bound-bound molecular spectroscopy of excited molecular potentials is performed on these decay products. Scanning the photo-ionisation (PI) laser frequency gives information on the intermediate states in the RE2PI spectrum. This is combined with the initial narrow energy distribution of vibrational levels and the final ionisation step, which has a smooth frequency dependence above the atomic ionisation threshold.

RE2PI detection of molecules following spontaneous decay into the $a^3\Sigma_u^+$ has been observed by other groups for ^{87}Rb$_2$ and ^{85}Rb$_2$ dimers [76] [28]. Intermediate states were identified as $(2)^3\Pi_g$ and $(2)^3\Sigma_g^+$ states, consistent with assignments by other groups [80]. Spectroscopy of the intermediate excited molecular states is presented here for a ^{87}Rb MOT over a large energy range. Figure 6.3 shows a molecular ion spectrum spanning most of the optical spectrum, with insufficient resolution to assign
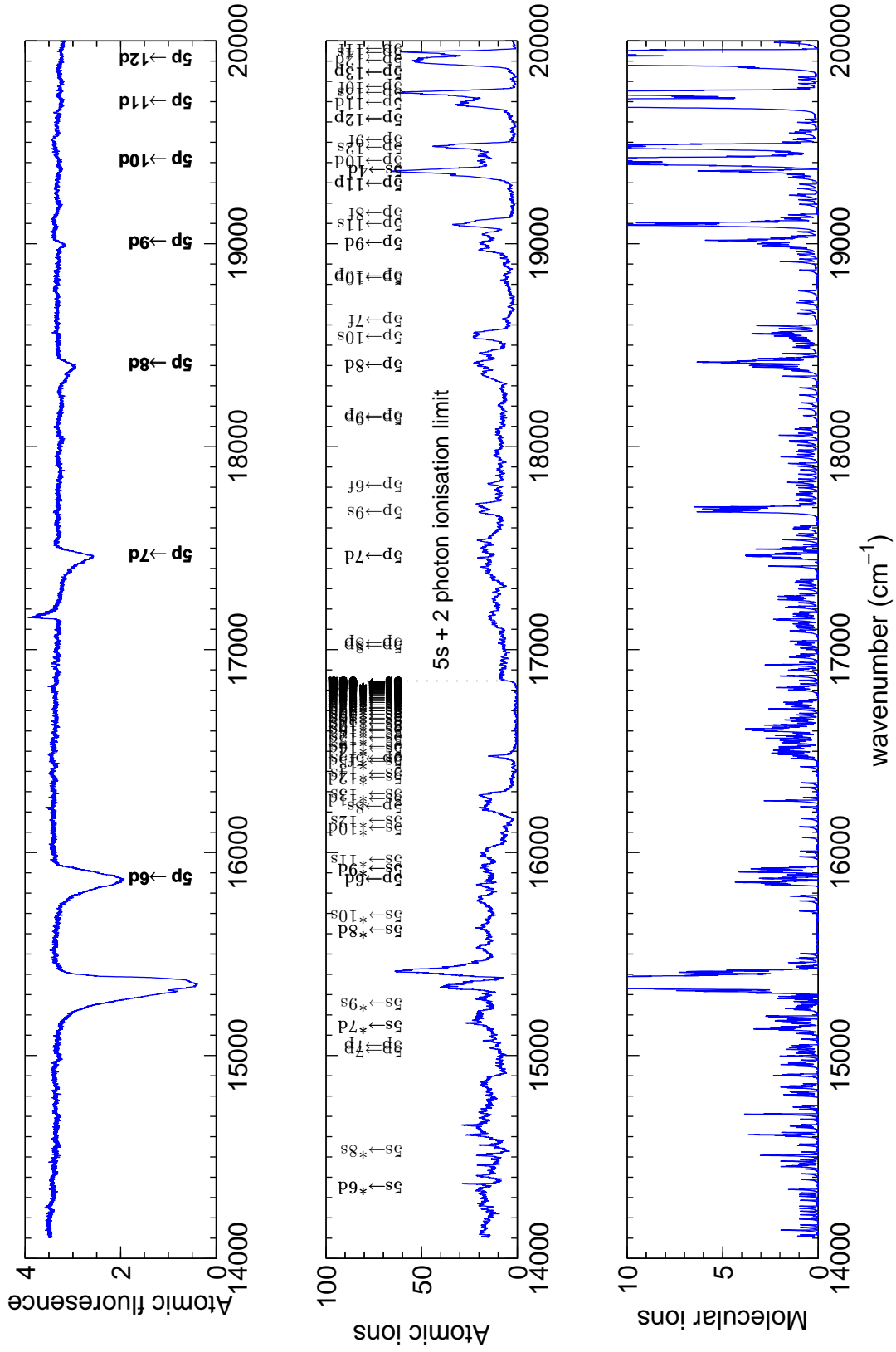
Fig. 6.3: Trap-loss spectrum, atomic ion and molecular ion spectrum showing intermediate states in a RE2PI process. Transitions identified with an asterix are two photon dipole-allowed transitions rather than single photon quadrupole-allowed transitions. Overlapping labels show non resolved levels at the ionisation limit.

individual vibrational levels.

To record bound-bound spectra the PA laser was tuned 2.14 cm^{-1} below the 5s+5p$_{3/2}$ limit, resonant with the $|0_g^-, v = 51\rangle$ state shown in Figure 6.5. This state decays to upper vibrational levels of the ungerade triplet ground state $a^3\Sigma_u^+$. For single photon transitions the relevant bound transition selection rules are $\Delta\Omega=0, \pm1, \Delta S = 0$, $\Delta p = 1$ (where p is the parity of the molecule) and that the reflexion symmetry is unchanged. The allowed electronic transitions from the ground state are $a^3\Sigma_u^+ \to {}^3\Pi_g$, ${}^3\Sigma_g^+$. Figure 6.4 shows the intermediate potentials which are involved over the energy range shown in Figure 6.3. These potentials, taken from the literature, are generated with effective core pseudo-potential calculations [58].
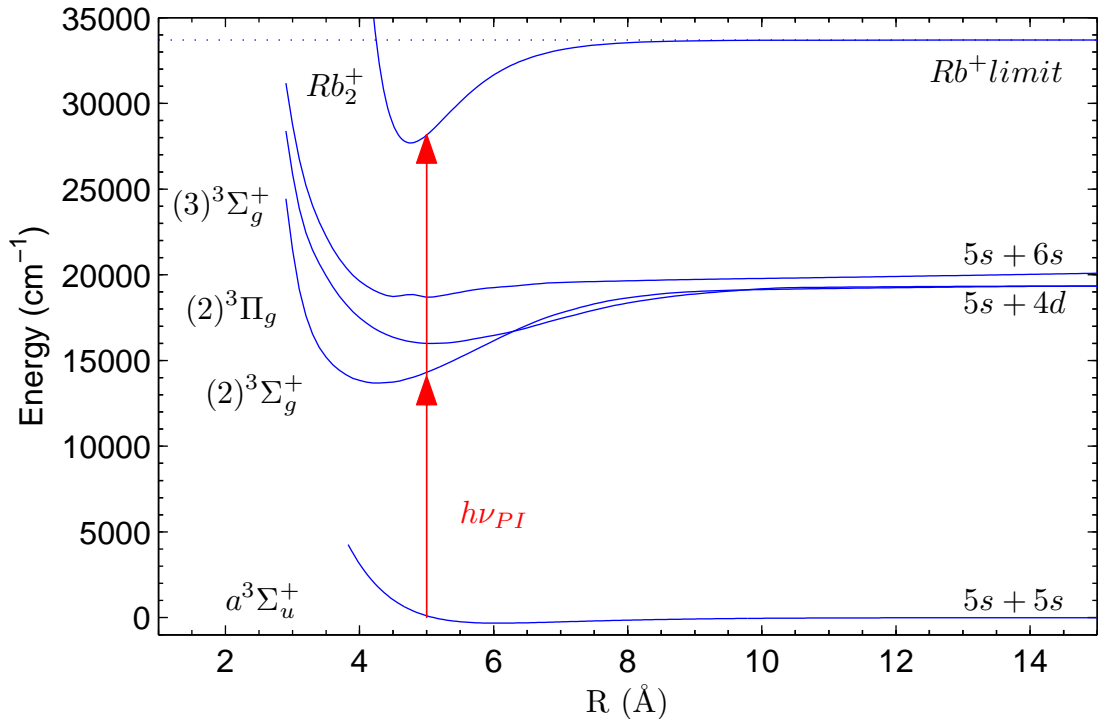
Fig. 6.4: Molecular potentials [58] involved in the ionisation process.

The PI laser scan is linear in wavelength, with the calibration performed using the labelled atomic transitions. The molecular ion signal is strong around 14,000

- 15,000 cm^{-1}, at the bottom of the $(2)^3\Sigma_g^+$ (5s+4d) well, and around 16,500 - 18,000 cm^{-1} near the bottom of the $(2)^3\Pi_g$(5s+4d) well. Above the 5s+4d limit (19361 cm^{-1}) there is a strong ion signal due to atomic transitions to long lived states in addition to the molecular ion signal from the $(3)^3\Sigma_g^+$(5s+6s) intermediate electronic state.

The ion signal is complicated by the occupation of multiple vibrational levels in the lower state, and excitation to multiple vibrational levels in the upper state. At the current resolution, vibrational progression can not be assigned. Higher resolution measurements can be achieved by further detuning the PA laser, so that fewer, more deeply bound and less closely spaced vibrational states are accessed in the ground state. The scan rate of the laser can also be slowed down, to the lower limit of 0.001 nm increments. The Σ states should exhibit simpler spectra as there is no spin-orbit coupling of the potential. The signal can also be improved at higher intensities, which is currently limited by the mode structure of the laser and the damage threshold of the optical fibre.

6.5 Ionisation Detection of PA Products

Ionisation of molecules in the a$^3\Sigma_u^+$ state was employed as a detection mechanism for PA spectroscopy of excited state molecular potentials below the 5s+5p$_{3/2}$ limit. Standard molecule selection rules do not apply to the PA process, as the initial ensemble of scattering states does not have a well defined parity. The subsequent spontaneous decay, and RE2PI bound-bound detection process following PA, obeys the usual molecular selection rules as both the initial and final states are in well defined electronic states.

A PA spectrum has been published in which 0_g^- states asymptoting to the 5s+5p$_{3/2}$ limit of ^{87}Rb$_2$ were detected using RE2PI after decaying to the ungerade triplet ground state a$^3\Sigma_u^+$ [76]. The detection process employed a gerade state assigned as the $2^3\Pi_g$

state asymptoting to the 4d+5s state.

In this work the ionisation laser was fixed to the RE2PI peak at 16,597 cm^{-1} near the bottom of the $(2)^3\Pi_g$ well. The PA laser was scanned below the 5s+5p$_{3/2}$ limit and excited state molecules were detected after spontaneously decaying into triplet ground state molecules. Only gerade states should decay into the triplet ground state. The 0_g^- series was identified in the ion spectrum; however the 1_g states were not detected in these measurements. The 0_g^- state has higher Franck-Condon overlap with the ground state, due its long range inner and outer turning point.

The state selectivity of ionisation measurements is useful in conjunction with trap-loss measurements for the assignment of electronic states. Figure 6.5 shows some combined trap-loss and ionisation data. The periodic vibrational progression of the 0_g^- states is readily identifiable in the ion spectrum. The trap-loss spectrum contains additional peaks from the 0_u^+ and 1_g series. The 0_g^- trap-loss features can be identified as they are coincident with the ion peaks. The 0_u^+ and 1_g series are overlapping and cannot be assigned from the trap-loss spectra in this part of the spectrum.

6.6 Fluorescence as a Measure of Trap-loss

The number of atoms in the MOT is governed by Equation 2.11. When the PA laser is scanned through a resonance, the rate of trap loss through two-body collisions changes. It takes minutes (τ=35 s) for the competing processes of trap-loss and trap loading to equilibrate.

Trap-loss features are in the order of 10 MHz wide. Scanning the PA laser frequency over 30 cm^{-1} sufficiently slowly for the atom number to equilibrate every MHz would take two years of continuous data collection. In practice the PA laser is scanned much faster (60 MHz/s), and the non-equilibrium atom number is recorded.

Figure 6.6(a) shows a typical scan over a trap-loss feature. Heating due to off-resonant
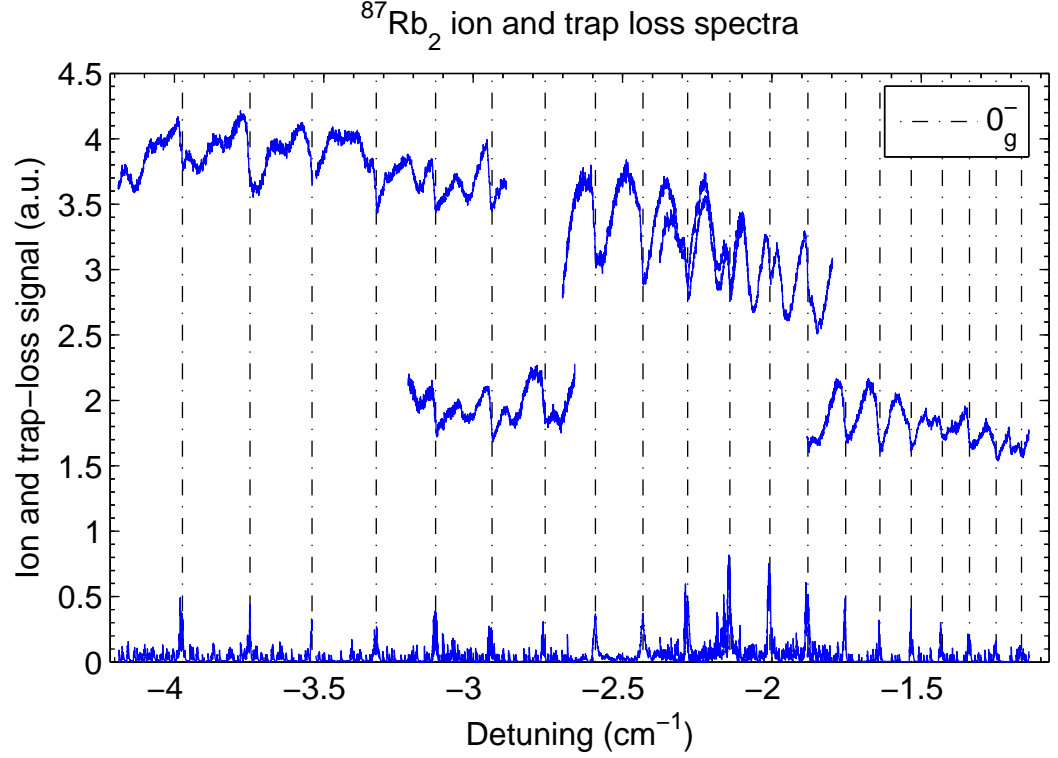
Fig. 6.5: $^{87}\text{Rb}_2$ molecular ion and trap-loss PAS, detuned from the $5s+5p_{3/2}$ limit.

excitation was negligible, as the trap was unperturbed by the 5 cm^{-1} detuned laser far from any PA resonance. At the bottom of the trap-loss dip about 20% of atoms are lost with 5×10^6 atoms remaining. Figures 6.6 (**x**), (**y**) and (**z**) show trap loading curves with the PA laser frequency fixed at various points on the trap-loss peak. For small two-body loss rates a measure of the rate C can be obtained by fitting the atom loading equations of Section 2.3.2 to these curves. For larger losses the fit is poor, since the trap volume changes significantly. However in this regime the trap loading rate A is still constant and the background collisional loss is negligible; so loss rate B proportional to the number of atoms in the trap can be attributed to the PA loss rate. In Figure 6.6 (**x**), (**y**) and (**z**) correspond to a loss rate B of 3×10^{-2}, 9×10^{-2} and 1×10^{-1} s^{-1} respectively.
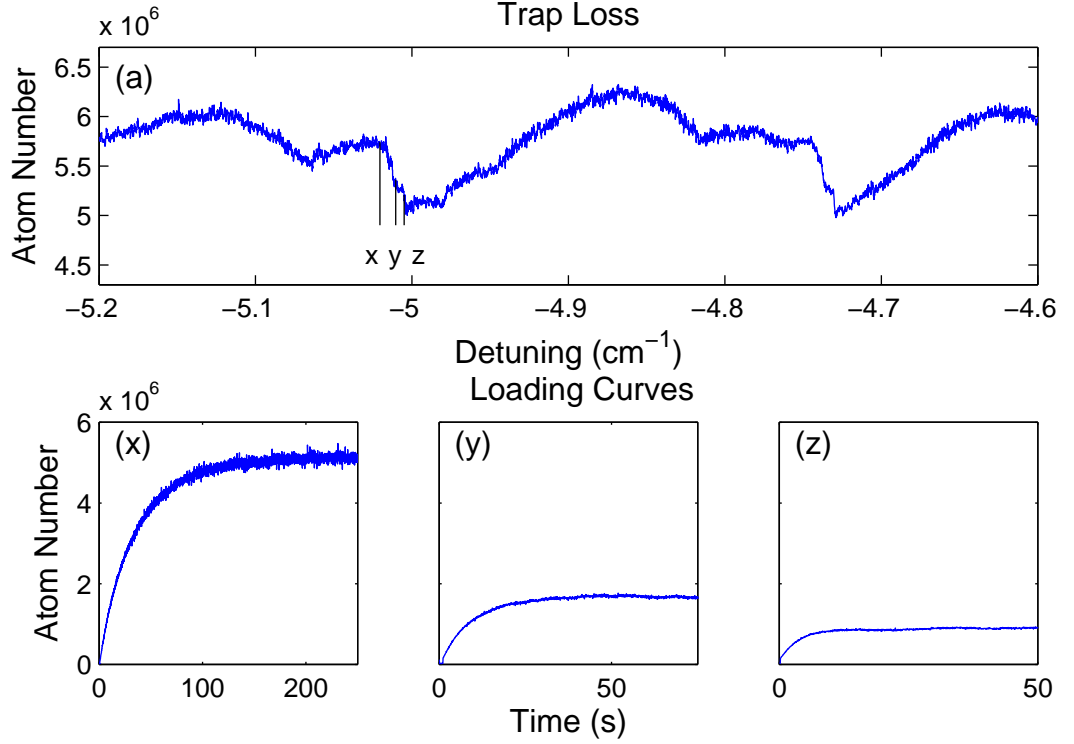
Fig. 6.6: (**a**)Trap-loss spectrum scanning the PA laser at 60 MHz/s. (**x**), (**y**) and (**z**) are loading curves with the PA laser fixed at the indicated frequency. The equilibrium atom number is lower than the non-equilibrium atom number in the trap-loss scan.

6.7 Trap-loss Data

Trap-loss data was recorded over a range of 30 cm^{-1} below the 5s+5p$_{3/2}$ asymptote for both ^{87}Rb and ^{85}Rb in Figures 6.7 and 6.8. The 30 cm^{-1} spectral range for each isotope is made up of approximately 50 separate mode-hop free scans, each spanning approximately 25 GHz. The typical scan rate was 70 MHz/s. The PA laser power at the MOT was increased from <1 mW near resonance to 1 W (including the retroreflected power) at a detuning of 30 cm^{-1}. The fluorescence sample rate was set to the ion sample rate, which is fixed by the 10 Hz repetition rate of the MOPO laser. The resolution of both the fluorescence and ionisation systems, determined by the frequency interval between samples, is 7 MHz which is comparable to the linewidth of the PA laser and the natural line-width of the transitions under investigation. The absolute wavelength

resolution of the system is of order 60 MHz (0.002 cm^{-1}).

Examination of the PA spectra in Figures 6.7 and 6.8 reveals overlapping series of vibrational levels, with each electronic series containing distinct rotational and hyperfine structure. The 0_g^- series shows a purely rotational progression, the 0_u^+ series exhibits pre-dissociation broadening [74], and the 1_g state shows a complicated and barely resolved hyperfine structure. In Figure 5.4 shown earlier, four attractive Movre-Pichler potentials below the 5s+5p$_{3/2}$ asymptote with binding energy greater than 2 cm^{-1} can be identified; these are the 0_g^-, 2_u, 0_u^+ and 1_g states. The 5s+5s+$h\nu$→2_u transition can be ruled out since the single-photon PA transition should provide only one unit of orbital angular momentum.

From Equation 5.13 the LeRoy-Bernstein expression for the vibrational level energy of all potentials below the 5s+5p limit, dominated by the resonant-dipole interaction (n=3), is:

$$v_D - v = \alpha(D_e - E(v))^{1/6} \tag{6.1}$$

where:

$$\alpha = \sqrt{\frac{2\mu}{\pi}} \frac{\Gamma(5/6)}{\Gamma(4/3)} \frac{(-C_3)^{1/3}}{\hbar} \tag{6.2}$$

Once a series of vibrational lines has been identified as belonging to a single electronic state, either by line-strength, line-shape or energy spacing, the relative vibrational numbers can be assigned. As a consequence of the v_D term in the LeRoy-Bernstein formula arbitrary relative vibrational assignments can be made without *a priori* knowledge of the absolute vibrational assignment relative to either the dissociation limit or the bottom of the potential well. Treating α and v_D as fit parameters, once three or more vibrational assignments have been made in a series, Equation 6.1 predicts the energy of all vibrational levels in the series relative to those already assigned.

A Lu-Fano type plot of (binding energy)$^{1/6}$ against vibrational number, shown below
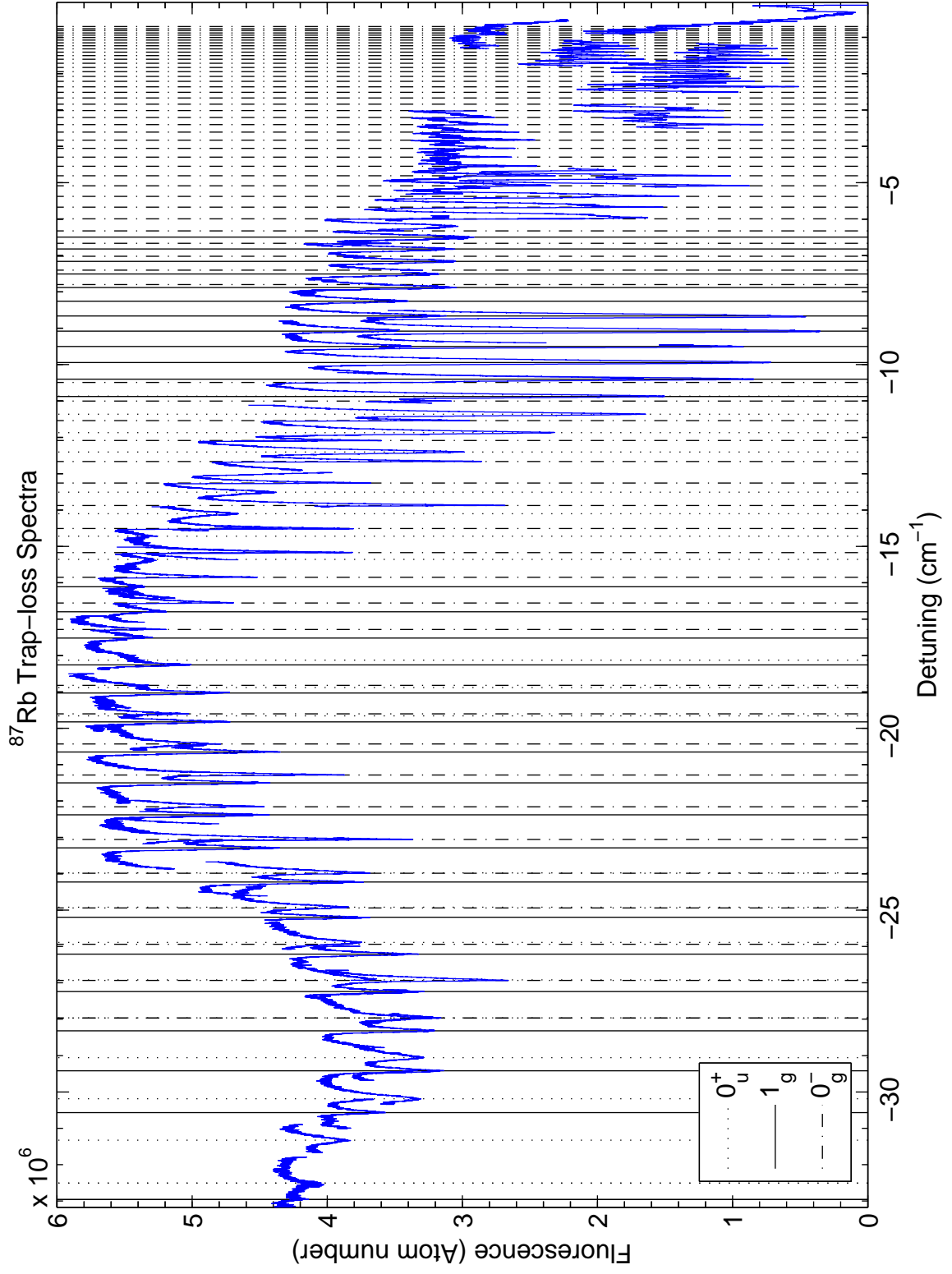
Fig. 6.7: ^{87}Rb Trap-loss data with the PA laser frequency detuned from the $5s_{1/2} \rightarrow 5p_{3/2}$ atomic transition.
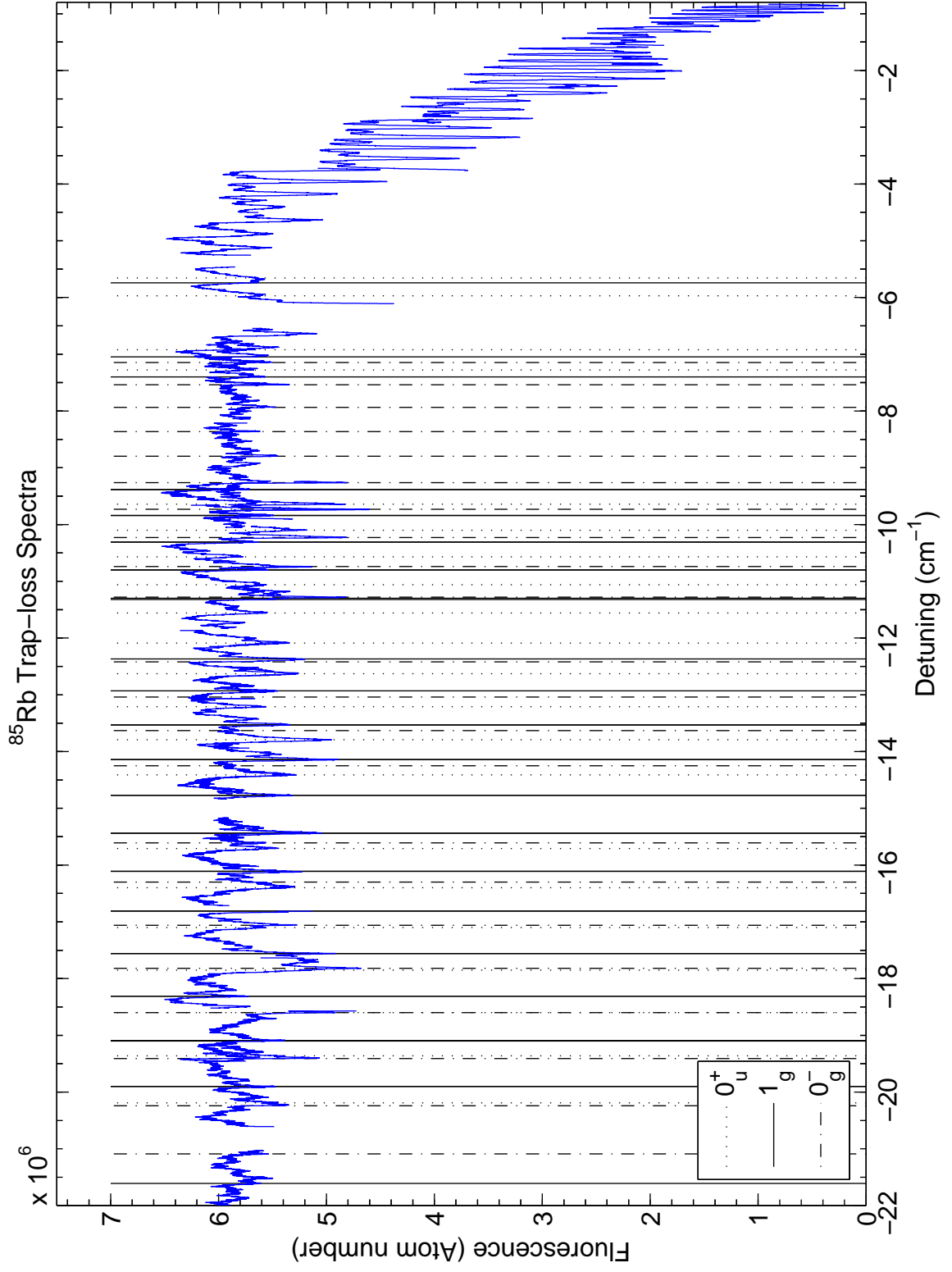
Fig. 6.8: ^{85}Rb Trap-loss data with the PA laser frequency detuned from the $5s_{1/2} \rightarrow 5p_{3/2}$ atomic transition. The baseline has been normalised across different data sets.

for both isotopes in Figures 6.9 and 6.10, is linear in the range where Equation 6.1 is valid. Three separate series can be clearly identified on the plot. The 0_g^- series is readily identified as it only extends to 27.89 cm^{-1} detuning, which is the bottom of the Movre-Pichler 0_g^- well in the potential. The 0_g^- series also exhibits curvature on the Lu-Fano type plot which indicates deviation from a simple $D_e - C_3/R^3$ potential, as is expected since the potential exhibits a potential minimum. The deviation from the LeRoy-Bernstein formula is more easily seen in a plot of residuals on a linear energy scale shown in the insets of Figure 6.11.
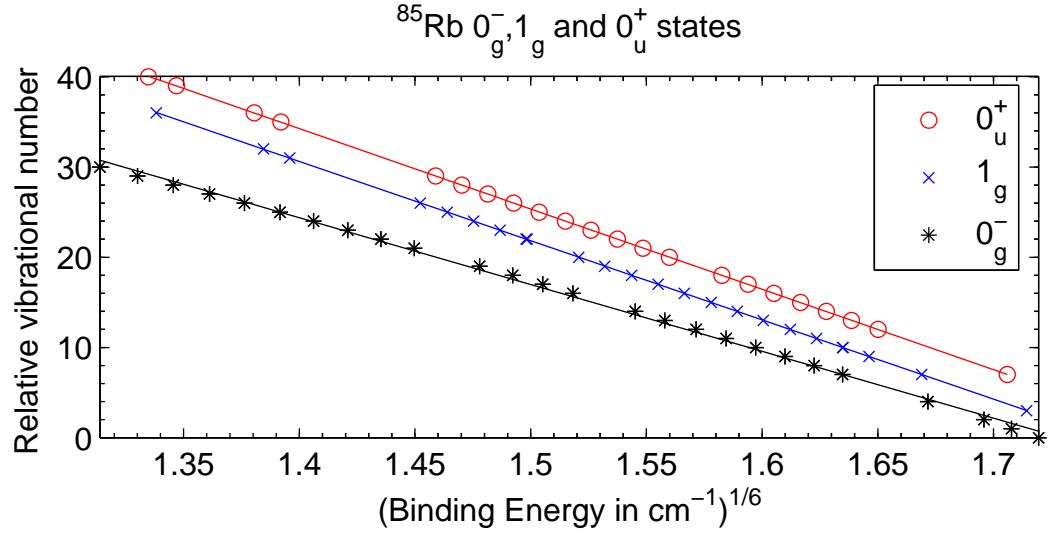
Fig. 6.9: Plot of relative vibrational number against (binding energy)$^{1/6}$ below the ^{85}Rb $5s+5p_{3/2}$ limit, along with lines of best fit. The 0_g^- vibrational assignments are relative to the bottom of the well.

Some overlapping vibrational levels are omitted from the Lu-Fano plots. At large detunings a distinctive, though not well-resolved, rotational and hyperfine structure can be discerned but partially overlapping states closer to resonance are not easily identified from the trap-loss spectrum. Improving the resolution of the trap-loss measurements would allow more levels closer to dissociation to be unambiguously assigned. The ionisation data allows a greater range of vibrational levels of the ^{87}Rb 0_g^- to be assigned close to resonance.
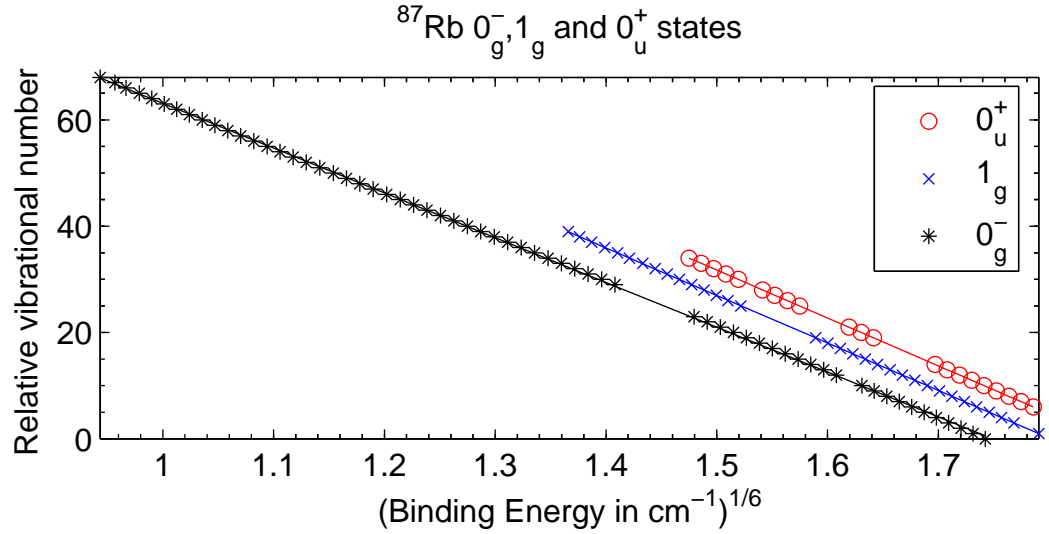
Fig. 6.10: Plot of relative vibrational number against (binding energy)$^{1/6}$ below the ^{87}Rb 5s+5p$_{3/2}$ limit, along with lines of best fit. The 0_g^- vibrational assignments are relative to the bottom of the well. Identification of the ^{87}Rb 0_g^- series was aided by ionisation data.

6.7.1 C_3 Coefficients

From the data in Figures 6.9 and 6.10 the fitted parameters v_D and α can be extracted. In a purely $D_e - C_3/R^3$ potential, α can be related to the resonant-dipole interaction coefficient C_3, the dipole matrix element $\langle 5s|er|5p_j \rangle$ and therefore the 5p$_j$ atomic lifetime.

For real potentials the extracted C_3 coefficients approximate the potentials near the right-hand turning points of the observed vibrational levels. The potential includes contributions from higher order dispersion terms on the upper and lower potentials, exchange energy and relativistic effects such as spin-orbit coupling, hyperfine structure and retardation. Outside the fitted range the shape of the real potentials may deviate drastically from that given by the restricted curvature permitted in Equation 6.1 [28].

The C_3 parameters extracted in the fits presented here exhibit some variation when fitting to different vibrational levels within the same electronic state. This was recognised in the ^{85}Rb assignments [74] by placing a large systematic uncertainty

of ± 0.7 a.u. on the C_3 parameters that were extracted despite the small statistical uncertainty ± 0.02 a.u. which reflects the high resolution of the measurements. The levels closer to dissociation should provide the best approximation to the free atomic parameters [84].

Table 6.1 shows a comparison of ^{85}Rb$_2$ and ^{87}Rb$_2$ C_3 coefficients obtained in this work to comparable work in the literature. The measurements are in agreement, given the systematic error ± 0.7 a.u. which arises from fitting to different vibrational levels within the same electronic series.

Fioretti *et al.* state that the C_3 coefficients of the two Rb isotopes scales as the ratio of the reduced mass of the e-Rb$^+$ system $\rho_{at}^{-6} = [\mu_{at}(^{87}\text{Rb})/\mu_{at}(^{85}\text{Rb})]^6 = 1.000000445$, due to the normalization of s and p atomic wave functions[85]. This is smaller than the experimental resolution; so differences in the C_3 coefficients between the isotopes is indicative of isotope-dependent effects that are not included in the Le-Roy formalism. The effects of channel mixing and R-dependent spin-orbit coupling are likely candidates [86].

Table 6.1: Comparison of C_3 parameters for 0_g^- and 0_u^+ state obtained in this work with those in the literature [74]. C_3 coefficients are expressed in atomic units (1 a.u.= 1 Hartree/Bohr Radius^3). The energy range is below the 5s+5p$_{3/2}$ limit. The first uncertainty is a statistical uncertainty and the second is a systematic uncertainty.

	^{85}Rb Cline [74]	^{85}Rb This work	^{87}Rb This work
Energy range	0-30 cm^{-1}	5-25 cm^{-1}	5-33 cm^{-1}
1_g C_3 coefficient	14.29$\pm$0.02$\pm$0.7	14.34	14.63
0_u^+ C_3 coefficient	14.64$\pm$0.01$\pm$0.7	14.94	14.99

The 0_u^+ and 1_g Hund's case C potentials can be expressed in a Hund's case A basis in a multipolar expansion in $1/R$ [63]:

$$V_{0_u^+} = D_e - \frac{5C_3}{3R^3} + \frac{9A(C_6^\Pi + 2C_6^\Sigma) + 4C_3^2(1+\epsilon)^2}{27AR^6} \tag{6.3}$$

$$V_{1_g} = D_e - \frac{A}{2} - \frac{(\sqrt{7}+2)C_3}{3R^3} + \frac{9A\big(2(\sqrt{7}-1)C_6^\Pi + (2+\sqrt{7})C_6^\Sigma\big) + 2(7\sqrt{7}-10)C_3^2(1+\epsilon)^2}{27\sqrt{7}AR^6}$$

$$(6.4)$$

where A is related to the fine structure splitting, ϵ is a parameter related to retardation, D_e is the "centre of gravity" of the 5p state and Π and Σ are the Born-Oppenheimer potentials below the 5s+5p atomic limit. Neglecting the R^{-6} terms the measured Hund's case C C_3 coefficients can be related to the Born-Oppenheimer resonant-dipole interaction coefficient. The values in Table 6.2 are extracted from the experimental values in Table 6.1 and Equations 6.4 and 6.3. This allows a comparison between different electronic series in addition to a comparison between the isotopes.

Table 6.2: Comparison of Hund's basis A Π C_3 parameters from the states in this work with those in the literature [74]. C_3 coefficients are expressed in atomic units (1 a.u.= 1 Hartree/Bohr Radius^3).

Source	Resonant dipole C_3 coefficient
^{85}Rb 0_u^+ C_3 this work	8.968
^{87}Rb 0_u^+ C_3 this work	8.994
^{85}Rb 0_u^+ C_3 Cline [74]	8.784
^{85}Rb 1_g C_3 this work	9.262
^{87}Rb 1_g C_3 this work	9.448
^{85}Rb 1_g C_3 Cline [74]	9.228
Theory Marinescu [87]	9.202
Combined p$_{1/2}$ and p$_{3/2}$ 0_u^+ [78] data	8.903

The Cline data [74] are directly comparable to this work as they were obtained with PA spectroscopy over a comparable energy range, though under different experimental conditions. The Bergeman measurement [78] should be more accurate as it used coupled channel calculations and includes data below the ^{85}Rb 5p$_{3/2}$ and 5p$_{1/2}$ atomic limits. The differences in the coefficients is, in part, due to the different vibrational levels used in each fit. This behaviour is beyond the simplified LeRoy formalism. A qualitative description of the effects which will need to be included in a more complete model follows below.

6.7.2 Beyond the LeRoy Formalism

Fits to the LeRoy-Bernstein equation for all of the potentials considered here are shown in Figures 6.12 and 6.11. The deviation from the LeRoy-Bernstein fit are shown in the insets. The large residuals for the 0_g^- fit shows that the C_3 behaviour of this purely long range state is only valid at very long range. The residuals for the 1_g and 0_u^+ states are much smaller; however there is evidence in the residuals for the 1_g states of a periodic perturbation. The levels overlap around 15 cm^{-1} detuning, and this may be perturbing the energy assignments. However some of the deviation is expected to arise from perturbations from the oversimplified model.

Bergeman *et al.* showed that coupled channel calculations, including R-dependent spin-orbit coupling, significantly reduced the residuals to fits of the 0_u^+ series beneath both the 5p$_{3/2}$ and 5p$_{1/2}$ atomic limits [78]. The Leroy-Bernstein formalism employed in this thesis only allows for a fixed asymptotic value of the fine-structure splitting. Pre-dissociation broadening of the 0_u^+ has been observed, and there may also be a significant effect from pre-dissociation shifting of the levels [88]. A more complete analysis of the molecular potentials will also include the hyperfine interaction for levels closer to resonance.

The line strengths of the transitions also show an isotopic dependence. The modulation of the transition strengths is dependent on the Franck-Condon overlap of the scattering wavefunction and the bound wavefunctions. The PA spectra are rich in information that has not been extracted in this thesis.
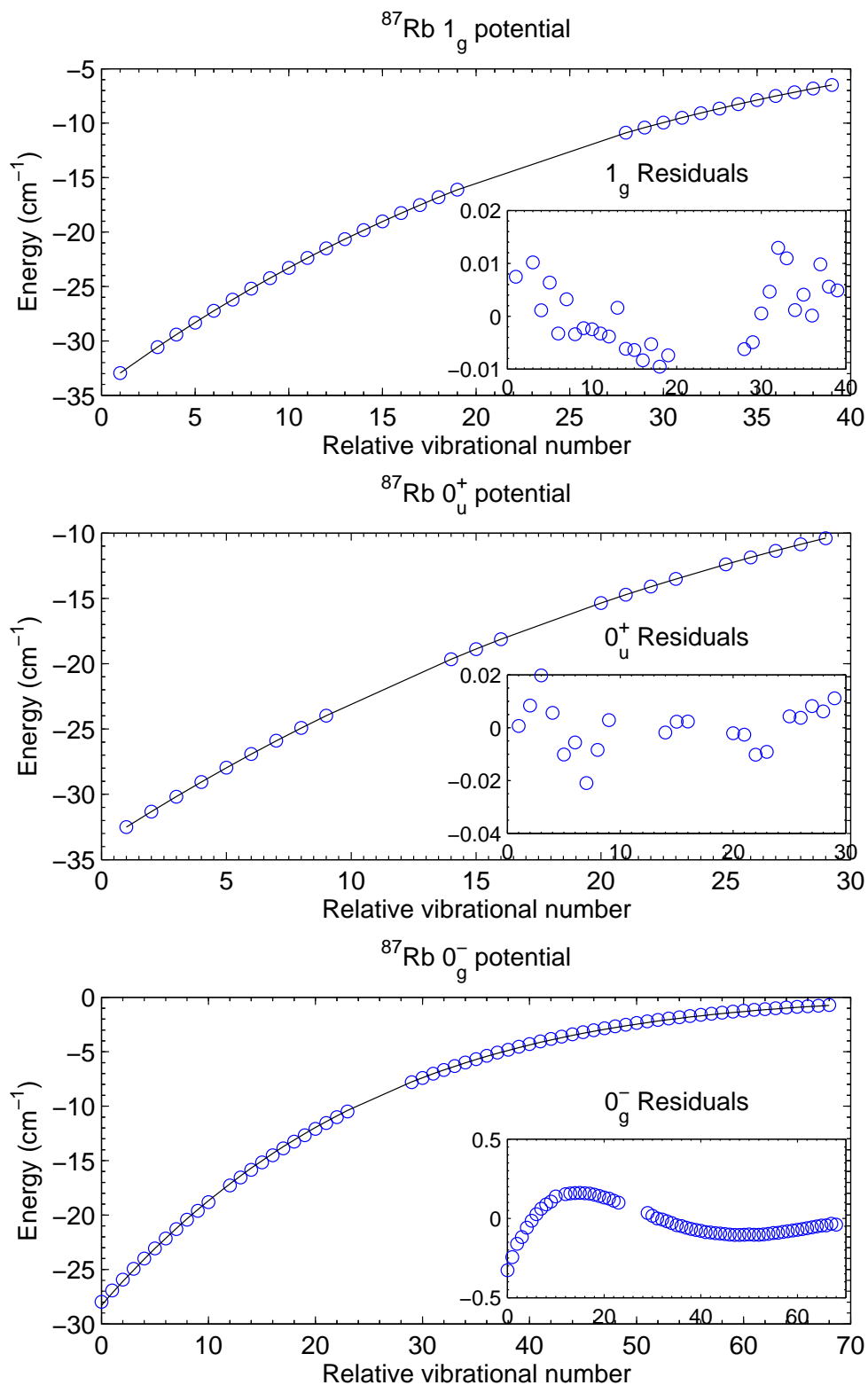
Fig. 6.11: Plot of level energy against vibrational number for the $^{87}Rb_2$ 0_g^-, 0_u^+ and 1_g potentials. Vibrational assignments are relative to the bottom of the well for the 0_g^- state. The fitted line is Equation 6.1. The residuals of the fit are shown in the inset.
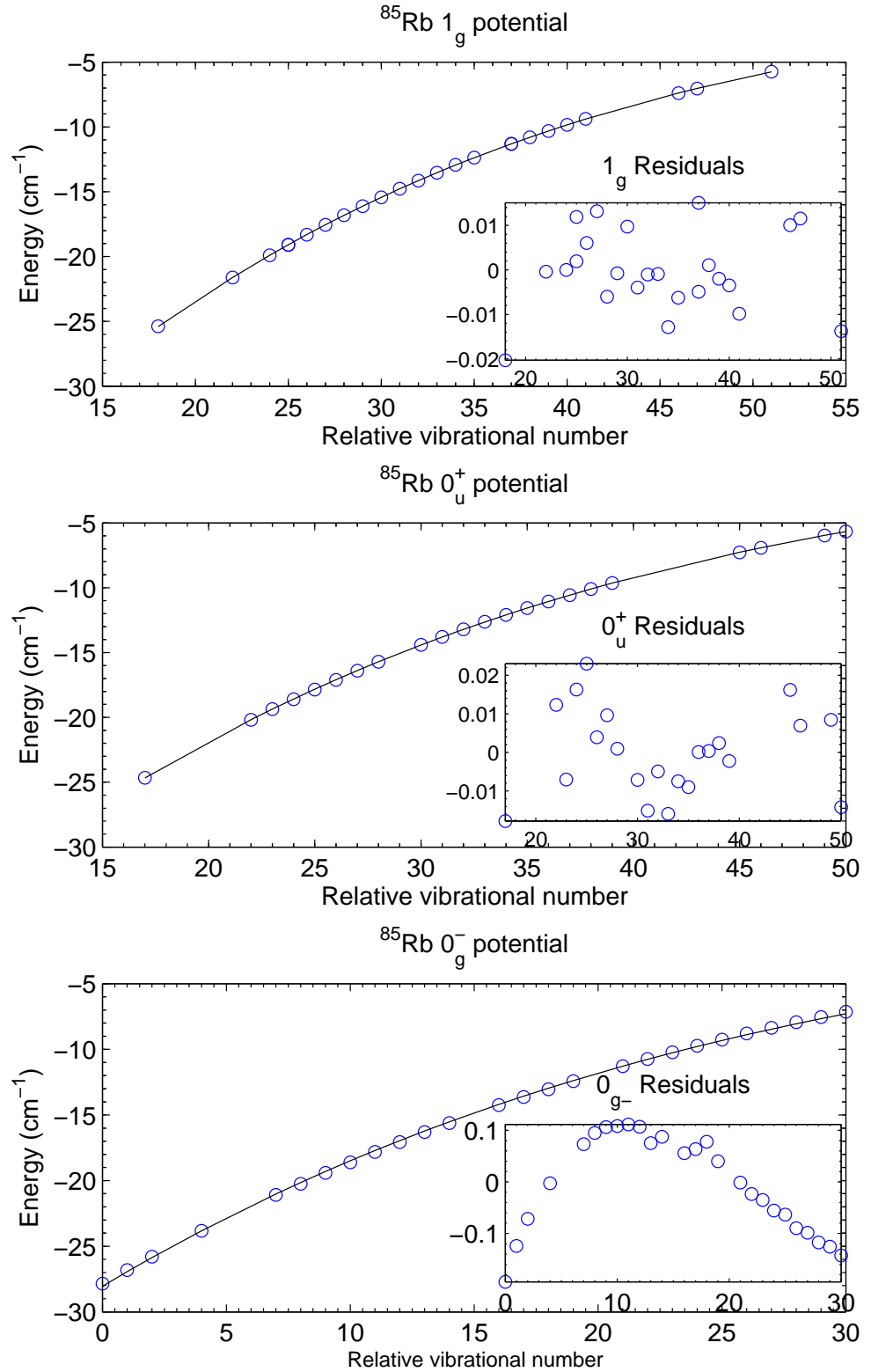
Fig. 6.12: Plot of vibrational number versus level energy for the ^{85}Rb$_2$ 0_g^-, 0_u^+ and 1_g potentials. Vibrational assignments are relative to the bottom of the well for the 0_g^- state. The fitted line is Equation 6.1. The residuals of the fit are shown in the inset.

Chapter 7

Conclusions

"A conclusion is the place where you got tired of thinking."

— Arthur Bloch

7.1 Thesis Conclusions

This thesis presented the construction and characterisation of a new experimental facility combining laser cooling, high resolution spectroscopy and ionisation detection for studies in atomic and molecular physics. All of the apparatus described were constructed solely by the author. In addition to the construction of the new facility the major results in this thesis are:

- Spectroscopy of ^{85}Rb atomic energy levels for nd states where n=6 - 42, over an energy range of 5000 cm^{-1} allowing assignment of these levels used for the following measurements.

- Measurement of the radiative decay rates for n=11-37 spanning an energy range over 1000 cm^{-1}.

- Modelling of population dynamics following excitation to an nd state where n=11 - 37, taking into account radiative decay and blackbody redistribution to neighbouring states connected by dipole allowed transitions. This model was able to isolate the dependance on a single free black-body interaction parameter.

- The comparison of experimental decay rates and the decay rate models over principal quantum n=11 - 37. This analysis provided an important test of a common coulombic approximation of the black-body interaction strength against the Theoudisou calculations which include spin orbit and core polarisability. Characterisation of the black body characterisation is also important since it is a source of decoherance for many quantum information schemes.

- Resonance-enhanced multi-photon ionisation spectroscopy with time-of-flight discrimination of the excited ^{87}Rb$_2$ molecular potentials over an energy range > 6000 cm^{-1} was performed. This measurement is an extension of previous work, extending measurements over a greater energy range, allowing investigation deeper into excited state molecular potentials identified in earlier work.

- Trap-loss photoassociation spectroscopy of ^{85}Rb and ^{87}Rb over 30 cm^{-1} detuning range below the 5s+5p$_{3/2}$ limit. This work also extends on previous work but provides an important isotopic comparison, showing isotopic differences beyond a simple mass scaling in the NDE approximation.

- Assignment of the 0_u^+, 1_g and 0_g^- series for ^{87}Rb and ^{85}Rb from trap-loss and ionisation measurements. These identifications allowed a basic analysis of the series in both isotopes within the LeRoy-Bernstein formalism. Deviations from the model are seen in the residuals to the fit for all of the series identified and both isotopes.

- A comparison of measured parameters of the 0_u^+ and 1_g series was possible by relating both to the fundamental resonant dipole C$_3$ coefficient in the Hund's Case A basis set. This also allowed comparison with theoretical predictions and previous experimental measurements.

A paper is currently being written on the Rydberg work presented in this thesis. The title is "Population Dynamics of Ultracold Rydberg Atoms", and it will be submitted to the journal *Spectrochimica Acta*.

7.2 Future Work

This thesis reports the construction of a versatile new apparatus for investigation of a wide range of atomic and molecular physics. As such the completion of this thesis is not so much an end point as a starting point for many further investigations.

Much still remains to be done on the work presented here, improving the reported experiments, further investigation into some results that are not currently well understood, and more detailed modelling to explain some of the data presented here. Some promising experiments not touched on in this thesis could not be performed in the current system, but may become viable after the addition of extra trapping, cooling or detection techniques. The flexibility of the apparatus should allow many new areas of investigation not yet considered by the author in this fast moving field.

Some possible areas of further investigation are discussed below.

7.2.1 Coupled Channel Modelling

The LeRoy-Bernstein analysis applied to the 0_u^+ and 1_g states describes the vibrational spacing of those series well; however examination of the residuals reveals there is additional systematic deviation from purely R^{-3} potential behaviour.

The description of the Coloumbic interaction can be straightforwardly improved with the inclusion of higher order dispersion coefficients in the upper and lower molecular potentials. In NDE analysis relativistic spin-orbit effects are introduced in the long range $R \to \infty$ limit, i.e. $V_{so} \propto \langle \vec{s}.\vec{l} \rangle$. A more robust theoretical model will take into

account the R dependence of the spin-orbit coupling interaction. To extend the analysis closer to resonance will also require the inclusion of the hyperfine interaction.

7.2.2   Spectroscopy of Higher Molecular States

Measurements have been performed on excited molecular states, using bound-bound REMPI spectroscopy of molecules formed by photo-association. A wide range of energies was surveyed in this spectrum; however higher resolution measurements are required to assign vibrational levels in overlapping electronic potentials. The improvement in resolution is best achieved by exciting to more deeply bound, widely spaced levels in the PA step. The step-size of the ionising laser can also be reduced by a factor of 10 to 0.001 nm/pulse. The resolution will ultimately be limited by the photo-ionisation laser line width of 6 GHz.

7.2.3   Field Ionisation

The measurements of decay from excited Rydberg levels could be more accurately determined with the implementation of field ionisation. Time-dependent field ionisation techniques can discriminate between states with different ionisation energy. The resolution is typically sufficient to discriminate between neighbouring Rydberg electronic levels, and even levels split by fine structure. Such a system would alow a more direct measurement of population transfer by blackbody interaction, and allow comparison of different quantum states with the same principal quantum number.

7.2.4   Blue-Satellites

The origin of the broad blue satellites identified in Section 4.4 remains poorly understood. They may arise from the presence of an electric field at the MOT centre or from the high peak powers present in the pulsed ionisation detection system. It

would be interesting to see the dependence of these features on electric field strength, or when probed with a CW laser with similar average power but lower peak power than the pulsed probe.

7.2.5 Improved PA Measurements

The resolution of the photo-association data could be improved by increasing the loading rate of the trap without increasing the effect of background collisions. Standard techniques to achieve higher loading rates include loading from an additional source of cold atoms such as a 2D-MOT, a low velocity intense source (LVIS) or a Zeeman slower.

7.2.6 Time Resolved Spectroscopy

The long timescale of ultracold collisions allows the time evolution of the reaction to be monitored. In room temperature reactions, changes in the internuclear separations of reactants take place on femtosecond timescales, which require sophisticated very short pulse lasers to resolve. Ultra-cold collisions take place on nanosecond timescales, which is a timescale accessible by pulses produced with acousto-optical switches.

7.2.7 Coherent Formation of Ground-State Molecules

Related to the discussion of measuring ultrashort time dynamics is coherent control of collisional processes. Short timescale pulses have broad Fourier limited spectral widths. Spectral shaping of coherent pulses has been investigated as a technique to coherently transfer free atoms into bound ground state molecules, avoiding spontaneous decay processes [89] [90]. A femto-second pulsed laser facility exists in an adjacent laboratory to the project described here and experiments may be extended to an ultracold sample.

7.2.8 Trapping of Molecules

In the work reported here molecules are formed in the MOT but are not trapped; so they diffuse out of the trap or fall out under gravity. Techniques for trapping of molecules include the addition of an optical dipole trap which must be far from all molecular resonances, and magnetic trapping of triplet state molecules.

7.2.9 Blue-Detuned Photoassociation

All of the spectra presented here were taken with the PA laser tuned below an atomic resonance. Repulsive potentials which are blue detuned from atomic resonances sometimes contain structure such as avoided crossings which can support bound states. Such structure has been proposed as a possible efficient route to ground vibrational state molecules since they can have good Franck-Condon overlap with the bottom of the ground state potential [91]. These states will efficiently populate the ground state once excited; however the PA step requires high densities to efficiently populate. It is noted here that a blue-detuned PA probe will impose a repulsive dipole force on atoms, driving atoms from the most intense part of the laser in contrast to the usual red-detuned PA. Blue detuned "doughnut" mode traps have been demonstrated, trapping atoms in the low intensity central minima at high densities.

7.2.10 Hetero-nuclear Molecules

The creation of hetero-nuclear molecules is now being pursued by a number of groups. A typical starting point is dual overlapping MOTs of different atomic species. A photoassociation probe is then introduced into the sample and both homo-nuclear and hetero-nuclear molecules can be formed according to the frequency of the PA probe. It is noted here that hetero-nuclear molecules do not exhibit an R^{-3} resonant dipole-dipole interaction. The leading term in the upper potential is the shorter range

R^{-6}, resulting in lower Franck-Condon overlap with scattering wavefunctions and lower transition rates.

Bibliography

[1] Allday, Jonathan. *Quarks, Leptons and the Big Bang, Second Edition.* IOP publishing, London, 2002.

[2] Downloaded from: http://www.linearcollider.org/. *ILC Design Summary Document.* Form One, Hamburg, 2006.

[3] P. Lebedev. The Experimental Study of the Pressure of the Light. *Annalen der Physik*, **Leipzig 6**:433, 1901.

[4] R. Frisch. Experimenteller Nachweis des Einsteinschen strahlungsruckstosses. *Z. Phys.*, **86**:42, 1933.

[5] T.W. Hänsch and A.L. Schawlow. Cooling of gases by laser radiation. *Opt. Commun.*, **13**:68, 1975.

[6] D. Wineland and H. Dehmelt. Proposed 10^{14} $\delta\nu/\nu$ laser fluorescence spectroscopy on Tl^+ MONO-Ion oscillator. *Bull. Am. Phys, Soc.*, **20**:637, 1975.

[7] S. Chu, L. Hollberg, J.E. Bjorkholm, A. Cable and A. Ashkin. Three dimensional viscous confinement and cooling of atoms by resonance radiation pressure. *Phys. Rev. Lett.*, **55**:48, 1985.

[8] Paul D. Lett, Richard N. Watts, Christoph I. Westbrook, William D. Phillips, Phillip L. Gould and Harold J. Metcalf. Observation of Atoms Laser Cooled below the Doppler Limit. *Phys. Rev. Lett.*, **61**:169–172, 1988.

[9] J. Dalibard and C. Cohen-Tannoudji. Laser cooling below the Doppler limit by polarization gradients: simple theoretical models. *J. Opt. Soc. Am. B.*, **6**:2023, 1989.

[10] E.L. Raab, M. Prentiss, A. Cable, S. Chu and D.E. Pritchard. Trapping of neutral sodium atoms with radiation pressure. *Phys. Rev. Lett.*, **59**:2631, 1987.

[11] C. Monroe, W. Swann, H. Robinson and C. Wieman. Very cold trapped atoms in a vapor cell. *Phys. Rev. Lett.*, **65**:1571, 1990.

[12] John Weiner. *Cold and Ultracold Collisions in Quantum Microscopic and Mesoscopic Systems.* Cambridge University Press, Cambridge, 2003.

[13] H. Scheingraber and C. R. Vidal. Discrete and continuous Franck Condon factors of the Mg_2 $A^1\Sigma_u^+ - X^1\Sigma_g^+$ system and their J dependence. *J. Chem. Phys.*, **66**:3694, 1977.

[14] H.R. Thorsheim, J. Weiner and P. Julienne. Laser induced photoassociation of ultracold sodium atoms. *Phys. Rev. Lett.*, **58**:2420–2423, 1987.

[15] J.J. Hudson, B.E. Sauer, M.R. Tarbutt, and E.A. Hinds. Measurement of the Electron Electric Dipole Moment Using YbF Molecules. *Phys. Rev. Lett.*, **89**:023003, 2002.

[16] T. Opatrny and G. Kurizki. Matter-Wave Entanglement and Teleportation by Molecular Dissociation and Collisions. *Phys. Rev. Lett.*, **86**:3180–3183, 2001.

[17] D.J. Heinzen, R. Wynar, P.D. Drummond, and K.V. Kheruntsyan. Superchemistry: Dynamics of Coupled Atomic and Molecular Bose-Einstein Condensates. *Phys. Rev. Lett.*, **84**:5029–5033, 2000.

[18] Ch. Lisdat, M. Franck, H. Knöckel, M.-L. Almazor, and E. Tiemann. Realization of a Ramsey-Borde matter wave interferometer on the K_2 molecule. *Eur. Phys. J. D*, **12**:235–240, 2000.

[19] Peter van der Straten and Harold J. Metcalf. *Laser Cooling and Trapping.* Springer-Verlag, New York, 1999.

[20] William D. Phillips. Laser cooling and trapping of neutral atoms. *Rev. Mod. Phys.*, **70**:721, 1998.

[21] A.M. Steane, M. Chowdhury and C.J. Foot. Radiation force in the magneto-optical trap. *J. Opt. Soc. Am. B.*, **9,12**:2142, 1992.

Bibliography

[22] W. Demtröder. *Laser Spectroscopy: Basic Concepts and Instrumentation.* Springer-Verlag, Berlin, 1996.

[23] Daniel A. Steck. *Rubidium 87 D Line Data.* latest version available at: http://steck.us/alkalidata, 2003.

[24] S.G. Cox, P.F. Griffin, C.S. Adams, D. DeMille and E. Riis. Reusable ultrahigh vacuum viewport bakeable to 240 °C. *Rev. Sci. Instr.*, **74,6**:3185–3187, 2003.

[25] M. Prentiss, A. Cable, J. E. Bjorkholm, Steven Chu, E. L. Raab and D. E. Pritchard. Atomic-density-dependent losses in an optical trap. *Opt. Lett.*, **13,6**:452, 1988.

[26] J. Arlt, P. Bance, S. Hopkins, J. Martin, S. Webster, A. Wilson, K. Zetie and C.J. Foot. Suppression of collisional loss from a magnetic trap. *J. Phys. B.*, **31**:L321–L327, 1998.

[27] D.S. Weiss, E. Riis, Y. Shevy, P.J. Ungar and S. Chu. Optical molasses and multilevel atoms: experiment. *J. Opt. Soc. Am. B.*, **6**:2072–2083, 1989.

[28] M. Kemmann, I. Mistrik, S. Nussmann, H. Helm, C. J. Williams and P. S. Julienne. Near-threshold photoassociation of ^{87}Rb$_2$. *Phys. Rev. A*, **69**:022715, 2004.

[29] *Matlab 7.* The MathWorks, Inc., 2004.

[30] C. Gabbanini, A. Fioretti, A. Lucchesini, S. Gozzini, and M. Mazzoni. Cold Rubidium Molecules Formed in a Magneto-Optical Trap. *Phys. Rev. Lett.*, **84,13**:2814–2817, 2000.

[31] W.E. Cook and T.F. Gallagher. Effects of blackbody radiation on highly excited atoms. *Phys. Rev. A*, **21**:588, 1980.

[32] K.M.F. Magalhaes, A.L. de Oliveira, R.A.D.S. Zanon, V.S. Bagnato and L.G. Marcassa. Lifetime determination of high excited states of ^{85}Rb using a sample of cold atoms. *Opt. Commun.*, **184**:385–389, 2000.

Bibliography

[33] A. L. Oliviera, M. W. Mancini, V. S. Bagnato and L. G. Marcassa. Measurements of Rydberg lifetimes using cold trapped atoms. *Phys. Rev. A*, **65**:031401, 2002.

[34] I.I. Ryabtsev, D.B. Tretyakov and I.I. Beterov. Applicability of Rydberg atoms to quantum computers. *J. Phys. B.*, **38**:S421–S436, 2005.

[35] S.A. Lee, J. Helmcke, J.L. Hall and B.P. Stoicheff. Doppler-free two-photon transitions to Rydberg levels: convenient, useful, and precise reference wavelengths for dye lasers. *Opt. Lett.*, **3**:141–143, 1978.

[36] C. J. Lorenzen and K. Niemax. Quantum Defects of the $n^2P_{1/2,3/2}$ levels in ^{39}K I and ^{85}Rb I. *Physica. Scripta*, **27**:300–305, 1983.

[37] M. Weidemuller, C. Gabbanini, J. Hare, M. Gross and S. Haroche. A beam of laser cooled lithium Rydberg atoms for precision microwave spectroscopy. *Opt. Commun.*, **101**:342–346, 1993.

[38] I. Mourachko, D. Comparat, F. deTomasi, A. Fioretti, P. Nosbaum, V.M. Akulkin and P. Pillet. Many body effects in a frozen Rydberg gas. *Phys. Rev. Lett.*, **80**:253–256, 1998.

[39] M.P. Robinson, B.L. Tolra, M.W. Noel, T.F. Gallagher and P. Pillet. Spontaneous evolution of Rydberg atoms into an ultracold plasma. *Phys. Rev. Lett.*, **85**:4466–4469, 2000.

[40] Wenhui Li, I. Mourachko, M.W. Noel and T.F. Gallagher. Millimeter-wave spectroscopy of cold Rb atoms in a magneto optical trap: Quantum defects of the ns, np and nd series. *Phys. Rev. A*, **67**:052502–1, 2003.

[41] M. Hugon, F. Gounand and P.R. Fournier. Radiative lifetimes of highly excited f states in Rb. *J. Phys. B.*, **11**:L605, 1978.

[42] M. Hugon, F. Gounand and P.R. Fournier. Superradiant cascading effects in Rubidium Rydberg levels. *J. Phys. B.*, **12,4**:547, 1979.

[43] F. Gounand, M. Hugon and P.R. Fournier. Radiative lifetimes of highly excited states in rubidium. *J. Phys. (Paris)*, **41**:119, 1980.

[44] C. Gabbanini. Assessments of lifetimes and photoionization cross-sections at 10.6 μm of nd Rydberg states of Rb measured in a magneto-optical trap. *Spectrochimica Acta B.*, **61**:196–199, 2006.

[45] U. Fano. Quantum Defect Theory of l Uncoupling in H_2 as an Example of Channel-Interaction Treatment. *Phys. Rev. A*, **2**:353, 1970.

[46] M. J. Seaton. Quantum defect theory. *Rep. Prog. Phys.*, **46**:167, 1983.

[47] F. Gounand. Calculation of radial matrix elements and radiative lifetimes for highly excited states of alkali atoms using the Coulombic approximation. *J. Phys. (Paris)*, **40**:457–460, 1979.

[48] J.W. Farley and W.H. Wing. Accurate calculations of dynamic Stark shifts and depopulation rates of Rydberg energy levels induced by blackbody radiation. Hydrogen, helium and alkali-metal atoms. *Phys. Rev. A*, **23,5**:2397, 1981.

[49] Constantine E. Theodosiou. Lifetime of alkali-metal-atoms Rydberg states. *Phys. Rev. A*, **30,6**:2881, 1984.

[50] J.H. Hoogenraad and L.D. Noordam. Rydberg atoms in far-infrared radiation fields. I. Dipole matrix elements of H, Li, and Rb. *Phys. Rev. A*, **57,6**:4533–4545, 1998.

[51] M.S. O'Sullivan and B.P. Stoicheff. Scalar and tensor polarisabilities of ^{2}D Rydberg states in Rb. *Phys. Rev. A*, **33,3**:1640–1645, 1986.

[52] B. Ji, C.C. Tsai and W.C. Stwalley. Proposed modification of the criterion for the region of validity of the inverse-power expansion in diatomic long-range potentials. *Chem. Phys. Lett.*, **236**:242–246, 1995.

[53] M. Marinescu, J. F. Babb and A. Dalagarno. Long-range potentials, including retardation, for the interaction of two alkali-metal atoms. *Phys. Rev. A*, **50,4**:3096–3104, 1994.

[54] Jenning Y. Seto, Robert J. Le Roy, Jean Verges and Claude Amiot. Direct potential fit analysis of the $X^1\Sigma_g^+$ state of Rb_2: Nothing else will do! *J. Chem. Phys.*, **113**:8, 2000.

[55] M. Foucrault, Ph. Millie and J. P. Daudley. Nonperturbative methods for core-valence correlation in pseudopotential calculatoins: Applications to the Rb_2 and Cs_2 molecules. *J. Chem. Phys.*, **96**:2, 2000.

[56] J.L. Roberts, N.R. Claussen, J.P. Burke, C.H. Greene, E.A. Cornell and C.E. Wieman. Resonant Magnetic Field Control of Elastic Scattering in Cold ^{85}Rb. *Phys. Rev. Lett.*, **81**:5109, 1998.

[57] M. Marinescu and A. Dalgarno. Long range potentials,including retardation, for the interaction of two alkali metal atoms. *Phys. Rev. A*, **52**:311, 1995.

[58] F. Speigelmann, D. Pavolini and J-P Daudey. Theoretical study of the excited states of the heavier alkali dimers. II. The Rb_2 molecule. *J. Phys. B.*, **22**:2465–2484, 1989.

[59] Kevin M. Jones, Eite Tiesinger, Paul D. Lett and Paul S. Julienne. Ultracold photoassociation spectroscopy: Long-range molecules and atomic scattering. *Rev. Mod. Phys.*, **78**:483–535, 2006.

[60] H. Lefebvre-Brion and R. W. Field. *The spectra and dynamics of diatomic molecules.* Elsevier Academic Press, London, 2004.

[61] Mladen Movre and Goran Pichler. Resonance interaction and self broadening of alkali resonance lines I. Adiabatic potential curves. *J. Phys. B.*, **10,13**:2631–2638, 1977.

Bibliography

[62] Robert J. LeRoy and Richard Bernstein. Dissociation energy and long range potential of diatomic molecules from vibrational spacings of higher levels. *J. Chem. Phys.*, **52,8**:3870–3879, 1970.

[63] Daniel Comparat. Improved LeRoy-Bernstein near-dissociation expansion formula. Tutorial application to photoassociation spectroscopy of long-range states. *arXiv*, **quant-ph**:0305157, 2003.

[64] R.J. Le Roy. *LEVEL 7.5: A Computer Program for Solving the Radial Schrodinger Equation for Bound and Quasibound Levels.* University of Waterloo Chemical Physics Research Report CP-655 (2002), The source code and manual for this program may be obtained from the "Computer Programs" link on the www site http://leroy.waterloo.ca., 1994.

[65] J.L. Bohn and P.S. Julienne . Semianalytic treatment of two-color photoassociation spectroscopy and control of cold atoms. *Phys. Rev. A*, **54**:R4637–R4640, 1996.

[66] P.S. Julienne and F.H. Mies. Collisions of ultracold trapped atoms. *J. Opt. Soc. Am. B.*, **6**:2257–2269, 1989.

[67] F.H. Mies and M. Raoult. Analysis of threshold effects in ultracold atomic collisions. *Phys. Rev. A*, **62**:012708, 2000.

[68] R.J. Napolitano, J. Weiner, C.J. Williams and P.S. Julienne. Line shape of high resolution photoassociation spectra of optically cooled atoms. *Phys. Rev. Lett.*, **73**:1352–1355, 1994.

[69] J.L.Bohn and P.S. Julienne. Semianalytic theory of laser assisted resonant cold collisions. *Phys. Rev. A*, **60**:414–425, 1999.

[70] Boisseau, C., E. Audouard, J. Vigue, and P. S. Julienne. Reflection approximation in photoassociation spectroscopy. *Phys. Rev. A*, **62**:052705, 2000.

[71] P. D. Lett, P. S. Julienne and W.D. Phillips. Photoassociation spectroscopy of laser cooled atoms. *Annu. Rev. Phys. Chem.*, **46**:423–452, 1995.

[72] William C. Stwalley and He Wang. Photoassociation of ultracold atoms: A new spectroscopic technique. *J. Mol. Spec.*, **195**:194–228, 1999.

[73] F. Masnou-Seeuws and P. Pillet. Formation of ultracold molecules(T≤200 μK) via photoassociation in a gas of laser cooled atoms. *Adv. At., Mol., Opt. Phys.*, **47**:53–127, 2001.

[74] R.A. Cline, J.D Miller and D.J. Heinzen. Study of Rb_2 long range states by high resolution photoassociation spectroscopy. *Phys. Rev. Lett.*, **73**:632–635, 1994.

[75] H. M. J. M. Boesten, C. C. Tsai, B. J. Verhaar and D. J. Heinzen. Observation of a Shape Resonance in Cold-Atom Scattering by Pulsed Photoassociation. *Phys. Rev. Lett.*, **77,26**:5194–5197, 1996.

[76] A. Fioretti, C. Amiot, C.M. Dion, O. Dulieu, M. Mazzoni, G. Smirne, and C. Gabbanini. Cold rubidium molecule formation through photoassociation: A spectroscopic study of the 0_g^- long-range state of $^{87}Rb_2$. **15**:189–198, 2001.

[77] H. Jelassi, B. Viaris de Lesegno and L. Provost. Photoassociation spectroscopy of $^{87}Rb_2$ ($5s_{1/2}$+ $5p_{3/2}$) 0_g^- long range molecular states; analysis by Lu-Fano graph and improved LeRoy-Bernstein formula. *Phys. Rev. A*, **73**:032501, 2006.

[78] T. Bergeman, J. Qi, D. Wang, Y. Huang, H.K. Pechkis, E.E. Eyler, P.L. Gould, W.C. Stwalley, R.A. Cline, J.D. Miller and D.J. Heinzen. Photoassociation of ^{85}Rb atoms into 0_u^+ states near the 5S+5P atomic limits.

[79] Y. Huang, J. Qi, H.K. Pechkis, D. Wang, E.E. Eyler, P.L. Gould and W.C. Stwalley. Formation, detection and spectroscopy of ultracold Rb_2 in the ground $X^1\Sigma_g^+$ state. *J. Phys. B.*, **39**:S857–S869, 2006.

[80] J. Lozeille, A. Fioretti, C. Gabbanini,Y. Huang, H.K. Pechkis, D. Wang, P.L. Gould, E.E. Eyler, W.C. Stwalley, M. Aymar and O. Dulieu. Detection by two-photon ionization and magnetic trapping of cold Rb_2 triplet state molecules. *Eur. Phys. J. D*, **39**:261–269, 2006.

Bibliography

[81] Burleigh Instruments. Burleigh WA-1000 and WA-1500 Wavemeter Operating Manual.

[82] Cyril Drag, Bruno Laburthe Tolra, Olivier Dulieu, Daniel Comparat, Mihaela Vatasescu, Salah Boussen, Samuel Guibel, Anne Crubellier and Pierre Pillet. Experimental versus theoretical rates for photoassociation and for formation of ultracold molecules. *J. Quant. Elec.*, **36,12**:1378–1387, 2000.

[83] J. E. Sansonetti. Wavelengths, Transition Probabilities and Energy Levels for the Spectra of Rubidium RbI through Rb XXXVII. *J. Phys. Chem. Ref. Data*, **35,1**:301–421, 2006.

[84] C. Amiot. Analysis of spectra obtained by cold-atom spectroscopy: the Rb, l_g and 0_g^- electronic states up to 100 Å. *Chem. Phys. Lett.*, 241:133–139, 1995.

[85] A. Fioretti, C. Amiot, C.M. Dion, O. Dulieu, M. Mazzoni, G. Smirne, and C. Gabbanini. Cold rubidium molecule formation through photoassociation: A spectroscopic study of the 0_g^- long-range state of $^{87}Rb_2$. **15**:194, 2001.

[86] V. Kokoouline, O. Dulieu, and F. Masnou-Seeuws. Theoretical treatment of channel mixing in excited Rb_2 and Cs_2 ultracold molecules: Perturbations in 0_u^+ photoassociation and fluorescence spectra. *Phys. Rev. A*, 62:022504, 2000.

[87] M. Marinescu and A. Dalgarno. Dispersion forces and long-range electronic transition dipole moments of alkali-metal dimer excited states. *Phys. Rev. A*, **52**:311–328, 1995.

[88] Prof. Dr. Eberhard Tiemann. Private communication.

[89] Brown, B.L. Dicks and A.J. Walmsley. The coherent effect of chirped femtosecond laser pulses on the formation of ultracold molecules in a magneto-optical trap. *Opt. Commun.*, 264:278–284, 2006.

[90] Brown, B.L. Dicks and A.J. Walmsley. Coherent Control of Ultracold Molecule Dynamics in a Magneto-Optical Trap by Use of Chirped Femtosecond Laser Pulses. *Phys. Rev. Lett.*, 96:173002, 2006.

[91] M.-L. Almazor, O. Dulieu, F. Masnou-Seeuws, R. Beuc and G. Pichler. Formation of ultracold molecules via photoassociation with blue detuned laser light. *Eur. Phys. J. D*, 15,3:355–363, 2001.

Appendix A

Solving the rate equation for Rydberg lifetime measurements

A.1   Coupled Rate Equation Problem

$$
\begin{bmatrix} \frac{dN_d(t)}{dt} \\ \frac{dN_p(t)}{dt} \\ \frac{dN_f(t)}{dt} \end{bmatrix} = \begin{bmatrix} -\Gamma_d - \Gamma_{dp} - \Gamma_{df} & \Gamma_{pd} & \Gamma_{fd} \\ +\Gamma_{dp} & -\Gamma_p - \Gamma_{pd} & 0 \\ \Gamma_{df} & 0 & -\Gamma_f - \Gamma_{fd} \end{bmatrix} \begin{bmatrix} N_d(t) \\ N_p(t) \\ N_f(t) \end{bmatrix} \tag{A.1}
$$

with boundary conditions:

$$
\begin{bmatrix} N_d(0) \\ N_p(0) \\ N_f(0) \end{bmatrix} = \begin{bmatrix} N_0 \\ 0 \\ 0 \end{bmatrix} \tag{A.2}
$$

A.2   Solving Coupled Rate Equations for n=11-37

```
%%%%%%%%%%%%%%%%%%%%%%%%%%%%%%%%%%%%%%%%%%%%%%%%%%%%%%%%%%%%%%%%%%%%%%%%
% Matlab code to Calculate N(t) after excitation to an nd state%
```

Bibliography

```
%%%%%%%%%%%%%%%%%%%%%%%%%%%%%%%%%%%%%%%%%%%%%%%%%%%%%%%%%%%%%%

clc;close all;clear all;

%%%%%%%%%%%%%%%%%%%
% define variables %
%%%%%%%%%%%%%%%%%%%%

%x=nd, population of nd state
%y=np, population of (n+1)p state
%z=nf, population of (n-1)f state
%gp -spontaneous decay rate of np state,
%gd -spontaneous decay rate of nd state,
%gf-spontaneous decay rate of nf state,
%gdp-black body decay rates coupling between d and p levels,
%gpd-black body decay rates coupling between p and d levels,
%gdf-black body decay rates coupling between d and f levels,
%gfd-black body decay rates coupling between f and d levels,
%No -initial atom number

%%%%%%%%%%%%%%%%%%%%%%%%%%%%%
%calculate rate constants %
%%%%%%%%%%%%%%%%%%%%%%%%%%%%

    i=0;
    for n=11:37;i=i+1;

    gd_ns=(2.10.*(n-1.347157).^(2.89)).^(-1);
    gd=1e3.*gd_ns;% put into = \mu s
    gp_ns=(2.80.*(n-2.65456+1).^(3.01)).^(-1);
    gp=1e3.*gp_ns;% put into = \mu s
    gf_ns=(0.76.*(n-0.016312-1).^(2.95)).^(-1);
    gf=1e3.*gf_ns;% put into = \mu s

    %C for <(n+1)p1/2|r|nd>=-0.32
    Cdp=0.4108*(((-n)^(-2))^(3/4)*((-(n+1))^(-2))^(3/4)*(abs(0.5*(n)^(-2)-0.5*(n+1)^(-2)))^(-5/3));
    ddp=-1.0*Cdp; %relative |<(n+1)p|r|nd>|
    transdp= 2*abs(((n-2.65456+1)^-2-(n-1.347157)^-2)^3*(abs(ddp))^2);% factor of 2 is p1/2 + p3/2
    %C for <(n+1)p1/2|r|nd>=-0.32
    Cdf = 0.4108*(((-n)^(-2))^(3/4)*((-(n-1))^(-2))^(3/4)*(abs(0.5*(n)^(-2)-0.5*(n-1)^(-2)))^(-5/3));
    ddf=-0.38*Cdf; %relative |<(n-1)f|r|nd>|
    transdf= abs(((n-0.016312-1)^-2-(n-1.347157)^-2)^3*(abs(ddf))^2);

    fracdp=transdp/(transdp+transdf);
    fracdf=transdf/(transdp+transdf);
```

145

```
%uncomment desired blackbody rate, Theoudisou or Farley


%bb_rate= 1e3/(294.242+ 0.096*(n-1.347157)^3.867);%bbrate theoudisou
bb_rate=(1e-6.*2.03E7.*(n-1.347157).^(-2));%bbrate farley
gdp=bb_rate*(0.645)^2*fracdp;%13/14;%*(23/24);%standard formula
gdf=bb_rate*(0.355)^2*fracdf;%1/14;%*(1/24);% standard formula
gfd=gdf;
gpd=gdp;


gamma=[gd gp gf gdp gfd gdf gfd];%print the rates's and lifetimes if wanted
tau=gamma.^(-1);


No=1;%initial fractional population = 1


%%%%%%%%%%%%%%%%%%%%%%%%%%%%%%%%%%%%%%%%%%%
%Solve eigenvalue problem for populations %
%%%%%%%%%%%%%%%%%%%%%%%%%%%%%%%%%%%%%%%%%%%


f=sym('f'); %treat time variable f as symbolic
A=[-gd-gdp-gdf,gpd,gfd;gdp,-gp-gdp,0;gdf,0,-gf-gfd];
[v evalue] =eig(A);% evaluate eigenvalus and eigenvectors
eval=diag(evalue);
initial=[1,0,0]; % boundary conditions N(t=0)=Nd
c=initial/v';

    for ii=1:length(v);
    B(:,ii)=c(ii)*v(:,ii)*exp(eval(ii)*f);
    end
B;


nd=sum(B(1,:));
nd=vpa(nd,3);
np=sum(B(2,:));
np=vpa(np,3);
nf=sum(B(3,:));
nf=vpa(nf,3);
N=np+nd+nf;
N=vpa(N,3);
%    t=(0:0.001:500);% higher time resolution slower calculation
    t=(0:0.01:500);% lower time resolution faster calculation
    N=subs(N,f,t); % evaluate N(t) and discrete times t.
    all_decay_rates(i,:)= N;
    n(i)=10+i; % quantum number n, for n=11 to 37
    end
```

146

```
save('N_and_t_for_n.mat','all_decay_rates','t','n','gdp','bb_rate')
clear all; load('N_and_t_for_n.mat')


    %%%%%%%%%%
    %plot Ns  %
    %%%%%%%%%%

plot(t,all_decay_rates)
xlabel('Time (\mu s)','FontSize',12);
ylabel('Atomic Population Fraction N','FontSize',12); box on;
set(gca,'XMinorTick','On','YMinorTick','On','FontSize',12);
set(gcf, 'PaperPosition', [7 1 19 9],'PaperSize',[20.98 29.68]);% paper position: [left bottom width height]
```